DISSERTATION

submitted to
the Combined Faculties
for the Natural Sciences and for Mathematics
of the Ruperto-Carola University
of Heidelberg, Germany

for the degree of
Doctor of Natural Sciences

presented by

Dipl.-Phys. David Emschermann

born in Bocholt, Germany

Oral examination: 20 January 2010

Construction and Performance
of the
ALICE Transition Radiation Detector

Referees :

Prof. Dr. Johannes P. Wessels

Prof. Dr. Ulrich Uwer

Was alles möglich ist,
merkt man erst,
wenn man es einfach macht.

Kurzfassung

Aufbau und Leistungsmerkmale des ALICE Übergangsstrahlungsdetektors

Der Übergangsstrahlungsdetektor (TRD) wurde konstruiert, um bei Schwerionenkollisionen Elektronen in dem von Pionen dominierten Untergrund zu identifizieren. Da Elektronen nicht stark wechselwirken, ermöglichen sie einen Einblick in den Anfangszustand der Teilchenkollision. Als Trigger auf e^+e^- Paare mit hohem Transversalimpuls kann der TRD 6,5 μs nach der Kollision die Auslese der Zeitprojektionskammer (TPC) auslösen. Der TRD besteht aus 18 Supermodulen, die zylinderförmig im Zentralbereich des ALICE Detektors angeordnet sind, und bietet nahezu 1,2 Millionen Auslesekanäle auf einer Gesamtfläche von knapp 700 m^2. Es werden die Designparameter der Auslesepadebene vorgestellt und deren physikalische Eigenschaften analysiert. Das im Detektor beobachtete Rauschen kann direkt mit der statischen Kapazitätsverteilung der Pads in Verbindung gesetzt und korrigiert werden. Es folgt ein Überblick über die TRD Infrastruktur am CERN: ein 70kW Niedrigspannungssystem, ein 2,5kV Hochspannungssystem mit 1080 Kanälen und ein 600 Knoten umfassendes Ethernet Netzwerk. Serienproduzierte TRD Module wurden jeweils 2004 und 2007 am CERN PS Beschleuniger im Teilchenstrahl getestet. Details der Testaufbauten werden präsentiert, ebenso wie die dafür massgeschneiderten Datennahmesysteme. Zum Schluss wird die Effizienz des TRD analysiert, mit besonderem Augenmerk auf die Fähigkeit, Pionen korrekt von Elektronen zu unterscheiden, und auf die hervorragende Ortsauflösung.

Abstract

Construction and Performance of the ALICE Transition Radiation Detector

The Transition Radiation Detector (TRD) has been designed to identify electrons in the pion dominated background of heavy-ions collisions. As electrons do not interact strongly, they allow to probe the early phase of the interaction. As trigger on high-p_t e^+e^- pairs within 6.5 μs after collision, the TRD can initiate the readout of the Time Projection Chamber (TPC). The TRD is composed of 18 super modules arranged in a barrel geometry in the central part of the ALICE detector. It offers almost 1.2 million readout channels on a total area of close to 700 m^2. The particle detection properties of the TRD depend crucially on details in the design of the cathode pad readout plane. The design parameters of the TRD readout pad plane are introduced and analysed regarding their physical properties. The noise patterns observed in the detector can be directly linked to the static pad capacitance distribution and corrected for it. A summary is then given of the TRD services infrastructure at CERN: a 70kW low voltage system, a 1080 channel 2.5 kV high voltage setup and the Ethernet network serving more than 600 nodes. Two beam tests were conducted at the CERN PS accelerator in 2004 and 2007 using full sized TRD chambers from series production. Details on the setups are presented with particular emphasis on the custom tailored data acquisition systems. Finally the performance of the TRD is studied, focusing on the pion rejection capability and the excellent position resolution.

Contents

Chapter 1

Introduction

1.1 Motivation

- Where do we come from?
- What are we made of?
- What are the elementary components of matter?

Curiosity has driven mankind to numerous fascinating discoveries. Driven by experimental discoveries and theoretical advances, a revolution of the understanding of nuclear matter occurred within the last century. The best description of the world of particle physics today is the Standard Model, it gives a precise understanding of matter under normal conditions. Still many things remain uncertain. How would matter behave under extreme conditions, such as high temperature, high energy density or large pressure – under conditions similar to those in the early state of our universe, just a few microseconds after the Big Bang?

The exploration of the phase diagram of strongly interacting matter (Figure 1.1) is one of the most challenging fields of modern high-energy physics. The transition from hadronic to partonic degrees of freedom, which is expected to occur at high temperatures and/or high baryon densities, is of particular interest. The discovery of this phase transition would shed light on two fundamental, but still not well understood aspects of Quantum Chromo Dynamics (QCD): confinement and chiral symmetry breaking.

In the 1960s, Hagedorn postulated a melting point for hadronic matter at the Hagedorn temperature, where hadrons dissolve into a partonic liquid, see [6]. It is understood as the phase boundary temperature between the hadron gas phase and the deconfined state of mobile quarks and gluons. Today, numerical simulations in lattice QCD (Figure 1.2) indicate a dramatic increase of the scaled energy density when hadronic matter reaches temperatures around a critical value of $\mathrm{T}_c \approx 170$ MeV. For temperatures beyond T_c the scaled energy density saturates in a plateau. Here, the Quark-Gluon Plasma is reached, a phase of deconfined matter, in which quarks and gluons can propagate over large distances without being bound inside color neutral objects. Chiral symmetry is expected to be restored in the QGP phase: the constituent quark masses of the light u, d and s quarks vanish above T_c and only the much smaller masses generated by the electroweak Higgs field remain, Figure 1.3.

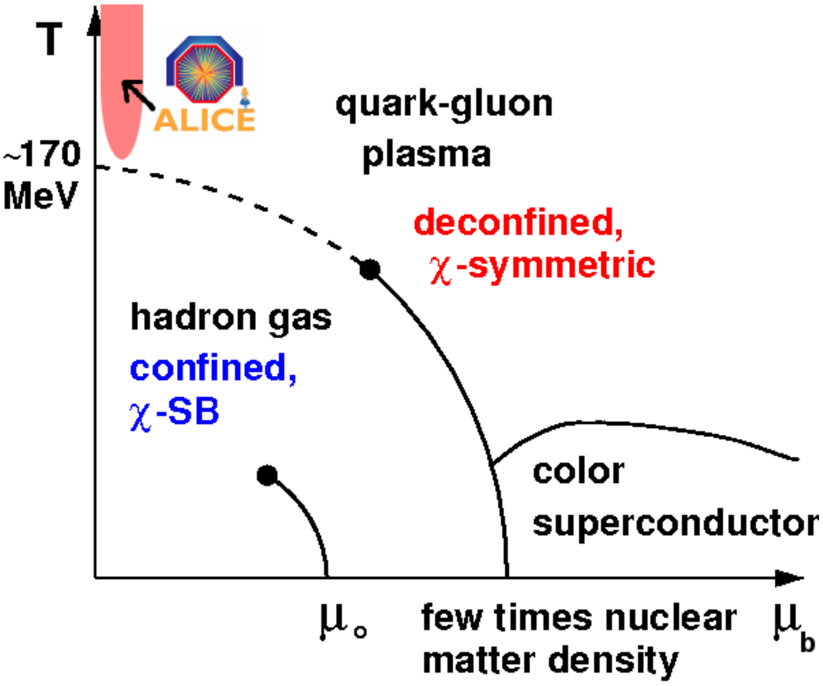

Figure 1.1: Sketch of the phase diagram of strongly interacting matter with hadronic and quark-gluon matter as a function of temperature T and baryon chemical potential μ_b, from [1]. Experimentally the QGP phase can be reached at extreme temperatures or extreme particle density.

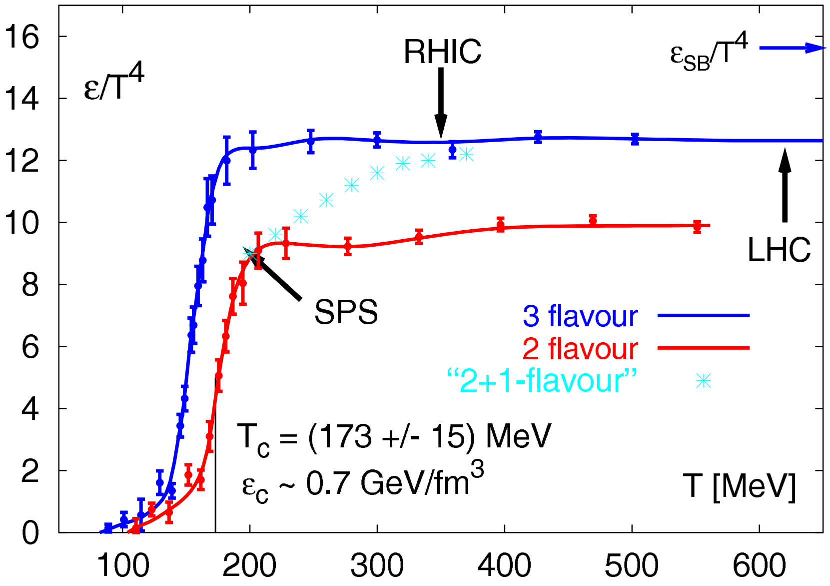

Figure 1.2: Scaled energy density ϵ/T^4 for thermal lattice-QCD with 2 and 3 light quark flavors (red, blue) and two light and one heavier flavor (light blue), from [2]. The arrow on the right side shows the value of the Stefan-Boltzmann limit for an ideal quark-gluon gas.

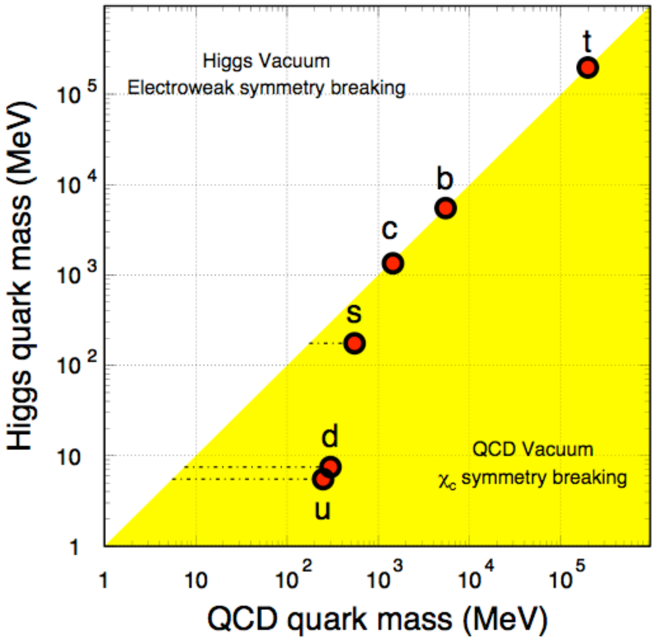

Figure 1.3: Quark masses in the Higgs and the QCD vacuum, from [5]. A large fraction of the light quark (u,d,s) masses is due to the chiral symmetry breaking in the QCD vacuum.

In the laboratory a quark-gluon plasma can be created by colliding heavy nuclei such as gold or lead head-on at very high energies. In the past decades such collisions have been performed at various accelerators, each new machine pushing for higher collision energy, such as the Alternating Gradient Synchrotron (AGS) at the Brookhaven National Laboratory (BNL), the Super Proton Synchrotron (SPS) at the European Organization for Nuclear Research (CERN), the Relativistic Heavy Ion Collider (RHIC) at BNL, to date the heavy ion collider with the highest center of mass energy. With the latest accelerator, the Large Hadron Collider (LHC) at CERN, the center-of-mass energy will increase by a factor of about 30 compared to RHIC. This leads to an increased initial energy density and longer lifetime of the QGP. According to [18], the fireball created in heavy-ion collisions at A Large Ion Collider Experiment (ALICE) is expected to be characterised by a rather long lifetime (4–10 fm/c) and an extended volume (2×10^4 fm^3). The temperature T will slightly increase as compared to RHIC, the baryo-chemical potential μ_b will approach 0 MeV, as indicated by the light red area in Figure 1.1.

Recent lattice QCD calculations at finite baryon chemical potential [8] predict a critical endpoint of the deconfinement phase transition at $\mu_b \approx 400$ MeV and T ≈ 160 MeV (Figure 1.4), while other models do not reach a critical point. The area of the QCD phase diagram around the critical point will be investigated at the Compressed Baryonic Matter (CBM) experiment with the future FAIR accelerator at GSI. The ALICE experiment at the LHC will probe the QCD phase diagram at high temperatures and almost vanishing baryo-chemical potential, where it is believed that the transition to the QGP will occur as a crossover.

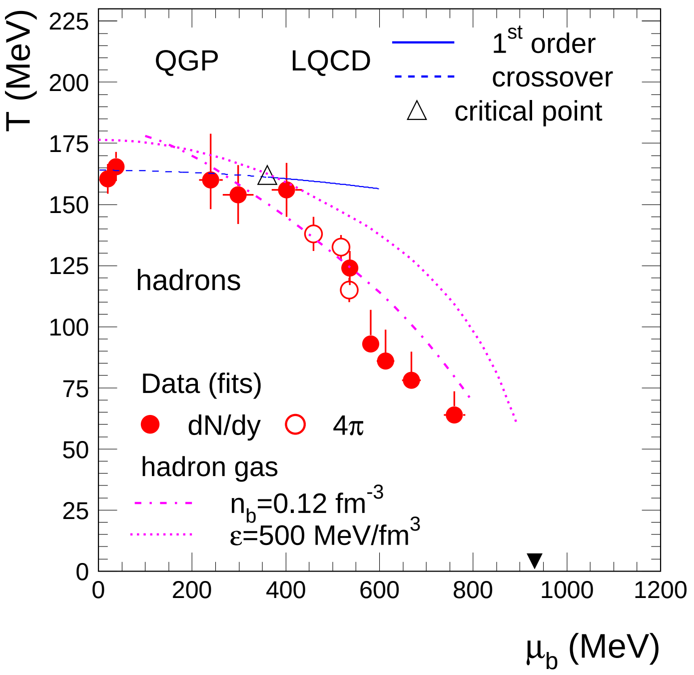

Figure 1.4: Results of lattice QCD calculations are shown together with experimental data for the chemical freeze-out, from [8]. The predicted critical point is marked by the open triangle. The location of ground state nuclear matter (atomic nuclei) is indicated by the full triangle.

1.2 Probes for the quark gluon plasma

1.2.1 Dileptons

Dilepton production is an important tool for measuring the temperature and the dynamical properties of the matter produced in a relativistic heavy-ion collision. Lepton pairs are emitted throughout the evolution of the system. Specifically, these are prompt contributions from hard nucleon–nucleon collisions, thermal radiation from the QGP and hot hadronic phases as well as final-state meson decays after freeze-out.

At higher lepton p_t, bottom decays will dominate the single lepton rate. The charm and bottom rates can also be measured in $e\mu$ coincidence studies. Thus, although the heavy quark cross sections still suffer from theoretical uncertainties, measurements of high mass lepton pairs and large p_t single leptons can reduce these uncertainties as well as provide valuable information about heavy quark energy loss and the nuclear gluon distribution.

1.2.2 Charm and bottom production

The measurement of open charm and open beauty production allows to investigate the mechanisms of heavy-quark production, propagation and, at low momenta, hadronisation in the hot and dense medium formed in high-energy nucleus–nucleus collisions.

The open charm and open beauty cross sections are also needed as a reference to measure the effect of the transition to a deconfined phase on the production of quarkonia. In fact, since at LHC energies heavy quarks are mainly produced through gluon–gluon fusion processes (gg $\to Q\overline{Q}$), the Drell–Yan process (q$\overline{\text{q}}$ $\to \ell^+\ell^-$) does not provide an adequate reference, besides having a very small cross section at these energies; a direct measurement of the D and B mesons yields would provide a natural normalization for charmonia and bottomonia production. Finally, the measurement of B meson production is necessary in order to estimate the contribution of secondary J/ψ (from B $\to$ J/$\psi + X$) to the total J/ψ yield.

Heavy-quark production in nucleus–nucleus collisions at high energy

Heavy quarks are produced in the early stage of the collision in primary partonic scatterings with large virtuality Q and, thus, on temporal and spatial scales, $\Delta\tau \sim \Delta r \sim 1/Q$, which are sufficiently small for the production to be unaffected by the properties of the medium, in the case of nucleus–nucleus collisions. In fact, the minimum virtuality $Q_{\min} = 2\, m_Q$ in the production of a $Q\overline{Q}$ pair implies a space time scale of $\sim 1/(2\, m_Q) \simeq 1/2.4\ \text{GeV}^{-1} \simeq 0.1$ fm/c (for charm), to be compared to the expected lifetime of the QGP phase at the LHC, > 10 fm/c. Thus, the initially-produced heavy quarks experience the full collision history.

Parton energy loss for heavy quarks in nucleus–nucleus collisions

While traversing the dense matter produced in nucleus–nucleus collisions, the initially-produced hard partons lose energy, mainly on account of multiple scatterings and medium-induced gluon radiation, and become quenched.

In a simplified picture, an energetic parton produced in a hard collision undergoes, along its path in the dense medium, multiple scatterings in a Brownian-like motion with mean free path λ, which decreases as the medium density increases. In this multiple scattering process, the gluons in the parton wave function pick up transverse momentum with respect to its direction and they may eventually 'decohere' and be radiated.

	Charm			Bottom		
System	pp	pPb	Pb–Pb	pp	pPb	Pb–Pb
Centrality	min.-bias	min.-bias	centr. (5%)	min.-bias	min.-bias	centr. (5%)
$\sqrt{s_{\text{NN}}}$	14 TeV	8.8 TeV	5.5 TeV	14 TeV	8.8 TeV	5.5 TeV
$N^{Q\overline{Q}}$/ev	0.16	0.78	115	0.0072	0.029	4.56

Table 1.1: Summary table of the production yields in pp, pPb, and Pb–Pb collisions, from[17].

Yields in proton–proton and Pb–Pb collisions

A summary of the production yields in the three considered colliding systems (pp, pPb and Pb–Pb) is presented in Table 1.1. One obtains 0.16 c$\overline{\text{c}}$ pairs and 0.0072 b$\overline{\text{b}}$ pairs per event in pp. In Pb–Pb collisions the yield is 115 $c\overline{c}$ pairs and 4.56 $b\overline{b}$ pairs per event.

Charm and bottom detection via e–μ coincidences

The $c\overline{c}$ and $b\overline{b}$ production cross sections could be measured in ALICE from unlike-sign electron–muon pairs where the electron is identified in the central barrel ($|\eta| < 0.9$) and the muon is detected in the forward muon spectrometer ($-4 < \eta < -2.5$). The e–μ channel is the only leptonic channel that gives a direct access to the correlated component of the $c\overline{c}$ and $b\overline{b}$ pairs. Indeed, in contrast to e^+e^- and $\mu^+\mu^-$ channels, neither a resonance, nor direct dilepton production, nor thermal production can produce correlated e–μ pairs.

Measurement of J/ψ's from B meson decays

B mesons decay into J/ψ mesons with a branching ratio of about 1%. Since B mesons are produced by a factor of 5 more abundantly than J/ψ mesons, and since direct J/ψ production might be further suppressed by QGP effects, secondary J/ψ mesons are conceivably contributing a large fraction to the observable J/ψ signal.

The interest for developing a procedure to measure the production of secondary J/ψ's is clearly two-fold. First, they will provide a sensitive measurement of the B meson production cross section, that use the semi-leptonic decay channel — $B \rightarrow J/\psi + X$ has become the standard decay channel to study beauty production in $p\overline{p}$ collisions at the Tevatron. Second, the identification and reconstruction of secondary J/ψ mesons is essential to investigate medium effects on primary charmonia. This is particularly important for the p_t dependence of the J/ψ signal, since J/ψ's from B meson decays exhibit a much harder transverse momentum spectrum than the primary one. At large transverse momentum the ratio of primary to secondary J/ψ's may grow as large as 1/1. A trustworthy physics interpretation of the measured J/ψ production can clearly only be given once the secondary contribution is quantitatively known, see Figure 1.6.

1.2.3 Quarkonium production

Heavy quarks (charm and bottom) provide sensitive probes of the collision dynamics at both short and long timescales. On the one hand, heavy-quark production is an intrinsically perturbative phenomenon which takes place on a timescale of the order of $1/m_Q$ where m_Q is the heavy-quark mass. On the other hand, the long lifetime of charm and bottom quarks allows them to live through the thermalisation phase of the plasma and to possibly be affected by its presence. Less than one percent of all heavy-quark pairs form quarkonium bound states. Finally, heavy-quark–antiquark pairs can form quarkonium states which are bound by energies of the order of a few hundred MeV. These binding energies are comparable in size to the mean energies ($\sim 3T_c$) of the plasma, implying a large probability for quarkonium breakup.

The quarkonium yields at central Pb–Pb collisions ($b = 0$) for one month, 10^6 s, run at the LHC, are $\simeq 10^8$ J/ψ and $\simeq 5 \times 10^5$ Υ resonances. These rates are sufficiently copious for high-statistics measurements at the LHC before suppression is accounted for. Therefore, quarkonium suppression should be measurable to fairly high accuracy, even for the Υ family.

The more tightly bound quarkonium states with lower masses, the J/ψ, Υ, $\chi_{\rm b}$(1P), and the Υ', survive as $T_{\rm c}$ is approached and need a deconfined medium for dissociation. The J/ψ, Υ' and $\chi_{\rm b}$(1P) should dissociate already at $T \sim 1.1T_{\rm c}$. The most tightly bound quarkonium state, the Υ, will not be suppressed below $T \sim 2.3T_{\rm c}$. According to estimates of the initial temperatures at the LHC, Υ suppression should indeed be possible.

It is worthwhile noting that secondary production will be at lower centre-of-mass energies than the initial nucleon–nucleon collisions. Thus the production kinematics will be different, leading to narrower rapidity and $p_{\rm t}$ distributions. Secondary quarkonium could be separated from the primary quarkonium, subject to suppression, by appropriate kinematic cuts. Such cuts will also be useful for separating initial J/ψ's from those produced in B-meson decays.

Where higher centre-of-mass energies are available (RHIC and LHC), the study of charmonia is subject to significant differences with respect to the SPS energies. In addition to prompt charmonia produced directly via hard scattering, secondary charmonia can be produced according to different mechanisms which might result in an enhancement instead of a suppression of charmonium states, as predicted in Figure 1.5. Secondary charmonium production can occur both as a consequence of QGP formation (kinetic recombination during the hadronic phase (bottom decay and D$\overline{\rm D}$ annihilation).

At LHC, the much higher energy offers the possibility of measuring with 'significant' statistics the bottomonium yields thus providing an additional probe for QGP studies. In fact, since the Υ (1S) dissolves only above the critical temperature, at a value which should not be reached at RHIC, the spectroscopy of the Υ family at LHC energies should reveal an unique set of information on the characteristics of the QGP.

However, new problems arise in the study of charmonium production at LHC. First of all, in the dense medium produced in a heavy ion reaction, energy loss of heavy quarks might substantially modify the spectra of the decay particles: this implies that the study of quarkonium production must be combined to the study of open heavy flavours. Moreover, the choice of the reference process for the normalization of the quarkonia signal is not obvious, and the fraction of J/ψ originated from B decay has to be taken into account. Finally, the quarkonium signals will be sitting on top of a complex combinatorial background, mainly coming from open charm and open bottom decay, see Figure 1.6.

Quarkonium states will be identified in the dielectron and the dimuon channel respectively in the central and in the forward region. Open charm and bottom will be measured in the hadronic and semi-leptonic decay channels of heavy mesons.

Quarkonia detection in ALICE

The excellent vertexing capabilities of the ALICE barrel detectors can be used in conjunction with electron identification in the TRD to discriminate prompt from secondary J/ψ originating from B decay. The latter are in fact produced at large distances from the primary vertex and can therefore be selected by identifying $\rm e^+e^-$ pairs with displaced vertex.

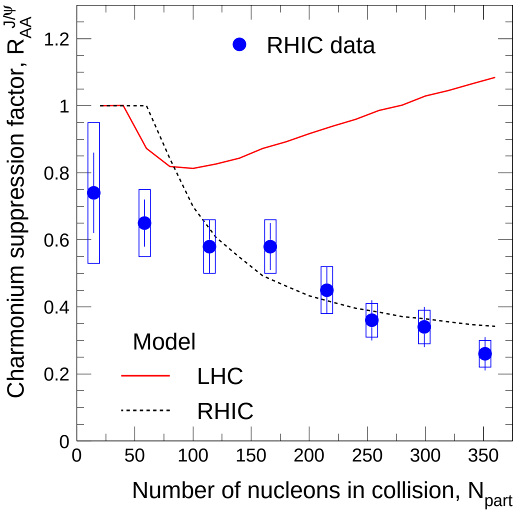

Figure 1.5: Statistical model predictions of charmonium production at RHIC and LHC energies, compared to RHIC data, from [9].

At LHC, thanks to the higher temperatures and energy densities reached in the collision, prompt J/ψ's are expected to be almost fully suppressed in central collisions. This is compensated by the J/ψ enhancement due to kinetic recombination or statistical hadronization. In fact, with respect to the scenarii without any suppression, charmonium yields at least two or three times larger are predicted for central Pb–Pb collisions, as detailed in Figure 1.5. This would be a clear signature of QGP formation.

In ALICE di-muon decays of J/ψ will be studied with the muon spectrometer, while the detectors of the central barrel will observe the di-electron channel. Due to the small cross section for di-lepton decays of quarkonia and a huge amount of background, dedicated detectors are required to identify di-leptons and to enhance their yield during data-taking. The TRD with its L1-trigger capability on high transverse momentum charged particles is the key element to collect sufficient statistics in the di-electron channel. Open charm is an important measurement and can contribute to the background in the J/ψ measurement, Figure 1.6 shows a simulation of the di-electron invariant mass spectrum. Leptons from open charm decays can be identified and removed from the background with the secondary vertex information provided by the Inner Tracking System (ITS). Without the pion rejection from the TRD the J/ψ signal would barely be visible in the background. Combined particle ID capabilities from TPC and TRD give enough statistics to measure J/ψ, Υ(1S) and Υ(2S) with good signal to background ratio and significance, according to [10].

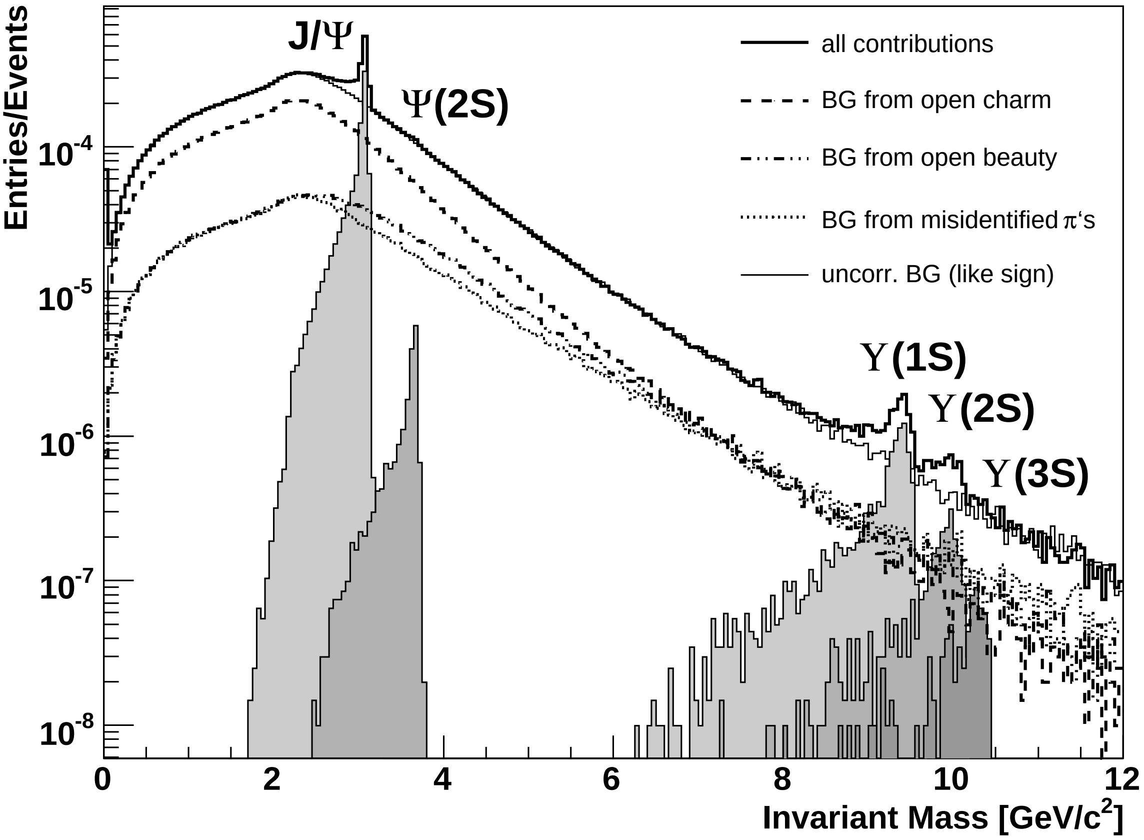

Figure 1.6: The normalised di-electron invariant mass spectrum, 2×10^8 simulated central events ($dN_{ch}/d\eta = 3000$), representing the statistics for one nominal ALICE running year, from [10].

1.3 The Large Hadron Collider

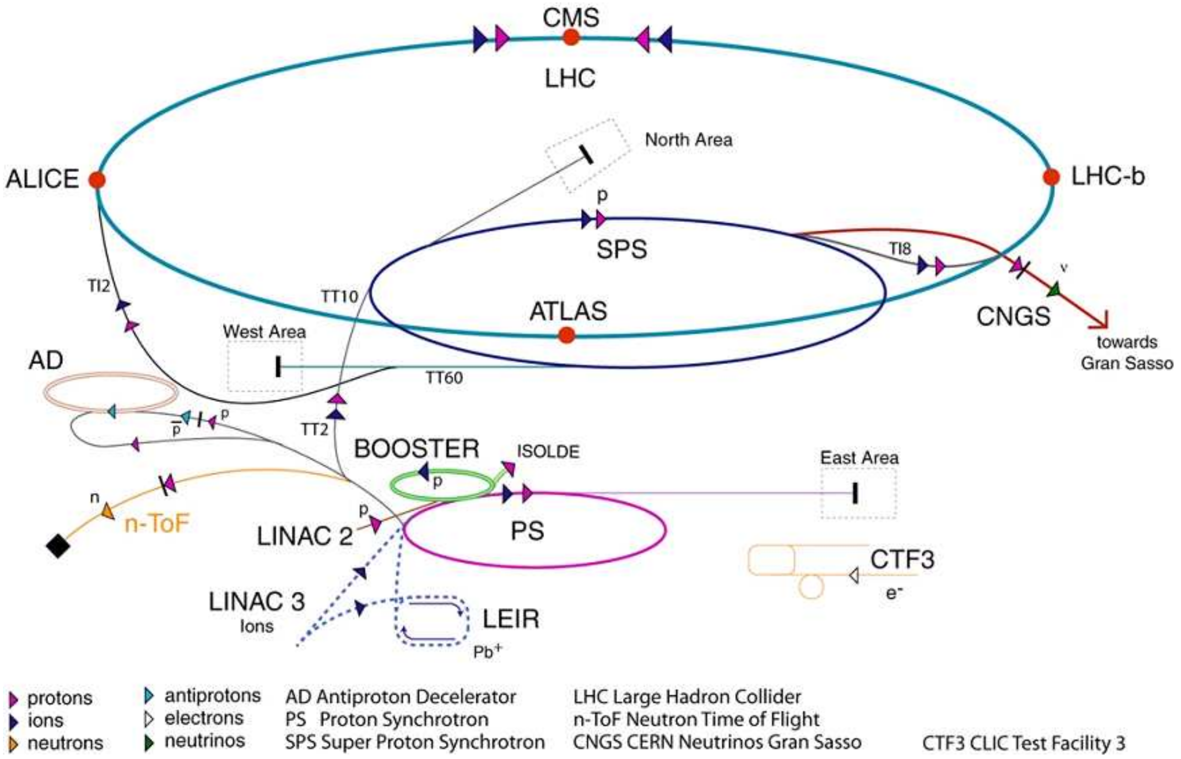

Figure 1.7: Schematic overview of the CERN accelerator complex. Particles are passing through a chain of four pre-accelerators prior to injection into the LHC ring, [CERN].

The Large Hadron Collider (LHC) at CERN, the European Organization for Nuclear Research, near Geneva is the world's most powerful particle accelerator. It is designed to collide two counter-rotating proton beams at an unprecedented centre of mass energy $\sqrt{s}$ of 14 TeV and a luminosity of $L=10^{34}\text{cm}^{-2}\text{s}^{-1}$. The LHC can also operate as a heavy-ion machine, colliding fully stripped $^{208}\text{Pb}^{82+}$ions with a centre of mass energy per nucleon pair $\sqrt{s_{\text{NN}}}$ of 5.5 TeV and a peak luminosity of $L=10^{27}\text{cm}^{-2}\text{s}^{-1}$. The first proton collisions in the LHC are scheduled for the end of 2009.

The LHC is installed in the former tunnel of the Large Electron Positron (LEP) collider measuring 26.7 km in circumference, located between the Jura mountain range and Lake Geneva. It has an octagonal shape with eight arcs and eight approximately 528 m long straight sections, Table 1.2 gives more details on the LHC geometry. Due to the high beam intensities implied by the anticipated luminosity, the LHC could not be realised as a proton anti-proton machine with one common vacuum and magnet system for both circulating beams. The use of two counter-rotating equally charged particle beams requires opposite magnet dipole fields for each ring. As there is not enough room for two separate rings of magnets in the LHC tunnel, the LHC uses twin bore magnets consisting of two sets of coils and beam channels within the same mechanical structure and cryostat. Common beampipes are used only close to the four experimental insertion regions, these are ATLAS, ALICE, CMS and LHCb at Point 1,

Geometry			
		Injection	**Collision**
Ring circumference	(m)	26658	
Ring separation in arcs	(mm)	194	
Number of quadrupoles		392	
Number of dipoles		1232	
Length of dipoles	(m)	14.3	
Dipole magnet mass	(t)	27.5	
Field of dipoles	(T)	0.54	8.33
Current in dipoles	(A)	763	11850
Bending radius	(m)	2803.95	
Revolution frequency	(kHz)	11.245	

Table 1.2: LHC geometry and properties, from [12].

Design p–p Beam parameters			
		Injection	**Collision**
Proton energy	(GeV)	450	7000
Relativistic γ		479.6	7461
Number of particles per bunch		1.15×10^{11}	
Number of bunches (max. 3564 possible)		2808	
Nominal bunch spacing	(ns)	25	
Circulating beam current	(mA)	582	
Stored energy per beam	(MJ)	23.3	362
RMS bunch length	(cm)	11.24	7.55
Peak luminosity in IP1 and IP5	($\mathrm{cm}^{-2}\mathrm{s}^{-1}$)	-	1.0×10^{34}
Events per bunch crossing		-	19.02
Peak luminosity in IP2	($\mathrm{cm}^{-2}\mathrm{s}^{-1}$)	-	5.0×10^{30}

Design Pb–Pb Beam parameters			
		Injection	**Collision**
Lead ion energy	(GeV)	36900	574000
Lead ion energy/nucleon	(GeV)	177.4	2759.
Relativistic γ		190.5	2963.5
Number of ions per bunch		7.0×10^{7}	
Number of bunches		592	
Peak RF voltage (400 MHz system)	(MV)	8	16
RMS bunch length	(cm)	9.97	7.94
Circulating beam current	(mA)	6.12	
Stored energy per beam	(MJ)	0.245	3.81
RMS beam size at IP2	(μm)	280.6	15.9
Peak luminosity at IP2	($\mathrm{cm}^{-2}\mathrm{s}^{-1}$)	-	1.0×10^{27}

Table 1.3: LHC beam parameters for proton-proton and lead-lead running, from [12].

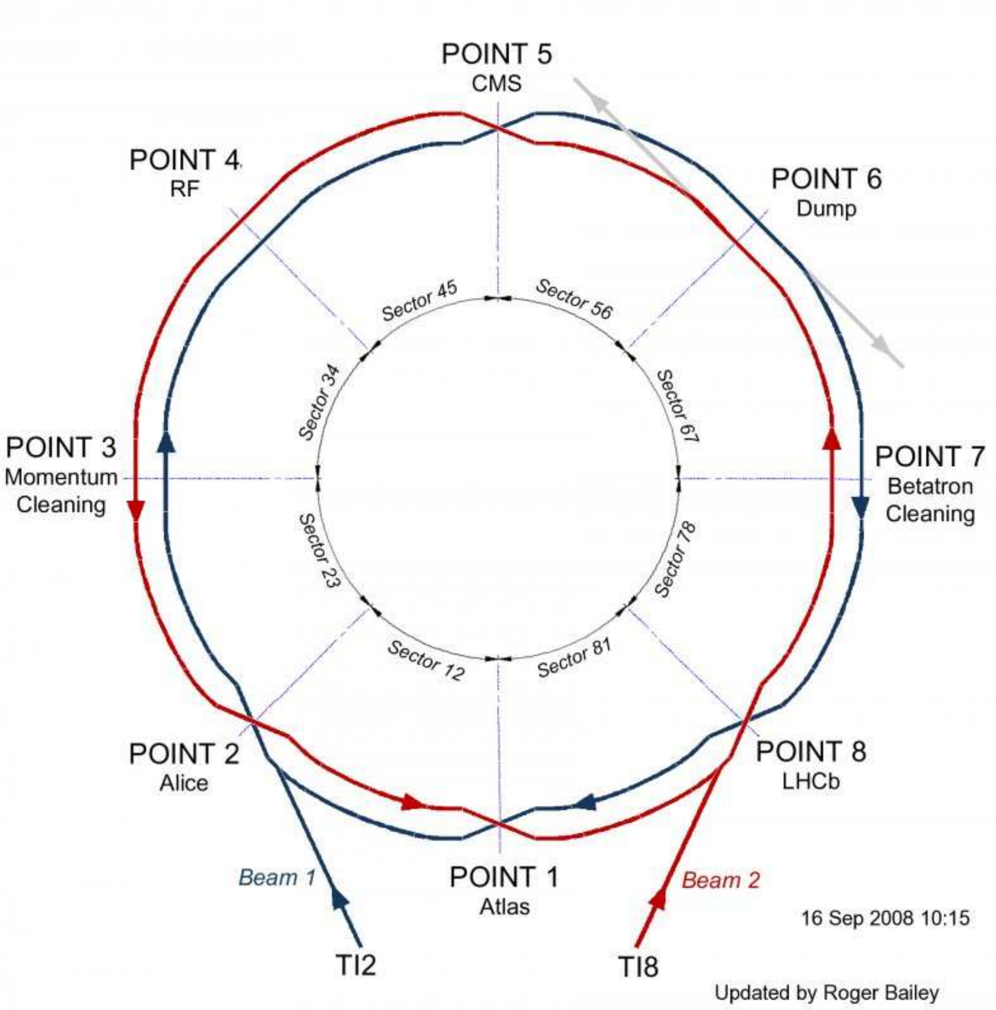

Figure 1.8: The two beams circulating in the LHC cross each other in 4 intersection Points. Beam 1 (blue) is injected in Sector 12 and runs clockwise. Beam 2 (red) is injected in Sector 81 and runs counter-clockwise. The accelerating RF cavities are installed at Point 4 while the beam dump is located at Point 6. Beam collimation takes place at Points 3 and 7, [CERN].

2, 5 and 8 respectively (see Figure 1.8). It is necessary to use superconducting magnet technology to keep the beams on orbit at 7 TeV proton energy. A total of 1232 dipole magnets (Figure 1.9) guide the beams once around the ring, they achieve a nominal dipole field of 8.33 T at currents of 11.8 kA. Machine infrastructure is located in the four long straight sections which are not used by the experiments. Two independent radio frequency systems installed at Point 4 are used for individual beam capture and acceleration. The insertions at Point 3 and 7 contain collimation systems and perform longitudinal and transversal beam cleaning. Point 6 accommodates the beam dump system, where both beams can be vertically ejected and dumped in a controlled way onto dedicated targets. ATLAS and CMS will operate at peak luminosity during pp, for ALICE it will be tuned to $L=5 \times 10^{30}\mathrm{cm}^{-2}\mathrm{s}^{-1}$. Table 1.3 gives more details on the different LHC beam parameters. The LHC relies on part of the existing CERN

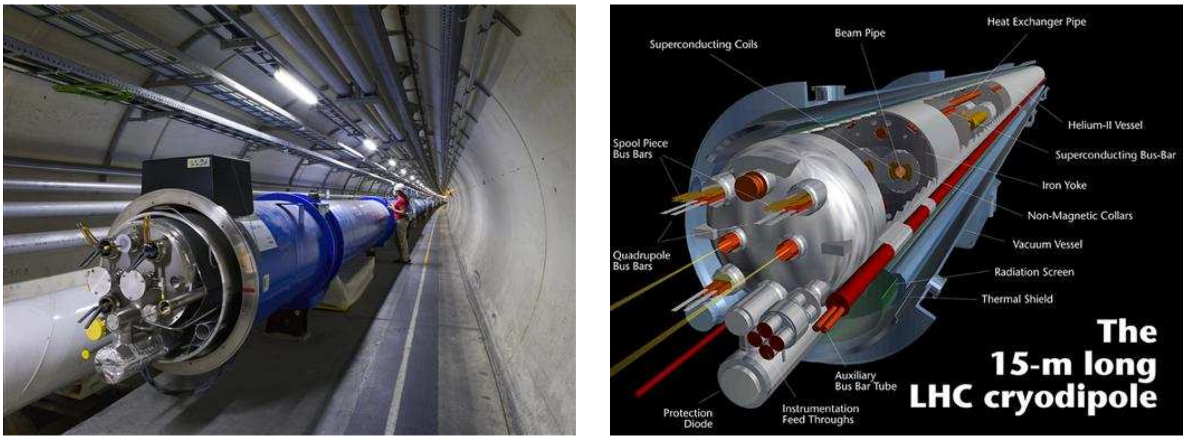

Figure 1.9: The LHC dipole magnet, left panel: during installation in the tunnel, right panel: schematical drawing. 1232 dipole units are installed in the LHC ring, from [16].

infrastructure (Figure 1.7) as pre-accelerator. In pp mode the LHC will be supplied with protons from the injector chain Linac2 (50 MeV) – Proton Synchrotron Booster (PSB) (1.4 GeV) – Proton Synchrotron (PS) (26 GeV) – Super Proton Synchrotron (SPS) (450 GeV).

Heavy ion collisions between beams of fully stripped lead ions ($^{208}\mathrm{Pb}^{82+}$) are planned for one year after the start-up of the collider with protons. The nominal magnetic field of 8.33 T in the dipole magnets, allows an ion beam energy of 2.76 TeV/nucleon, yielding a total centre-of-mass energy $\sqrt{s_{\mathrm{PbPb}}}$ of 1.15 PeV. The typical running schedule within a year consists of 8 month pp operation followed by 1 month of heavy-ion collisions and 3 month of shutdown. In later years it is foreseen to collide p–Pb like systems and lighter ions (Ar–Ar) to study energy density dependencies and cold nuclear matter effects.

The pre-accelerators were upgraded to meet the needs of the LHC, but they were not initially designed for the task of LHC injector. A complicated sequence of beam transfers between the different pre-accelerator stages finally allows to fill 2808 bunches out of 3564 possible bunch places. For a future LHC luminosity or energy upgrade to "Super-luminosity" LHC (SLHC) (up to $\mathrm{L}=10^{35}\mathrm{cm}^{-2}\mathrm{s}^{-1}$) or "Double energy" LHC (DLHC) (14 TeV beam energy) the construction of a new pre-accelerator chain is being discussed. It would involve the Linac4 (160 MeV), the Superconducting Proton Linac (SPL) (4 GeV), the High Energy PS (PS2) (50 GeV) and an upgraded Superconducting SPS (SPS+) (1 TeV).

1.4 ALICE - A Large Ion Collider Experiment

A Large Ion Collider Experiment (ALICE) is the only dedicated heavy-ion experiment at the CERN LHC. It was designed to track and identify particles from nucleus-nucleus collisions over a broad momentum range, from rather low momenta of 100 MeV/c up to 100 GeV/c. It will allow to investigate the physics of the quark gluon plasma at extreme values of temperature and energy density. A photo of ALICE, fully assembled for the initial start-up of the LHC in autumn 2008, is shown in Figure 1.10.

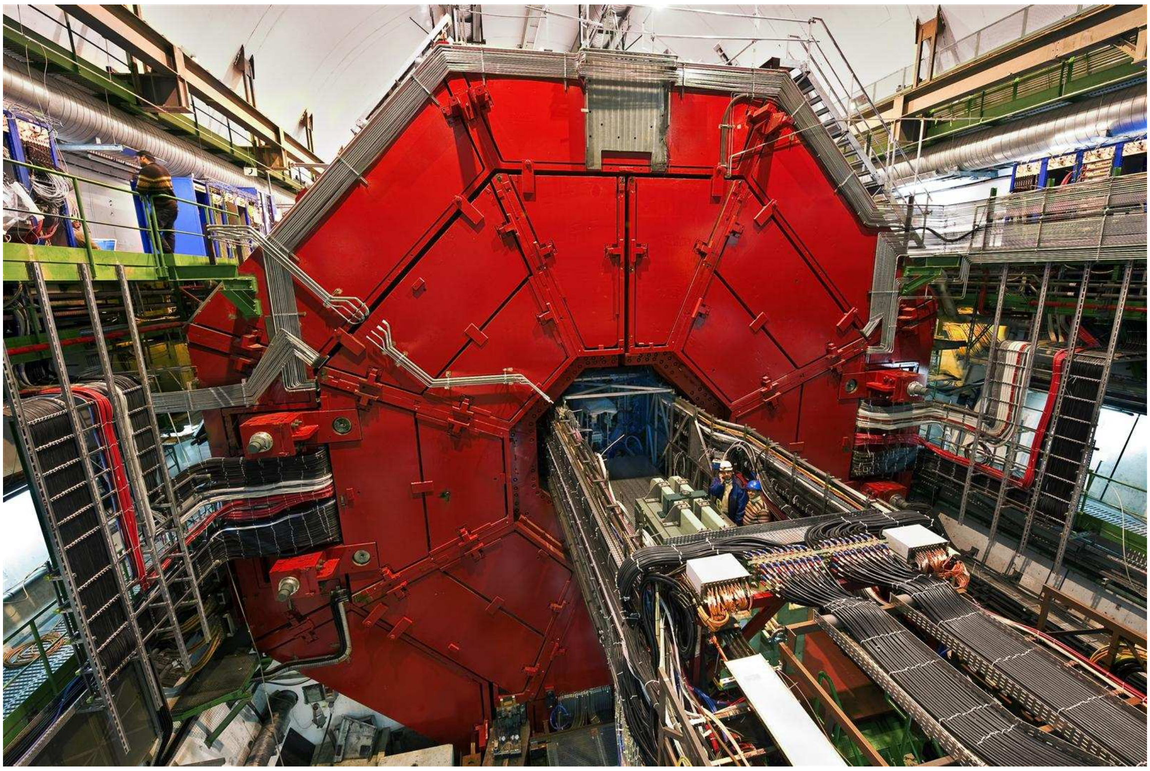

Figure 1.10: Photo of the ALICE detector with magnet doors closed and ready for beam, from [16].

The dominating element in the ALICE cavern is the red, octagonal shaped solenoid magnet. It is the world's largest volume conventional magnet, operating at 0.5 T maximum field strength and inherited from the former LEP L3 experiment. The overall dimensions of the ALICE detector are 16 m × 26 m × 16 m with a total weight of approximately 10 000 t.

ALICE consists of a central barrel part and a muon spectrometer, as illustrated in Figures 1.11 and 1.12. The central barrel fits inside the solenoid magnet and measures hadrons, electrons and photons at mid-rapidity in the range of $|\eta| \leq 0.9$. The muon spectrometer consists of a large warm dipole magnet and 14 tracking and triggering stations in direction of beam 1. It covers a large domain of rapidity ($-4.0 \leq \eta \leq -2.4$). A massive conical absorber structure installed between the interaction point and the dipole magnet acts as muon filter, reducing the hadronic background. The barrel is completed by forward detectors located at large rapidities to provide an interaction trigger and to characterize the event. The Forward Multiplicity Detector (FMD), V0 and T0 detectors cover a wide acceptance in the forward and backward region ($-3.4 \leq \eta \leq -1,7$ and $1,7 \leq \eta \leq 5.1$) for the measurement of charged particle multiplicity and triggering.

The ALICE design luminosity for Pb–Pb collisions corresponds to an interaction rate of 8kHz, for the 10% most central collisions an extreme multiplicity of $\mathrm{d}N_{\mathrm{ch}}/\mathrm{d}\eta = 8000$ has been assumed, corresponding to 14400 charged particle tracks in the acceptance of the TPC.

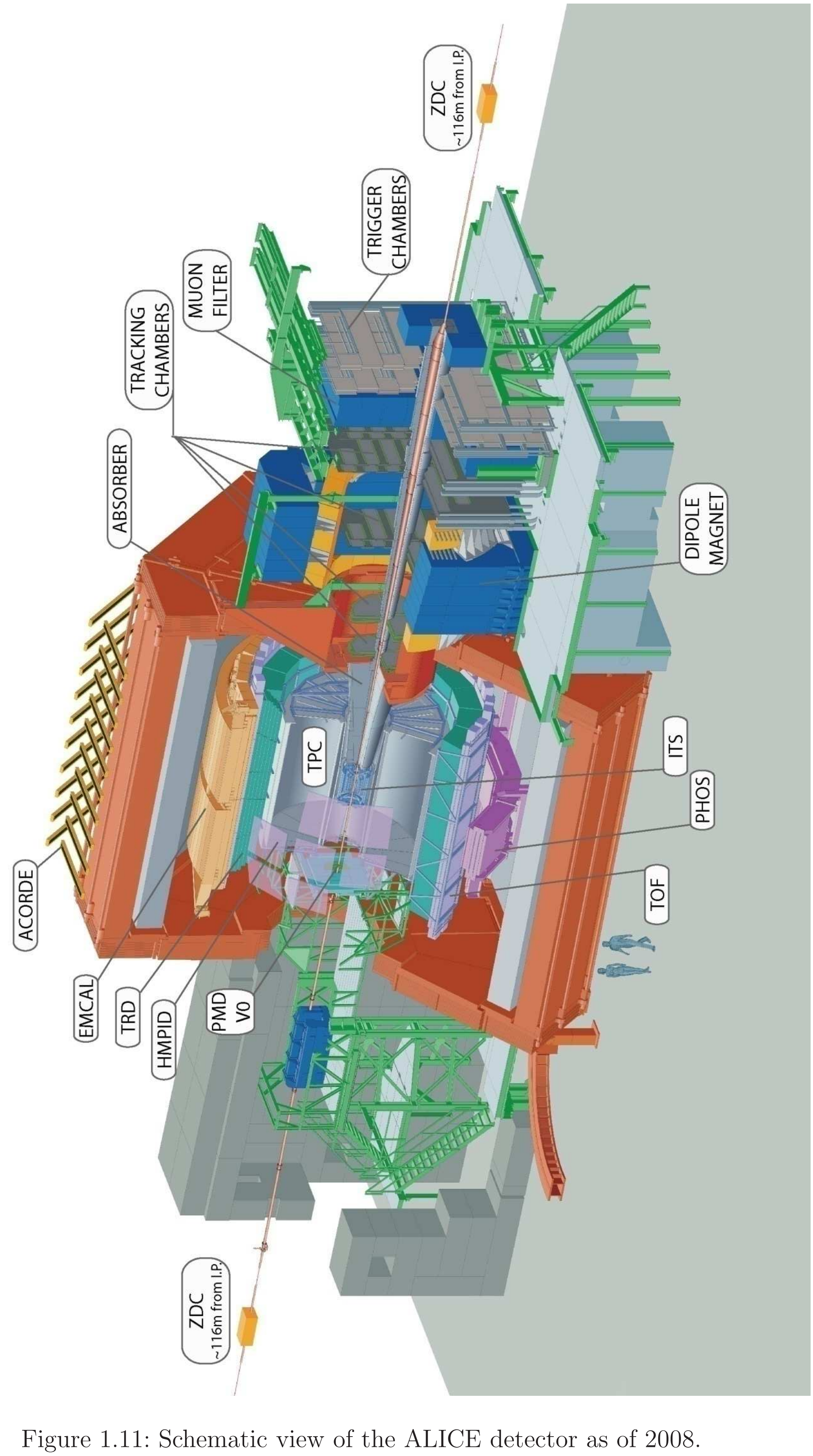

Figure 1.11: Schematic view of the ALICE detector as of 2008.

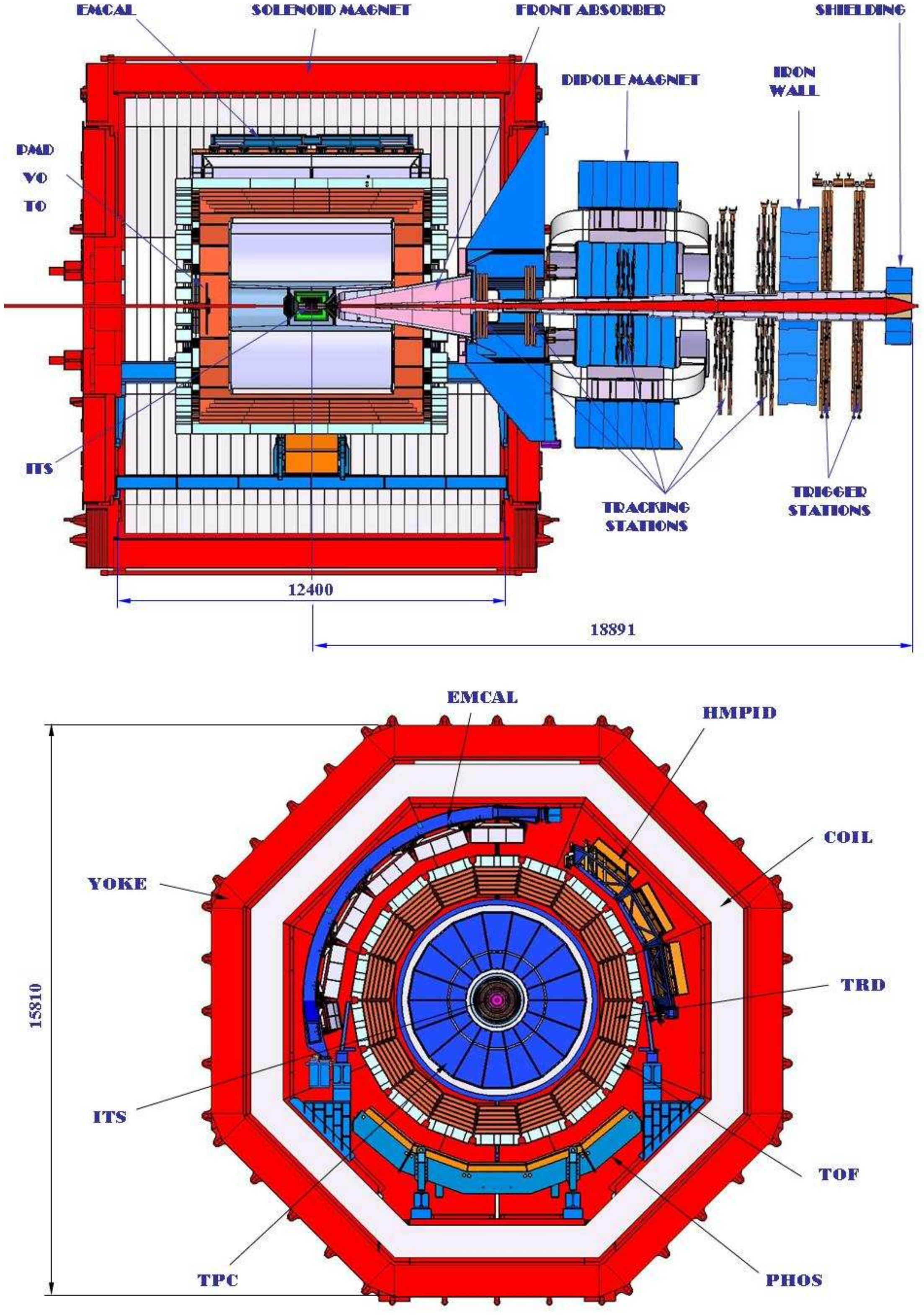

Figure 1.12: 2-dimensional cut views of the ALICE detector. Upper panel : cut along the $yz-$ direction, view from the LHC center. Lower panel : cut along the $xy-$ direction, view in direction of beam 1, from [19].

1.4.1 The ALICE coordinate system

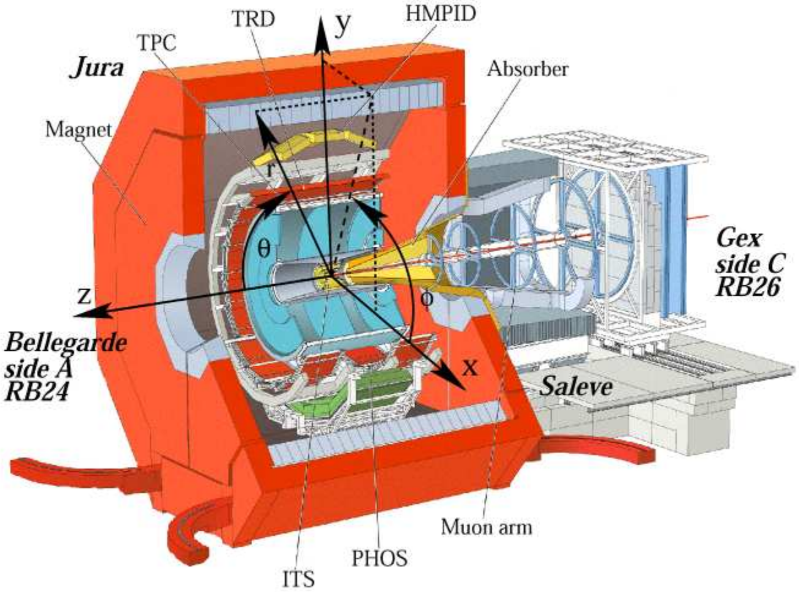

Figure 1.13: Definition of the ALICE coordinate system, from [23].

The ALICE coordinate system (Figure 1.13) is defined as follows : The origin of the right-handed coordinate system is located at the interaction point. The x-axis is pointing horizontally towards the LHC center, the y-axis is oriented upwards and the z-axis points along the beam, away from the muon arm, in direction of beam 2.

1.4.2 Detectors in the central barrel

A few ALICE subdetectors related to the TRD will be presented in the following section, these are either used in combined tracking or as trigger detectors. For a more detailed overview of the various subdetectors in ALICE, please consult [19]. All detectors in the central barrel cover the $|\eta| \leq 0.9$ rapidity range and 2π in azimuth, except HMPID, PHOS, and EMCal, located radially outside the TOF barrel and offering only a partial coverage in η or ϕ.

ITS The Inner Tracking System consists of three individual silicon subdetectors, each contributing 2 layers, which are cylindrically arranged around the interaction point : the Silicon pixel detector (SPD), the Silicon drift detector (SDD) and the Silicon strip detector (SSD). The ITS can detect very low momentum tracks, down to 100 MeV/c. It can localise the primary vertex with a resolution better than 100 μm. Thanks to the high spatial resolution of the SPD, secondary vertices from D and B mesons as well as hyperons can be reconstructed.

TPC The Time-Projection Chamber is the main tracking device of the ALICE central barrel. It is built as a high-granularity detector to cope with the initially anticipated extreme particle multiplicity, new multiplicity estimates are much lower. The TPC has a cylindrical shape, an overall length of 500 cm, an inner radius of about 85 cm and an outer radius of about 250 cm. With an active volume of 95 m^3 it is the biggest TPC in the world. Charged-particle momentum measurements with good two-track separation are provided as well as particle identification through energy loss and vertex determination together with the ITS. With 2.5 m drift length, the drift time takes 88 μs. A gating grid separates the drift region from the amplification region, opening only upon a L1 trigger signal from a trigger detector, for example the TRD. The limiting factor for the trigger rate is still the space charge due to ion back-drift, the TPC is expected to operate at a maximum trigger of 200 Hz in Pb–Pb and 1 kHz in pp mode. Simulations in Figure 1.14 show a standalone TPC tracking efficiency of more than 90% at $\mathrm{d}N_{\mathrm{ch}}/\mathrm{d}\eta = 6000$. In combination with the ITS and TRD a combined p_{t} resolution below 2.5% is achieved, for $p_{\mathrm{t}} < 20$ GeV/c.

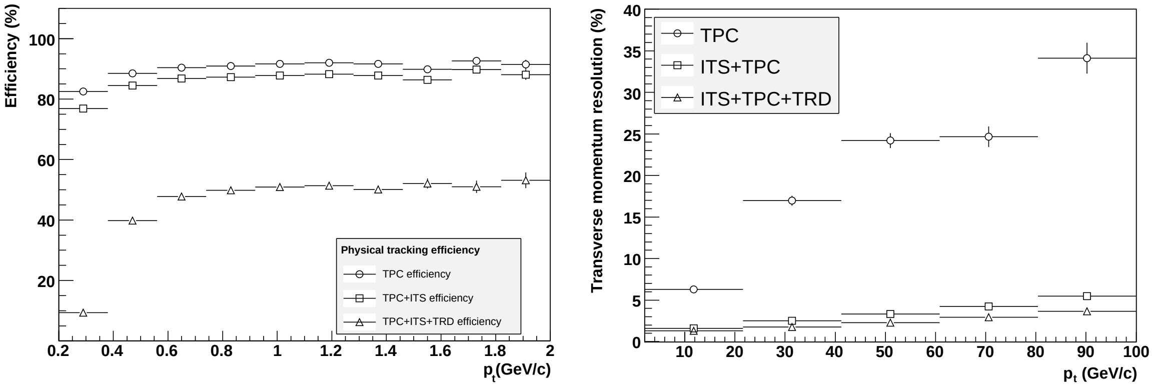

Figure 1.14: Left: Physical track-finding efficiency, Right: Transverse-momentum resolution for different combinations of the tracking detectors (ITS, TPC, TRD) in central Pb–Pb collisions ($\mathrm{d}N_{\mathrm{ch}}/\mathrm{d}\eta = 6000$), from [19].

TRD The Transition Radiation Detector provides electron identification for transverse momenta above 1 GeV/c and serves as fast L1 trigger for events with high-p_{t} electrons. The TRD will be presented in detail in chapter 2.

TOF The Time Of Flight detector is a large array of double stack Multi-gap Resistive Plate Chamber (MRPC) strips. It contributes to the charged particle identification in the intermediate momentum range from 0.2 to 2.5 GeV/c and offers a time resolution below 50 ps. The occupancy at maximum of the assumed charged particle density is smaller than 15%.

HMPID The aim of the High-Momentum Particle Identification Detector is to enhance the particle identification capability for charged hadrons at $p_{\mathrm{t}} > 1$ GeV/c. It is complementary to the energy-loss measurements in the TPC and ITS and the time-of-flight measurements in TOF and allows π/K and K/p separation up to 3 GeV/c and 5 GeV/c, respectively. The HMPID uses seven modules of proximity-focusing Ring

Imaging Cherenkov (RICH) counters in a single arm array, covering 5% of the central barrel acceptance.

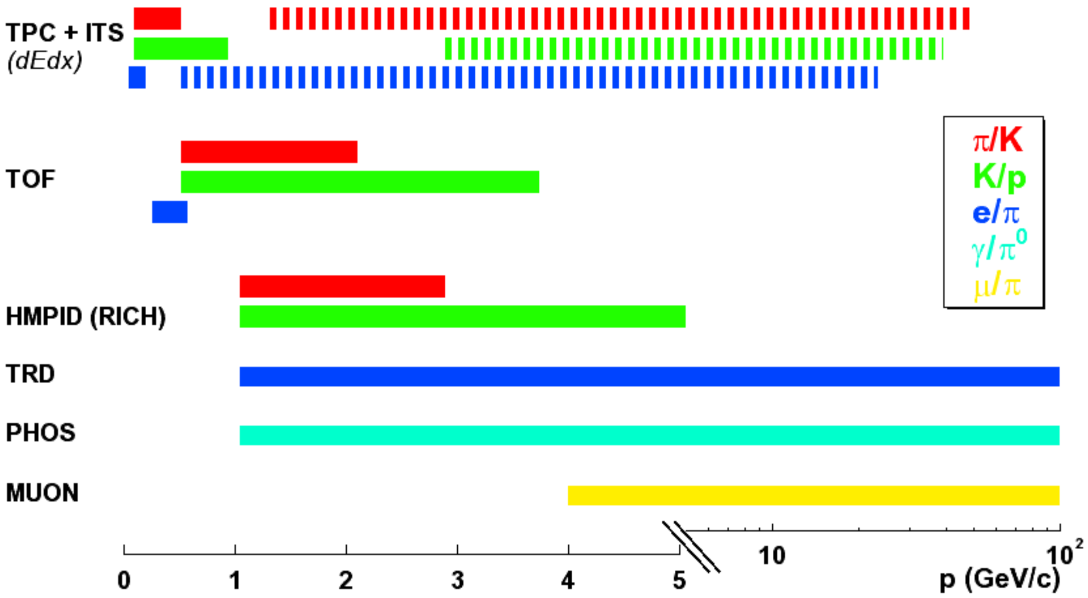

Figure 1.15: Combined particle identification capabilities in ALICE, covering a range from 100 MeV to 100 GeV. Full bars represent a 3σ, dashed bars a 2σ separation of particle types.

PHOS The PHOton Spectrometer is designed as a single-arm high-resolution, high-granularity electromagnetic calorimeter with a timing resolution of a few ns and an additional Charged Particle Veto (CPV) detector. It covers a geometrical acceptance of $|\eta| < 0.12$ and $\Delta\phi = 100°$. PHOS will probe the initial phase of the collision with low-p_t direct photon measurements and study jet quenching by measuring high-p_t π^0 and γ-jet correlations.

EMCal The ElectroMagnetic Calorimeter is a large Pb-scintillator sampling calorimeter with moderate resolution. It measures the energy of photons and electrons with transverse momenta up to 100 GeV/c allowing to focus on jet quenching in heavy-ion collisions. The EMCal can provide L1 triggers for hard jets, photons and electrons. It covers a geometrical acceptance of $|\eta| < 0.7$ and $\Delta\phi = 107°$.

V0 Two arrays of scintillator counters assembled in a disc geometry and installed perpendicular to the beam axis on either side of the interaction point build the V0 detector. It provides minimum bias triggers for the central barrel detectors and further centrality triggers, namely multiplicity, semi-central and central triggers. In pp collisions the V0 can measure the luminosity with a precision of about 10%. The V0 is part of the inputs to the TRD pre-trigger system.

T0 The T0 detector consists of two arrays of 12 Cherenkov counters each, which are cylindrically grouped around the beam pipe on either side of the nominal vertex. It generates a start time for the TOF detector tagging the interaction time with a precision of 50 ps, can also measure the vertex position with a precision of ± 15 mm and generates a L0 trigger. A wake-up signal can be provided to the TRD pre-trigger system prior to L0. The dead-time of the T0 is below the bunch-crossing period of 25 ns in pp collisions.

Chapter 2

The Transition Radiation Detector

2.1 Detector requirements

The Transition Radiation Detector (TRD) was proposed in 1999 to improve the electron identification in the ALICE central barrel at relatively large transverse momenta ($p_{\mathrm{t}} > 1$ GeV/c). At lower momenta electrons can be identified through measurement of specific energy loss in the Time Projection Chamber (TPC). In conjunction with data from the TPC and the Inner Tracking System (ITS) the achieved electron identification allows to measure the production of light and heavy vector meson resonances in the di-electron channel as well as to study the di-lepton continuum in both pp and Pb–Pb collisions. Exploiting the excellent impact parameter resolution of the ITS, it will be possible to determine the overall amount of open charm and open beauty produced in the collision. Directly produced J/ψ mesons can be separated with a similar technique from those resulting from B decay. Furthermore the TRD is designed as a fast trigger for high momentum charged particles. This can be used to significantly enhance the recorded Υ-yields, for the measurement of the high-mass part of the di-lepton continuum as well as jets and for J/ψ detection at high-p_{t}. These physics requirements have resulted in the following design parameters:

Pion rejection capability This is driven by the signal-to-background ratio in the measurement of J/ψ production and its p_{t} dependence. The anticipated pion rejection capability (at 90% electron detection efficiency) is a factor 100 for momenta above 3 GeV/c in central Pb–Pb collisions. The light vector mesons ρ, ω and ϕ as well as the di-electron continuum between the J/ψ and the Υ are only accessible with this level of pion rejection.

Position and momentum resolution The combined momentum resolution of the TPC and the ITS leads to an overall mass resolution of about 100 MeV/c^2 at the Υ-mass (for B = 0.4 T). It is crucial to add electron identification to the tracks with the TRD in order to increase the signal to noise ratio for Υ-resonances and charmonia. To reach this goal the pointing accuracy for electrons needs to be on the level of a fraction of a TPC pad, which will be fulfilled by the anticipated momentum resolution of the TRD of 3.5 (4.7)% at 5 GeV/c (depending on multiplicity), see Table 2.1. At trigger level, a good p_{t} resolution will lead to a sharp trigger threshold.

Pseudo-rapidity coverage	$-0.84 < \eta < +0.84$
Azimuthal coverage	360°
Radial position	2.90 m $< r < 3.68$ m
Overall super module length	7.80 m
Total weight	29.7 tons
Total number of detector modules	540 [522] arranged in 18 super modules
Largest/smallest module	113×145 cm^2 (91×122 cm^2)
Active detector area	694.07 m^2 [674.67 m^2]
Radiator	fibre/foam sandwich, 4.8 cm per layer
Radial detector thickness	$X/X_0 = 23.4\%$
Module segmentation	144 pads in φ 12–16 pads in z
Typical pad size	0.7×8.8 cm^2
Total number of pads	1.18×10^6 [1.15×10^6]
Detector gas	Xe/CO$_2$ (85%/15%)
Gas volume	25.83 m^3 [25.10 m^3]
Depth of amplification region	7 mm
Depth of drift region	30 mm
Drift field	700 V/cm
Drift velocity	15 mm/μs
Longitudinal diffusion	$\mathrm{D}_L = 250\ \mu\mathrm{m}/\sqrt{\mathrm{cm}}$
Transverse diffusion	$\mathrm{D}_T = 180\ \mu\mathrm{m}/\sqrt{\mathrm{cm}}$
Lorentz angle	8° at 0.4 T magnetic field
Number of readout channels	1181952 [1150848]
Time samples in r (drift)	20
ADC	10 bit, 10 MHz
Number of multi-chip modules	70848 [68976]
Number of readout boards	4104 [3996]
Pad occupancy for $\mathrm{d}N_{ch}/\mathrm{d}\eta = 8000$	34%
Pad occupancy in pp	2×10^{-4}
Space-point resolution at 1 GeV/c in z	2 mm (offline)
in $r\varphi$	400 μm for $\mathrm{d}N_{ch}/\mathrm{d}\eta = 2000$
	(600 μm for $\mathrm{d}N_{ch}/\mathrm{d}\eta = 8000$)
Momentum resolution	$\delta p/p = 2.5\% \oplus 0.5\%(0.8\%)$ p / (GeV/c)
	for $\mathrm{d}N_{ch}/\mathrm{d}\eta = 2000$ ($\mathrm{d}N_{ch}/\mathrm{d}\eta = 8000$)
Pion suppression at 90% e efficiency	better than 100 for p = 1 - 6 GeV/c
Event size for $\mathrm{d}N_{ch}/\mathrm{d}\eta = 8000$	11 MB
Event size for pp	6 kB
Trigger rate limit	100 kHz

Table 2.1: Summary of TRD parameters. Numbers are quoted for 18 full super modules, numbers in square brackets, e.g. [522], denote TRD configuration with holes for PHOS in 3 sectors.

Radiation length It has to be minimized in order to prevent photon conversions resulting in increased occupancy as well as incorrect matching. Small radiation length also reduces the amount of Bremsstrahlung leading to loss of electrons or incorrect momentum determination.

Detector granularity In the bending direction it is driven by the desired momentum resolution. In longitudinal direction it is governed by the required capability to correctly identify and track electrons efficiently through all layers of the detector, even at the highest possible multiplicities. A tracking efficiency of 90% for single tracks is required for the desired quality of the reconstructed di-lepton pair signal. The pads have an average area of about 6 cm^2 to attain the above efficiency. A maximum occupancy of 34% at the highest simulated multiplicity density of $\mathrm{dN_{ch}}/\mathrm{d}\eta = 8000$ is expected, including secondary particles.

2.2 Detector concept

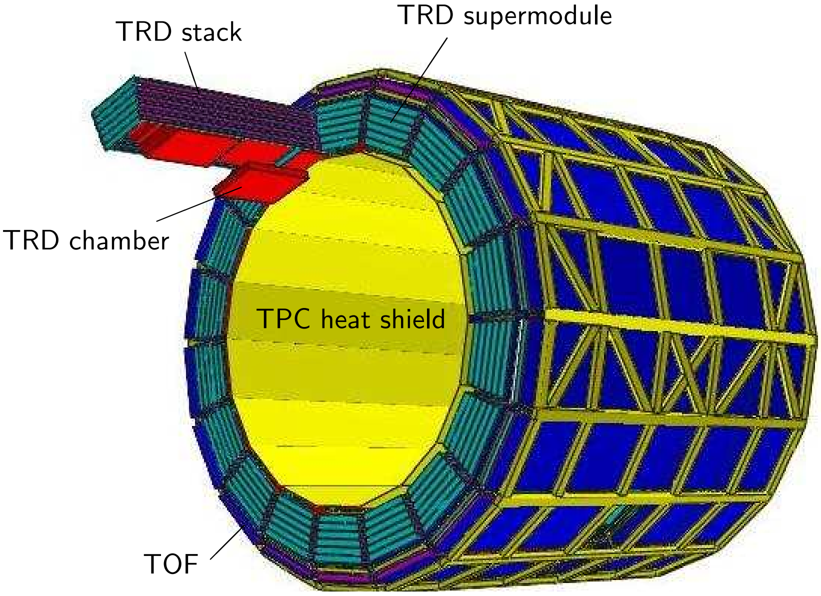

Figure 2.1: Schematic drawing of the TRD installed in the ALICE space frame.

The final design of the TRD, consisting of 522 individual readout detector modules is shown in Figure 2.1. Eighteen super modules (see left panel of Figure 2.2) are arranged in a barrel geometry around the TPC, each containing 30 detector modules grouped in 5 stacks along beam direction and 6 layers in radial direction. The twelve different types of detector modules, varying in their outer dimensions, are arranged as indicated in Table 2.2. In three sectors (13, 14, 15) the central stack (S2) is kept empty to minimise the radiation length in front of the PHOS detector. A summary of the main TRD parameters is given in Table 2.1.

	A-side				C-side
layer 5	L5C1	L5C1	L5C0	L5C1	L5C1
layer 4	L4C1	L4C1	L4C0	L4C1	L4C1
layer 3	L3C1	L3C1	L3C0	L3C1	L3C1
layer 2	L2C1	L2C1	L2C0	L2C1	L2C1
layer 1	L1C1	L1C1	L1C0	L1C1	L1C1
layer 0	L0C1	L0C1	L0C0	L0C1	L0C1
stack	0	1	2	3	4

⟵ z–direction

Table 2.2: Positions of the 12 different chamber types in a TRD super module.

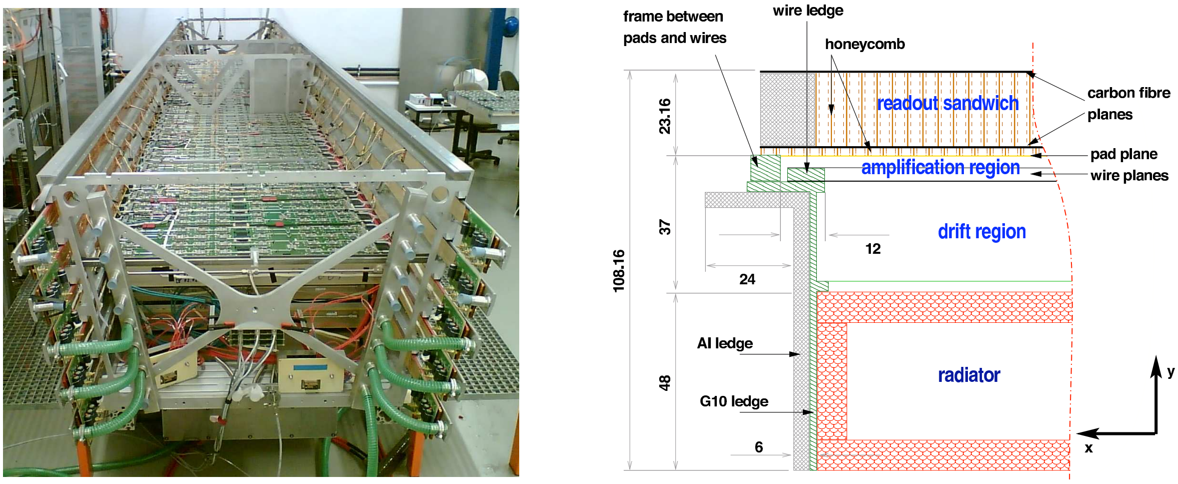

Figure 2.2: Left panel : A super module during assembly with the first three layers installed. Right panel : Schematic cross-sectional drawing of a TRD detector module. Particles originating from the interaction vertex would traverse the chamber from the bottom to the top.

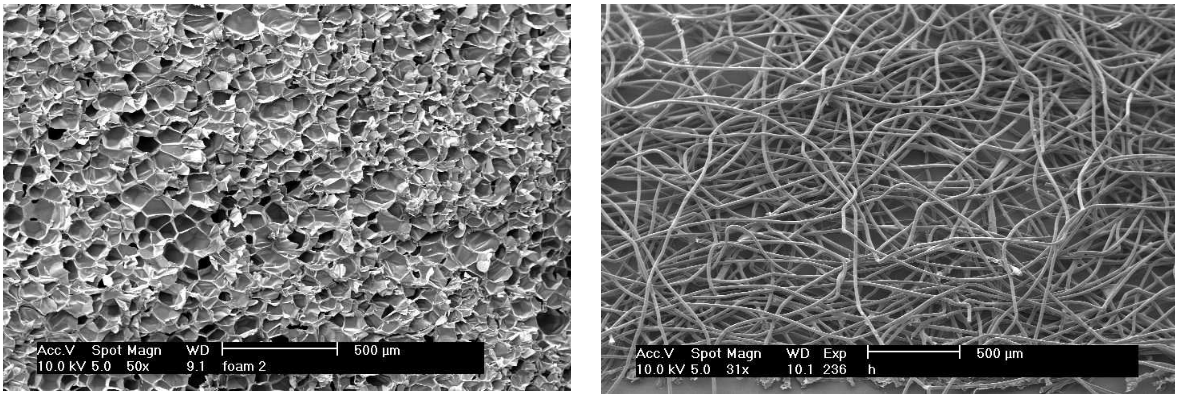

Figure 2.3: Scanning electron microscope images of the irregular radiator materials. Left panel : Rohacell (HF71) foam. Right panel : Polypropylene fibers (Freudenberg LRP375BK).

2.2.1 The readout chambers

Each TRD readout chamber is a full transition radiation detector in itself, a cross-sectional view is visible in the right panel of Figure 2.2. Each detector module comprises the following 3 subcomponents : the radiator, a readout chamber and the back panel sandwich.

The radiator is a composite structure using two different inhomogeneous materials, an electron microscope picture of both is shown in Figure 2.3. The front and back face consist of 8 mm Rohacell foam covered with 0.1 mm carbon fibre laminate. It is filled with irregular polypropylene fibre mats, with an average fibre diameter of 20 μm. The sandwich is covered with sheets of aluminium-coated 25 μm mylar foil, which serves as gas shield and electrode. The radiator is glued into a frame of aluminium L-profiles and fiberglass-epoxy ledges.

wire grid	cathode	anode
material	Cu-Be	Au-plated W
diameter [μ]	75	20
density [g/cm^3]	8.25	19.30
pitch [mm]	2.5	5.0
tension [cN]	100	45
frame load [N/150cm]	600	135

Table 2.3: Properties of the wire grids used for the cathode and anode.

The readout chamber is made up of a conversion and drift gas region of 30 mm thickness and a 7 mm large multi-wire proportional chamber with cathode pad readout. The mylar foil on the radiator surface acts as drift electrode. The drift field is shaped by a field cage integrated into the L-profiles and it is terminated by a plane of cathode wires which is attached to the upper rim of the L-profiles. On top of this grid is a plane of anode wires, providing the necessary gas amplification. The properties of these two wire grids are summarised in Table 2.3. The chamber frame is rigid enough to hold the total wire tension of roughly 735 N. In an equivalent spring load test the maximum deformation of the frame was 280 μm for the sum of the two sides. The deformation of the drift electrode can be kept within the specification of less than 1 mm, even accounting for the additional 1 mbar overpressure in the gas volume.

The back panel, see Figure 2.4, is a 20 mm honeycomb carbon-fibre sandwich supporting the pad planes with an additional 2 mm honeycomb spacer, which ensures a low pad to ground capacitance and guarantees the flatness of the pad surface. At an overpressure of 1 mbar the pad plane is deformed by about 150 μm, which leads to a gain variation of 7%. The pad plane is made of up to three individual printed circuit boards. The chambers in the central stack consist of 12 pad rows (C0-type), all other chambers of 16 pad rows (C1-type), a pad row holds 144 pads in the bending plane. This results in 1.15 million channels on 674.67 m^2 active area for the PHOS-hole layout. Charge signals induced on the pads are passed via plated-through vias to the back side of the pad plane. Flexible flat cables are soldered to this back side and transmit the analog signals to the readout electronics. The radiator and the back panel provide

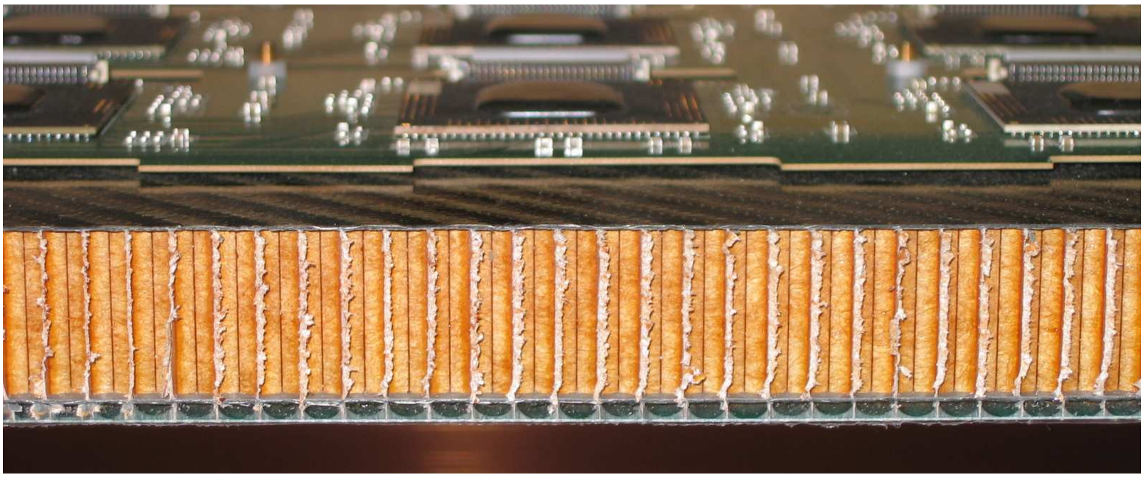

Figure 2.4: Photo of the back panel composite structure cross section. Well visible in the bottom part are the glue joints between the pad plane and the 2 mm thick honeycomb spacer.

enough mechanical rigidity to the chamber to ensure a deformation of less than 1 mm at an overpressure of 1 mbar. The readout electronics is installed directly on the back panel, see Figure 2.4. With water cooling meanders installed on top of the electronics the thickness of a detector module is 125 mm.

2.2.2 Principle of operation

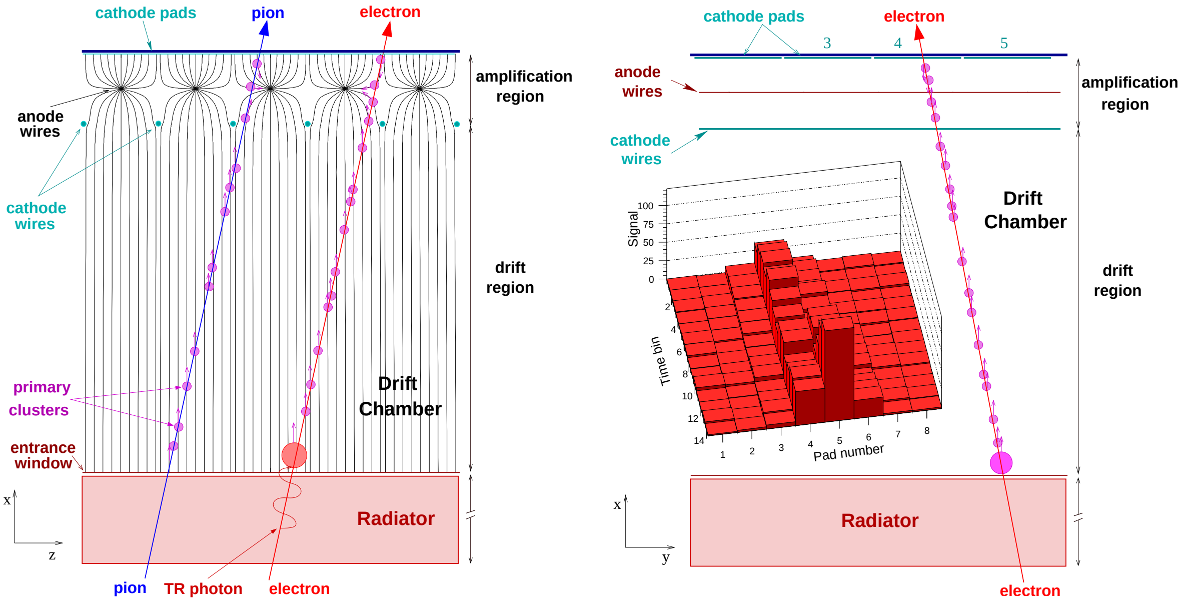

Figure 2.5: A schematic illustration of the TRD principle, from [25].

Charged particles passing the TRD detector liberate electrons in the counting gas (Xe/CO_2 (85%/15%)) through ionisation along their tracks as shown in Figure 2.5.

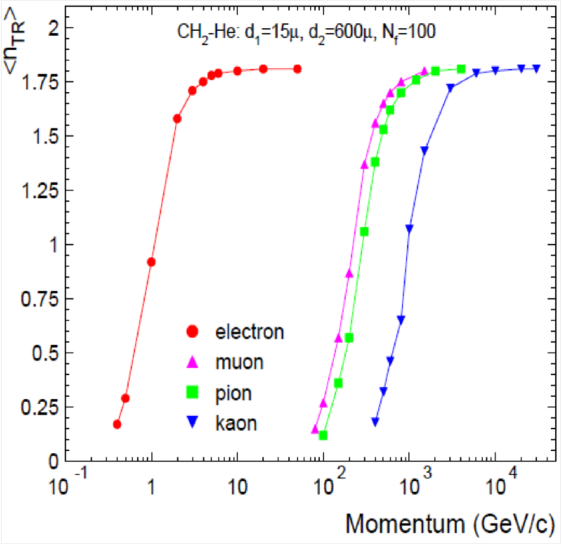

Figure 2.6: Momentum dependence of transition radiation production for different particle types. In the energy range of up to 100 GeV electrons are the only particles producing TR, from [25].

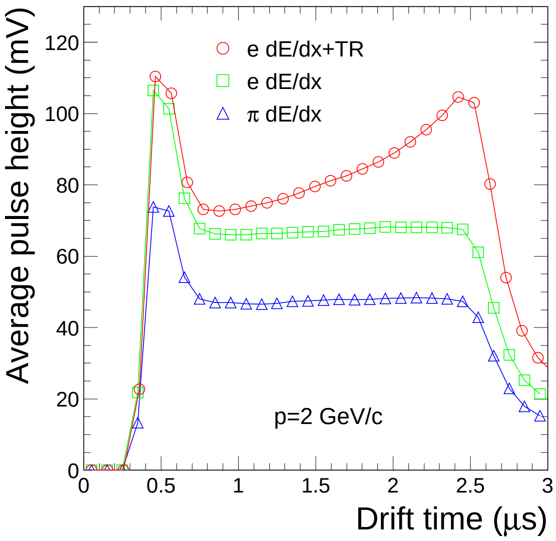

Figure 2.7: Average pulse height as a function of drift time for electrons with a TR (circles), electrons without TR (squares) and pions (triangles), for 2 GeV/c momentum in the ALICE TRD, from [25].

Transition radiation can be produced by highly relativistic particles (above a threshold of $\gamma \approx 1000$) crossing a refractive index interface in the radiator. Electrons exceeding this threshold (above 0.5 GeV/c) will produce X-ray photons in the energy range of a few keV. Due to their higher rest-mass, pions with a few GeV/c momentum are too slow to produce TR, compare Figure 2.6. The X-ray photons propagating at small angle to the initial particle track are absorbed on short length scale in the high-Z counting gas (Xe), where they deposit their energy with highest probability at the beginning of the drift region. All electrons from ionisation energy loss and X-ray conversions will then move with constant velocity along the homogenous drift field towards the amplification region. Upon gas amplification close to the anode wires an electrical signal is induced on the readout pads. The inset of the right panel in Figure 2.5 shows a typical electron track signal shared between 3 pads. Assuming the tracks originate from the interaction vertex, the inclination in ϕ-direction is a direct measure of their transverse momentum.

Figure 2.7 shows the average pulse height versus time for particles with a momentum of 2 GeV/c. It starts with a peak at the beginning of the drift time, quickly falling off to settle in a plateau and finally dropping in a tail (see green and blue curve). The peak is due to the initial particle track, ionising electrons on both sides of the anode wire grid. When the electrons from the drift area reach the amplification region, the signal drops to the plateau level. The pulse height drops off after 2 μs when clusters from the end of the drift volume have reached the anodes. Electrons can be discriminated from pions due to two effects : The electrons have an increased specific energy loss compared to pions at momenta of a few GeV/c, resulting in a higher plateau. Electrons passing through the TRD radiator with momenta above 2 GeV/c produce on average 1.45 TR photons of which 1.25 are detected, see [50]. These are absorbed at the entrance to the drift volume and contribute an extra peak dominating at the end of the drift time. A likelihood method or a trained neural network can be utilised to return a probability for the track to be an electron or a different kind of particle.

2.3 Readout electronics

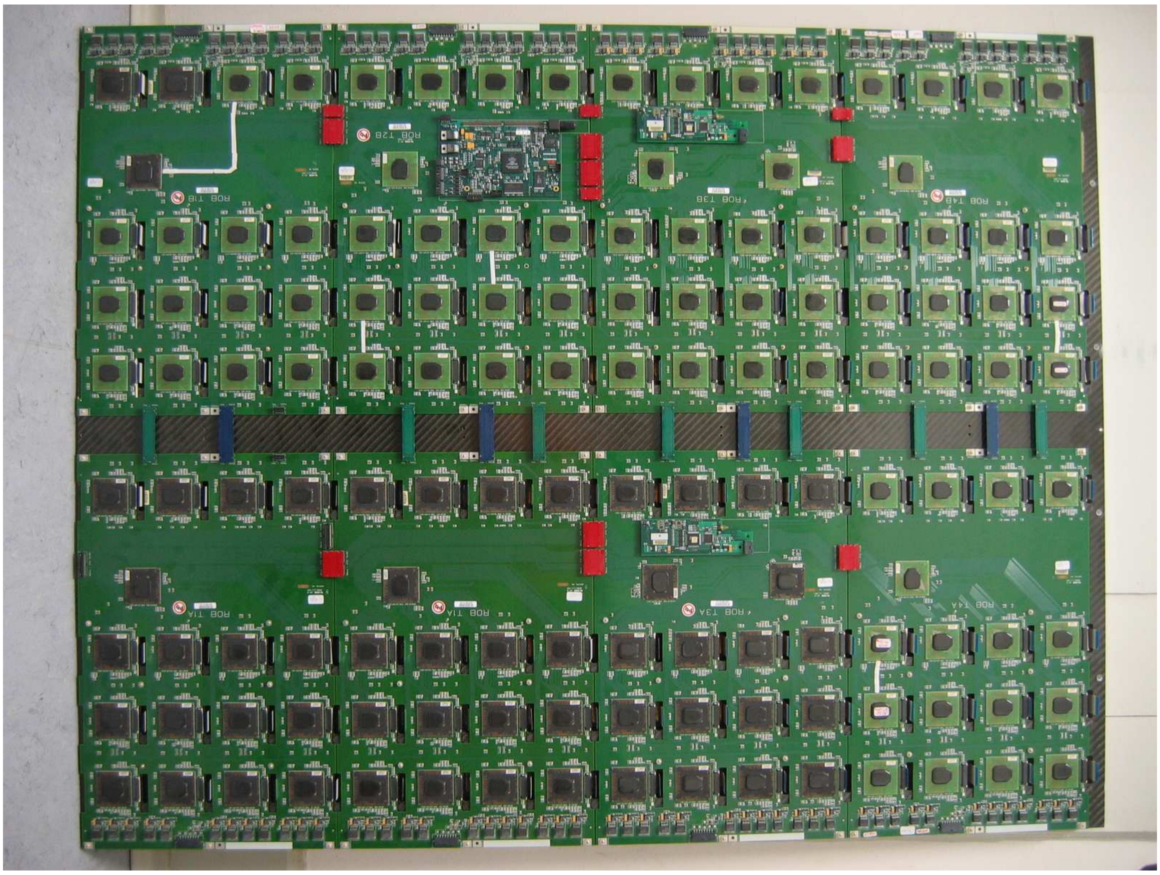

Figure 2.8: Back panel composite structure of a L1C1 chamber equipped with 8 readout boards, a DCS board, two ORIs and board-to-board interconnections.

2.3.1 General layout

An overview of the TRD electronics readout chain is shown in Figure 2.9. Each detector module can be operated independently of the others. It is is equipped with 6 or 8 readout boards, including two Optical Readout Interfaces (ORI) and a DCS board, mounted directly on the back-panel, see Figure 2.8. The data of a super module is transmitted to the Global Tracking Unit (GTU) through 60 optical fibres. The GTU can further analyze the data to derive a fast Level-1 trigger decision or forward the data to the DAQ via the Detector Data Links (DDL), 18 DDLs for the full TRD. In trigger mode, tracklets from all layers of a stack can be combined to detect high-momentum e^+e^--pairs or to determine the multiplicity of high-p_t particles.

2.3.2 Detector electronics

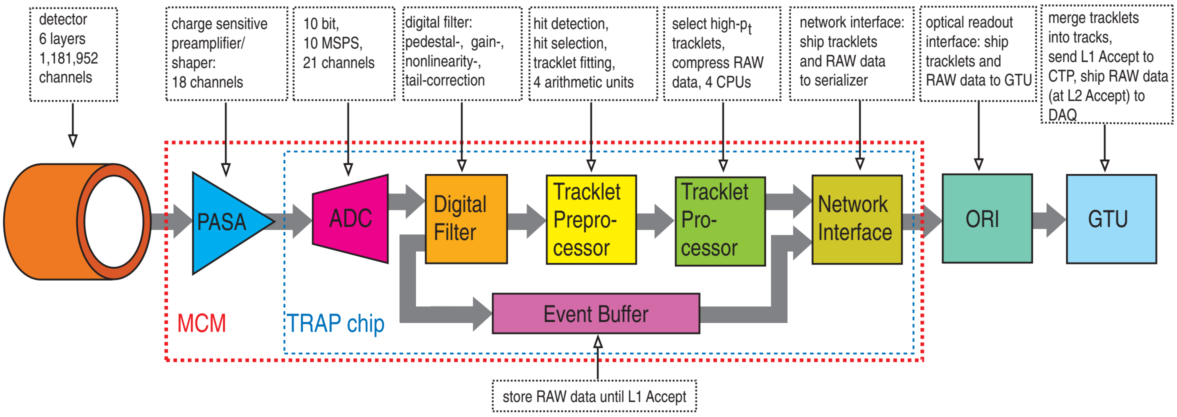

Figure 2.9: Schematic overview of the TRD electronics readout chain.

Two ASICs were designed for the on-detector data processing. The 18-channel preamplifier shaper (PASA) and the Tracklet Processor (TRAP) were integrated into a multi-chip module (MCM).

The PASA is a folded cascode with differential output (120 ns shaping time, 850e ENC for an input capacitance of 25 pF, 12.4 mV/fC gain, and 12 mW/channel power consumption). It was realized using the AMS 0.35 μm CMOS process. Each PASA chip has 18 input channels and 21 differential output channels. The three extra output channels are fed into the analogue inputs of the TRAPs on neighbouring MCMs. This allows for continuous tracklet reconstruction, also across MCM boundaries.

The Tracklet Processor is a mixed signal design realized in the UMC 0.18 μm process. It comprises 21 ADCs, event buffers and a group of digital filters for: the correction of non-linearity, pedestals and gain, further tail cancellation and crosstalk suppression. The gain correction filter can scale the input data chanel-by-channel within a range of ± 12% to compensate for gain variations inside a readout chamber. The tail cancellation filter compensates for the ion tails in the gas volume of the chamber, which improves the tracklet quality. Each TRAP holds four MIMD processing units calculating the tracklet inclination in bending direction, which allows to identify high-p_{t} particles at the trigger level. The total charge deposited along a track can also be computed in the TRAP, allowing to tag electron candidates at the trigger level.

2.3.3 Global Tracking Unit (GTU)

The pre-processed tracklets are sent stack wise from each detector module to the GTU, where they need to be matched in three dimensions for the reconstruction of transverse momentum. The global tracking based on the data of 1.15 million analogue channels has to be performed within 6.5 μs after collision to derive the Level-1 trigger decision in time. The trigger timing sequence involving the on-detector MCMs and the GTU is presented in Figure 2.10.

The core element of the GTU is the Xilinx Virtex-4 FX FPGA, which includes an integrated multi-gigabit serializer/deserializer and PowerPC processor blocks. More

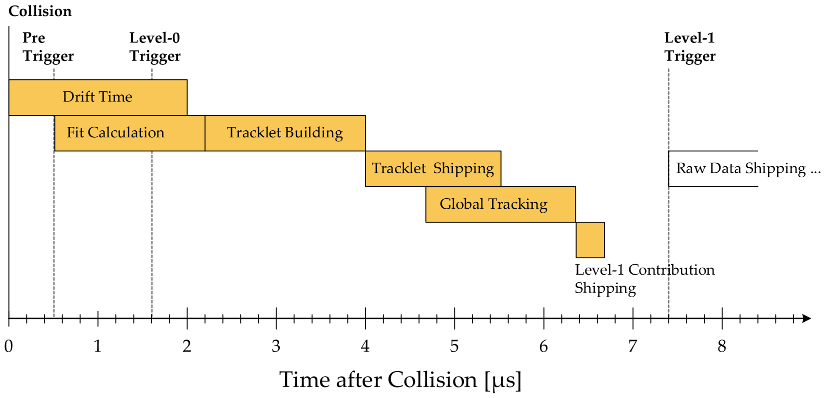

Figure 2.10: Trigger timing diagram for the generation of a high-p_t trigger.

than 100 of these FPGAs provide the processing power capable of handling up to 20000 track segments within 2 μs. The Track Matching Unit (TMU) is a CompactPCI board equipped with 12 fibre-optical SFP transceiver interfaces gathering the data from the 6 chambers of a stack. It performs the global tracking for a stack of six chambers as illustrated in Figure 2.11. The tracklets of all layers are projected onto a virtual middle plane. A cluster search algorithm finds matching tracklets in that plane, these are then fitted with a common track passing through all six layers of the detector. The output of five TMUs, interfacing a full super module, is forwarded through a custom bus to the Super Module Unit (SMU). The SMU is equipped with a DDL to the DAQ system and a DCS board for configuration and control of the TMUs. GTU trigger decisions are collected by a single, central Trigger Unit (TGU) serving as interface to the ALICE Central Trigger Processor (CTP). The CTP controls and processes all trigger signals within ALICE. It is designed to select events displaying a variety of different features, making optimum use of the detector systems.

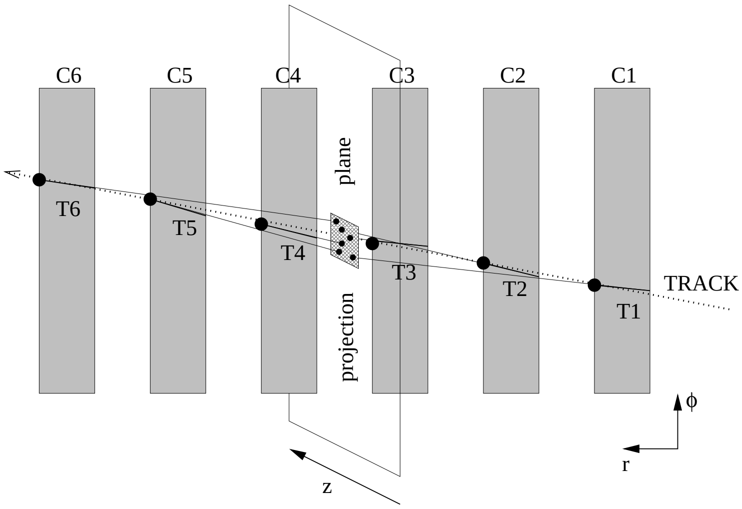

Figure 2.11: Global tracking concept as performed in the TMU

2.3.4 Pre-trigger system

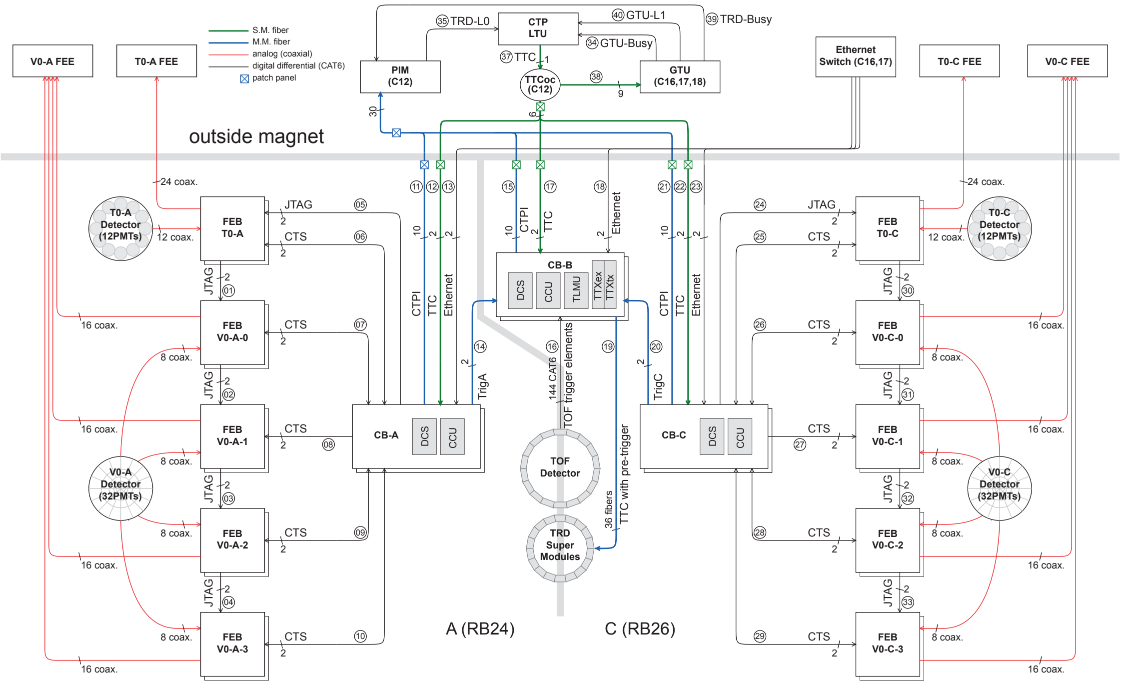

Figure 2.12: Schematic overview of the pre-trigger system.

The pre-trigger system (Figure 2.12) provides fast wake-up signal to the TRD. It allows to keep the digital part of the readout electronics in a low power mode while there are no events to process. The Control-Box-B (CB-B) derives the pre-trigger signal from a combination of analogue inputs from the V0, T0 and TOF detectors. From there it is forwarded via the TTC fibers to the detectors in the super modules, where it is available at the readout electronics within 700 ns after collision. The L0 signal issued by the Central Trigger Processor (CTP), would deteriorate the TRD signals, as it would arrive after 1500 ns at the Front End Electronics. Thanks to the pre-trigger system it is possible to generate a TRD L1 trigger within the required 6,5 μs.

2.3.5 Detector Control System (DCS)

Each detector module can be addressed from outside through its DCS board, which is powered independently from the readout electronics. The DCS board is responsible for the entire control, configuration and monitoring of the detector electronics. It comprises an Altera FPGA with ARM9 core, flash memory, Ethernet-, JTAG-, and I^2C-interfaces, 8 analogue and 8 digital inputs as well as 8 digital outputs.

The DCS board is able to turn on or to shutdown the voltage regulators of the readout boards through its external control lines. It can address each MCM through a Slow Control Serial Network (SCSN), which can be rerouted to bypass faulty MCMs without loss of data from entire readout boards. The configuration of the MCMs including channel masks, filter and gain parameters as well as zero suppression conditions used for the reconstruction of the tracklets are handled by the DCS board. It also receives and locks to the central clock signal, which is then synchronised with the MCMs. The trigger signals are propagated in the same way. Finally the DCS board also monitors the temperatures of all individual MCMs.

The states of all services (low voltage, high voltage, gas, cooling) as well as all states generated or monitored by the DCS board are implemented as Finite-State Machines (FSM) which are operated and controlled via PVSS.

Chapter 3

The readout pad plane of the TRD

The particle detection properties of the TRD crucially depend on details in the design of it's readout pad plane. This chapter begins with an overview on the design parameters of the TRD pad plane. It explains, how the layout was generated for production by the PCB manufacturer. It provides a short introduction to preparation and handling of the pad planes during detector construction. Finally, the physical properties of the pad plane are highlighted, taking a close look at pad plane related noise patterns.

3.1 Part I - Design and production

3.1.1 Detector requirements

The Transition Radiation Detector is composed of 12 individual chamber types. These differ in size (length and width) and number of readout channels, related to their position in the TRD super module. The best possible position resolution of a track is achieved when the induced charge distribution is shared between typically two or three neighbouring pads. The pad granularity in azimuthal direction has therefore been matched to the induced charge distribution. The pad size along z-direction determines the total number of channels in the TRD and is constrained on the one hand by the budget available for readout electronics and on the other hand by the maximum tolerated detector occupancy. At the highest simulated multiplicity density of $\mathrm{d}N_{\mathrm{ch}}/\mathrm{d}\eta = 8000$ the maximum occupancy in the TRD will be 34%, including secondary particles. The TRD must have a small radiation length, thus the pad plane needs to be thin, but still stiff enough to ensure flatness at a 0.1 mm scale. To reduce complexity and cost during readout board production, we decided to use a unique signal cable spacing pattern, which interconnects the pad plane to the front-end electronics.

The PCB production sets some further constrains on the layout of the pad planes: The available PCB base material is of smaller dimensions than the typical size of a TRD chamber. In addition the PCB manufacturer is limited to a maximum PCB that can be handled in the production line. These conditions require to produce for each chamber type an individual set of pad planes, composed of 2 or 3 pieces. All pad planes must respect a common set of global design parameters.

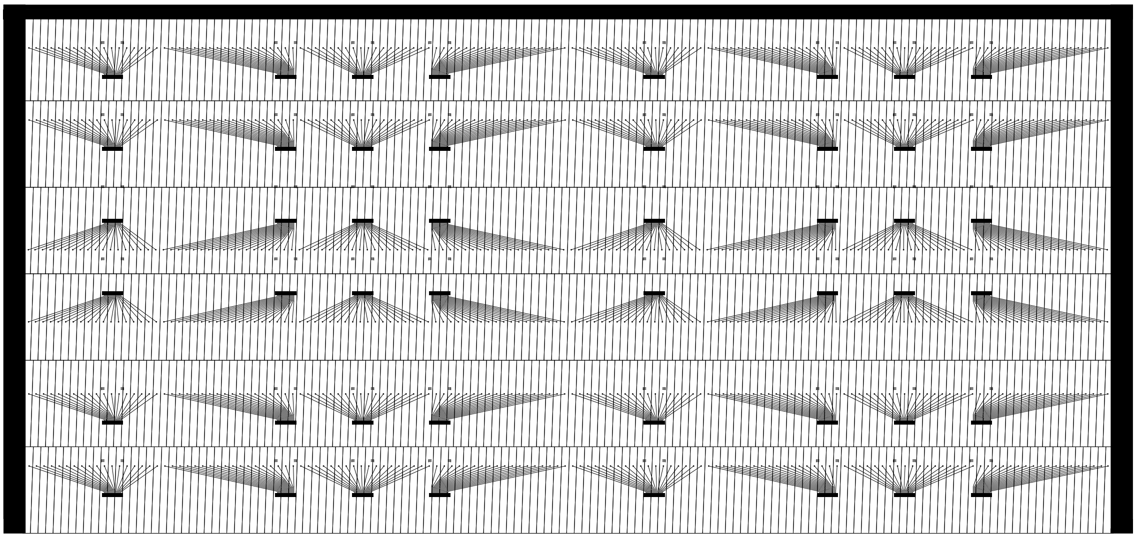

Figure 3.1: L5C1 type 3 pad plane. Top part of pad plane with 6 rows.

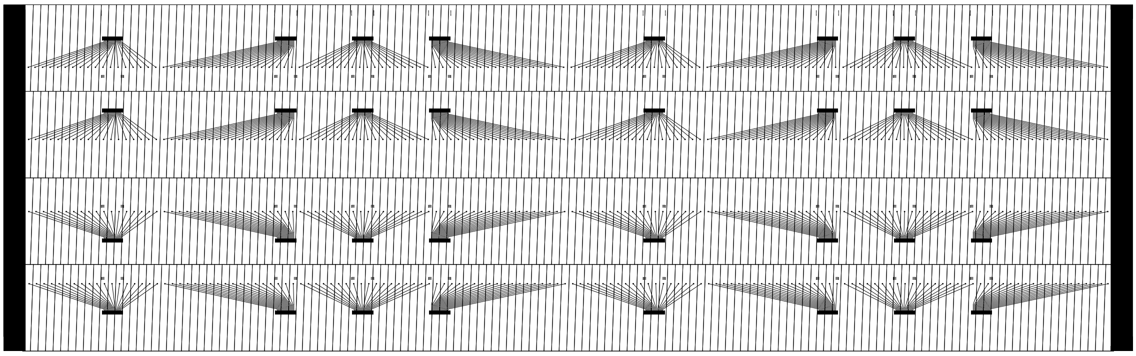

Figure 3.2: L5C1 type 2 pad plane. Central part of pad plane with 4 rows.

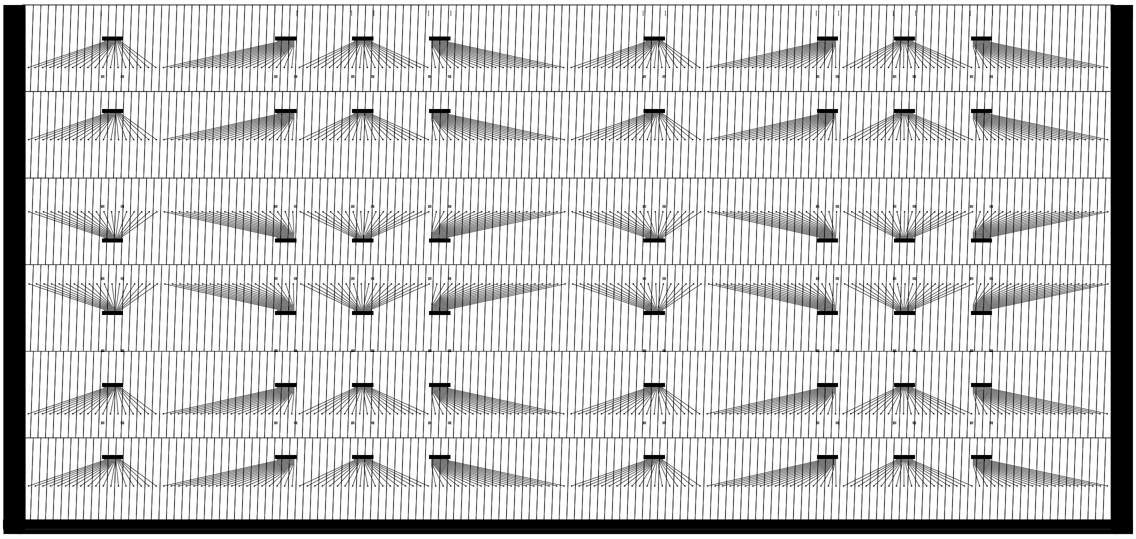

Figure 3.3: L5C1 type 1 pad plane. Bottom part of pad plane with 6 rows. Each rows has 144 pads, grouped in 8 × 18 pads.

3.1.2 The pad plane geometry

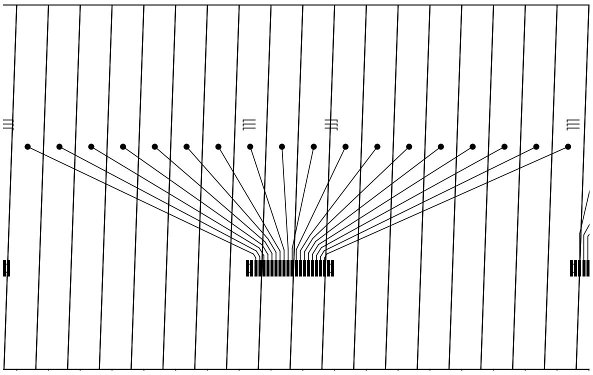

Figure 3.4: Zoom on a group of 18 pads. The pads are connected with thin traces to a common footprint to which a flat signal cable is soldered. This cable connects to the PreAmplifier-ShAper (PASA) chip with 18 input channels. The tiny "LLL"-shaped markers are used to align the flat cables prior to soldering.

The readout pad plane of the TRD is located at the end of the amplification region, opposite to the radiator. The number of pad rows in a chamber is an integer multiple of 4, either 12 rows for C0 type or 16 rows for C1 type chambers. There are 144 pads in a row, subdivided into 8 groups of 18 pads (Figure 3.3). Each group of 18 pads is mapped with thin traces to a common footprint on the pad plane PCB (Figure 3.4). A flat signal cable is soldered to that footprint and interconnects to the front-end electronics. The soldering footprints are placed across the pad plane in a 4 × 4 pattern, which maps the readout board geometry. This common interface design allows to use the same type of readout board on each type of chamber (Figure 2.8). A readout board covers the area of 4 half pad rows (4 × 72 pads). The full TRD has a total of 1181952 readout pads, with holes in 3 sectors in front of the PHOS detector the TRD counts 1150848 pads.

The active area of the full TRD amounts to 694.07 m^2, which is equivalent to the surface of more than 2.5 tennis courts. The base material of the TRD pad plane is a 0.36 mm thick, halogen free FR-4 laminate coated on both sides with 17 μm of Cu. The maximum allowed width of PCBs in the production facility is 610 mm, while the base material has sheet sizes of 1225 mm × 1070 mm. The PCBs are etched with the desired pad shape on the front side and wire traces with soldering footprints on the back side. Since the TRD chamber dimensions are far larger than the maximum available PCB size, the pad plane of each chamber is composed of individual PCB pieces. Hence C0 type chambers (12 rows) are composed of 2 pieces of pad plane with 6 rows each. The C1 type chambers (16 rows) are made up of 3 pieces of pad plane with 6+4+6 rows (see Figures 3.1 to 3.3). The fabricated pad plane PCBs sizes range from the smallest 996 mm × 300 mm (L0C1 type 2) to the largest 1174 mm × 550 mm (L5C1 type 1). To cover the 12 chamber types of the TRD, 30 different types of pad plane pieces are needed. An overview of all pad plane dimensions is given in Table 3.1. The pad planes of all 12 different TRD chamber types are presented in Appendix B.

Not only does the pad plane allow to measure the induced charge, it also serves a gas seal towards the rear of the detector. The pad planes are fabricated as plated

type	L_z	$W_{r\phi}$	#rows	α_{tilt}	L_{rim}	W_{rim}	L_{opad}	L_{ipad}	W_{opad}	W_{ipad}
L0C0	1080	922	12	-2	10	5	80.0	90.0	5.15	6.35
L0C1	1220	922	16	-2	10	5	75.0	75.0	5.15	6.35
L1C0	1080	966	12	+2	10	5	80.0	90.0	5.85	6.65
L1C1	1220	966	16	+2	10	5	75.0	75.0	5.85	6.65
L2C0	1080	1011	12	-2	10	5	80.0	90.0	7.05	6.95
L2C1	1290	1011	16	-2	10	5	75.0	80.0	7.05	6.95
L3C0	1080	1055	12	+2	10	5	80.0	90.0	7.75	7.25
L3C1	1360	1055	16	+2	10	5	75.0	85.0	7.75	7.25
L4C0	1080	1099	12	-2	10	5	80.0	90.0	8.45	7.55
L4C1	1430	1099	16	-2	10	5	75.0	90.0	8.45	7.55
L5C0	1080	1144	12	+2	10	5	80.0	90.0	9.65	7.85
L5C1	1450	1144	16	+2	10	5	85.0	90.0	9.65	7.85

Table 3.1: Dimensions of the individual TRD chambers, all sizes in mm. type: chamber type. L_z: pad plane length in z. $W_{r\phi}$: pad plane width in $r\phi$. #rows: number of pad rows in chamber. α_{tilt}: tilt angle in degrees as seen by a particle originating from the interaction point. L_{rim}: size of rim in z. W_{rim}: size of rim in $r\phi$. L_{opad}: length of outer pads in z. L_{ipad}: length of inner pads in z. W_{opad}: width of outer pads in z. W_{ipad}: width of inner pads in z. The total pad surface of the TRD (18 SM) amounts to 694.07 m^2.

through PCBs, each single pad has a tiny hole, electrically interconnecting the pad layer with the layer of the soldering footprints. These 1728 or 2304 holes per chamber cannot be sealed reliably during the fabrication process of the PCB. As the pad plane of a chamber is composed of two or three individual pieces, there are in addition one or two sub-millimeter wide gaps across the chamber back panel. In order to ensure gas tightness, all these openings need to be carefully sealed with glue. This is done in when glueing the pad plane to the back panel of the chamber.

3.1.3 Readout pads

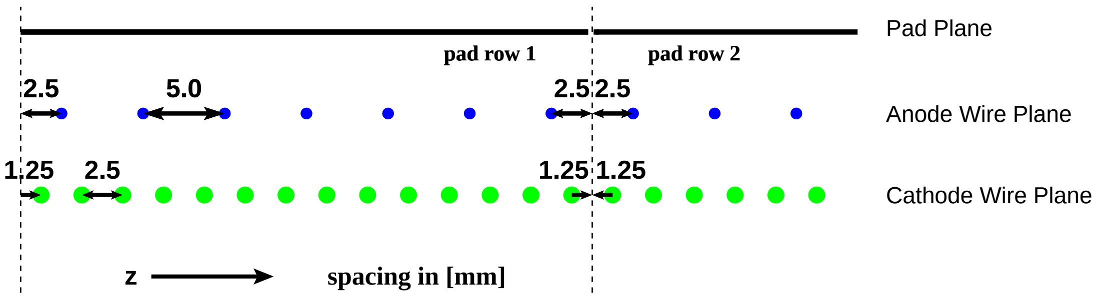

Figure 3.5: Arrangement of pad with respect to the anode wire grid position (blue) : The pad length is an integer multiple of the anode wire pitch. The pad row borders are always centered between two anode wires. Hence the charge charing between two adjacent pad rows is minimised.

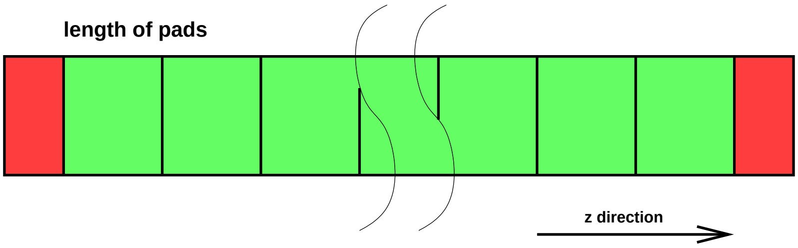

Figure 3.6: The two outer rows (number 0 and 11 or 15) at the beginning and end of the pad plane usually have pads with different length compared to rows in the inner part of the pad plane.

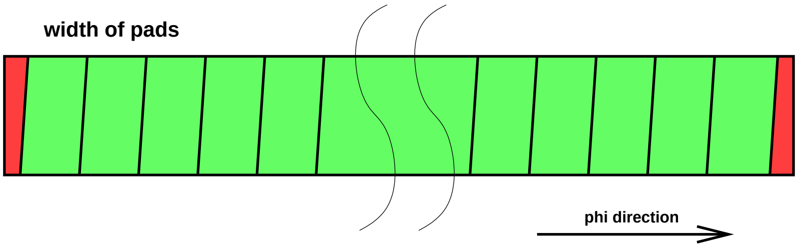

Figure 3.7: In a row of pads, the two outer pads (0,143) at the beginning and end, are usually different in width from those pads inside the row.

In order to reduce charge sharing between adjacent pad rows, the pad length was chosen to be an integer multiple of the anode wire spacing (5 mm), see Figure 3.5. As a consequence for every chamber type, the outer pad rows (the first and the last) may have pads of a different length than the inner pad rows, as detailed in Figure 3.6.

The pad width for the inner 142 pads of a row was defined to be :

$$\mathrm{pad}_{width}(\mathrm{layernumber}) = \mathrm{layernumber} \times 0.3\ mm + 6.35\ mm \tag{3.1}$$

The two outer pads of each row fill up the gap to the rim of the distance ledges, as illustrated in Figure 3.7. Therefore the width of these outer pads is usually different from the one of the inner pads.

The gap between two adjacent pads or rows is $250\mu m$, this is large enough to ensure electrically well separated pads after the etching process, without exposing significant insulating surface.

3.1.4 Pad response function

The relative pulse height distribution on adjacent pads, induced by a point like avalanche on the anode wire, is called the pad response function (PRF). The PRF can be obtained by integration of the induced charge distribution across the pad area, with y denoting the coordinate given by the anode wire direction :

$$\mathrm{PRF}(y) = \int_{y-W/2}^{y+W/2} \rho(y)\mathrm{d}y \tag{3.2}$$

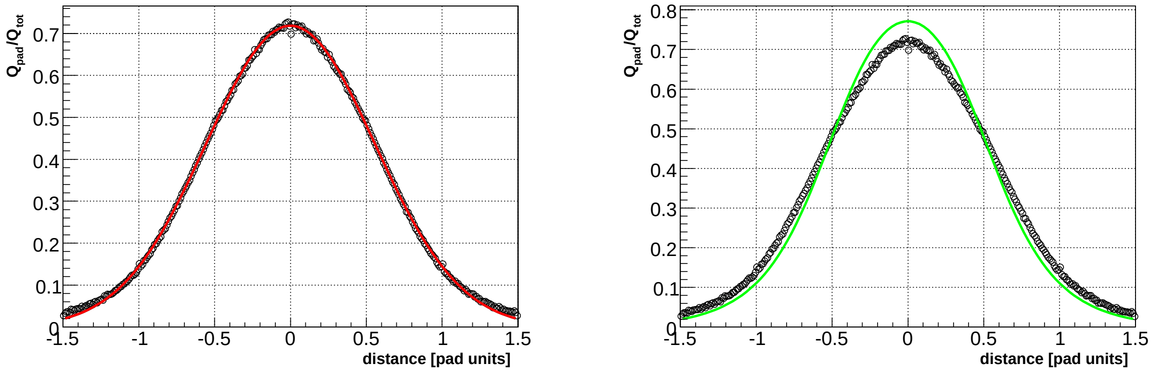

Figure 3.8: Pad response function measured with cosmics data for layer 4 of super module VI, from [30]. The left panel is fitted with a Gaus distribution. The right panel is fitted with the Mathieson formula.

Mathieson has found an empirical formula describing the cathode charge distribution in symmetrical multi-wire proportional chambers, see [31]. It is based on the design parameters of the detector, namely the anode–cathode separation, the anode wire pitch and the anode wire diameter. The amplification region of the TRD, however, is not exactly symmetric. The ground potential of the cathode plane is slightly shifted into the drift volume, due to the transparency of the cathode grid. Still, the Mathieson formula gives a good approximation of the induced charge distribution. Figure 3.8 displays the pad response function measured for a layer of a TRD super module, fitted with a Gauss distribution and with the Mathieson function. The measured PRF is perfectly approximated by the Gaussian. As already observed in TRD prototype chambers, see [48] and [22], the standard deviation of the Mathieson fit is slightly narrower than the Gaussian, the fit also overshoots the maximum of the PRF. The discrepancy between the measured PRF and the Mathieson formula could be explained due to cross-talk between adjacent pads, which is introduced by capacitive coupling between the pads.

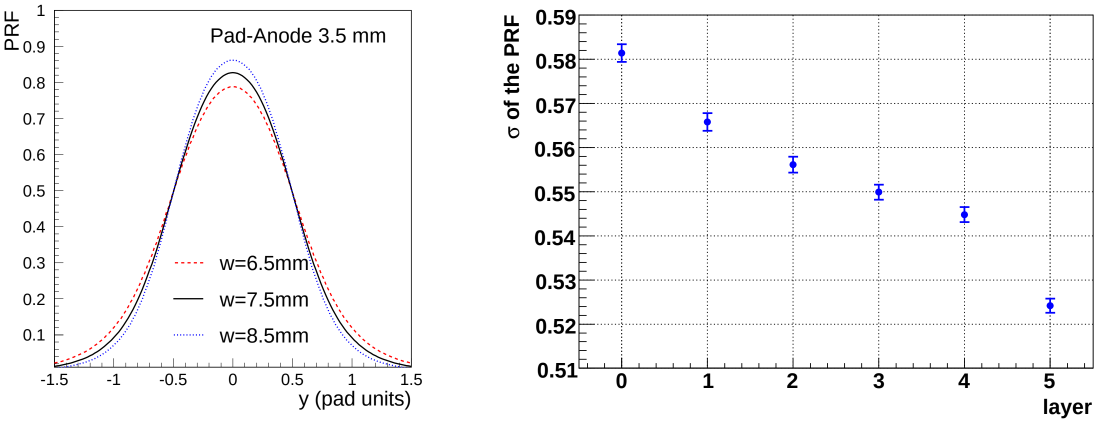

Figure 3.9: Pad response functions calculated for 3 different pad widths (left). A linear decrease of the PRF standard deviation is observed in the 6 layers of a SM (right).

Under otherwise fixed chamber parameters, the width of the pad response function is correlated with the width of the pads. An increase in pad width induces a decrease of the standard deviation of the PRF, as depicted for three different pad sizes in Figure 3.9. Also shown is the linear relation between the standard deviation of the PRF and the layers number in the super module. This is directly related to the linear increase of pad with across layers as defined in equation 3.1.

3.1.5 Improvement of z-resolution

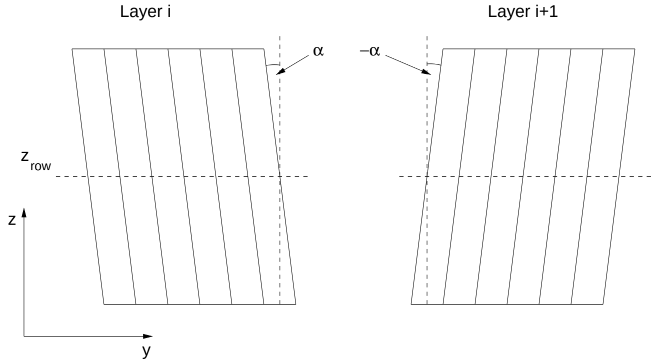

layer	tilt orientation
5	counter-clockwise
4	clockwise
3	counter-clockwise
2	clockwise
1	counter-clockwise
0	clockwise

Figure 3.10: Tilted pad geometry in two successive layers (left). Tilt orientation of the pads in the TRD, as seen by a particle originating from the vertex (right).

In order to improve the position resolution along the long axis of the pad, the pads are slightly tilted by an angle of 2 degrees with respect to the z-axis, see Figure 3.10. In consecutive layers this tilt is performed in opposite direction. A particle originating from the vertex and passing through the TRD sees the pads in the 6 layers tilted in the order indicated in the table.

Let's assume the following definitions : $< y_{pad} >$ is the center of gravity in pad space, z_{row} is the z-coordinate of the center of a pad row, α_i is the tilt angle of layer i with respect to the z-axis, as reference see Figure 3.10. With tilted pads, the coordinates (ϕ_i, z_i) of a hit in a given layer are related to $< y_{pad} >$ and the tilt angle α_i :

$$\phi_i = \phi(< y_{pad} >) + (z_i - z_{row}) sin(\alpha_i) \tag{3.3}$$

The ϕ- and z-resolution have been computed as function of the pad tilt angle. Figure 3.11 shows the position resolution in $r\phi$- and z-direction as function of the tilt angle α. For simplicity only two layers are considered with straight tracks orthogonal to the pad planes ($\theta = 0$). Then the resolutions scale as follows with α :

$$r\Delta\phi \propto 1/cos(\alpha) \tag{3.4}$$

$$\Delta z \propto 1/sin(\alpha) \tag{3.5}$$

Already at small tilt angles the z-resolution can be improved without noticeable loss in ϕ-resolution.

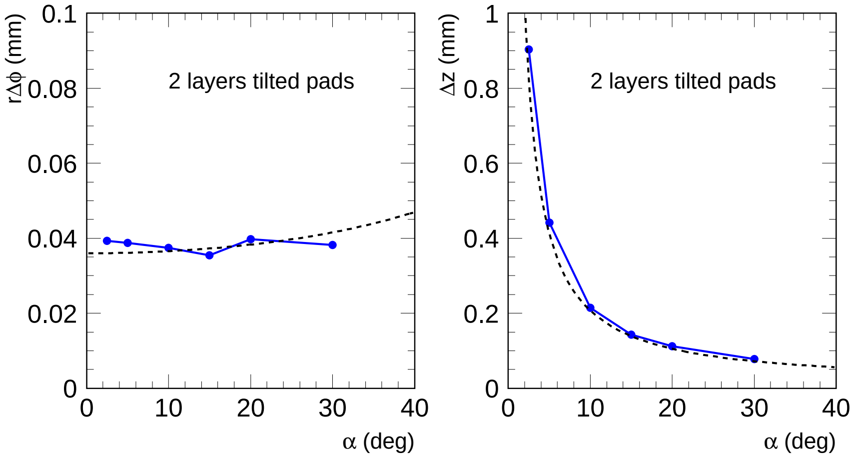

Figure 3.11: Resolution of track averaged ϕ- and z-positions as function of the pad tilt angle α. Two layers with tilt angle $\pm\alpha$ are assumed.

3.1.6 Design modifications

A first batch of pad planes for 60% of the TRD was produced in 2004. Pad planes from this first batch picked up a big amount of noise on the outermost pads of each row (pad numbers 0 and 143). This pickup was induced by the chamber internal high voltage distribution. The copper strips conducting high voltage for the anodes are located only 3.5 mm apart from the pads, respectively 7.0 mm for the cathodes, see Figure 3.12.

In 2006 the remaining 40% of TRD pad planes was ordered in a second batch. The pad design was slightly modified in order to reduce the noise pickup. As can be seen in Figure 3.13 each outer pad was thinned by 3 mm in width. This reduces the vertical overlap between the pads and the high voltage conductors.

The outer pads do not directly cover the drift volume of the detector. It is therefore

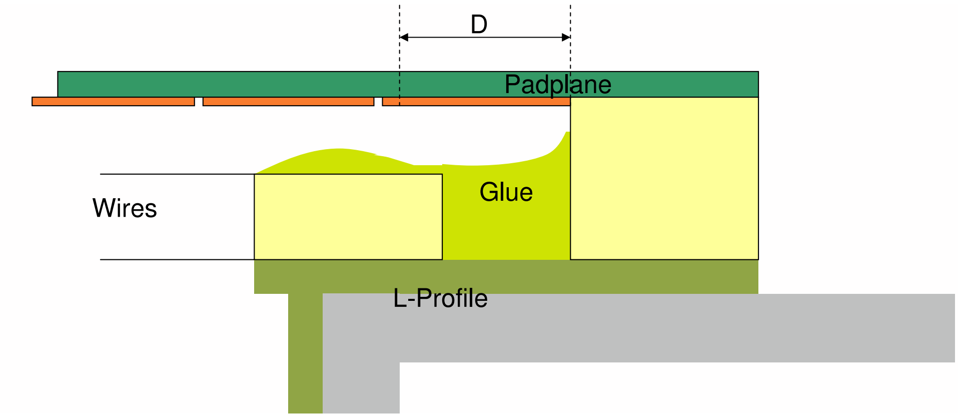

Figure 3.12: Inside the chamber the high voltage is distributed to the wire grids by copper strips. These influence the outermost pads of each row. The conductor for the anode high voltage runs along the top surface of the wire ledge, at a distance of 3.5 mm to the pad. The conductor for the cathode is located on the L-profile and buried with glue, 7.0 mm apart from the pad plane.

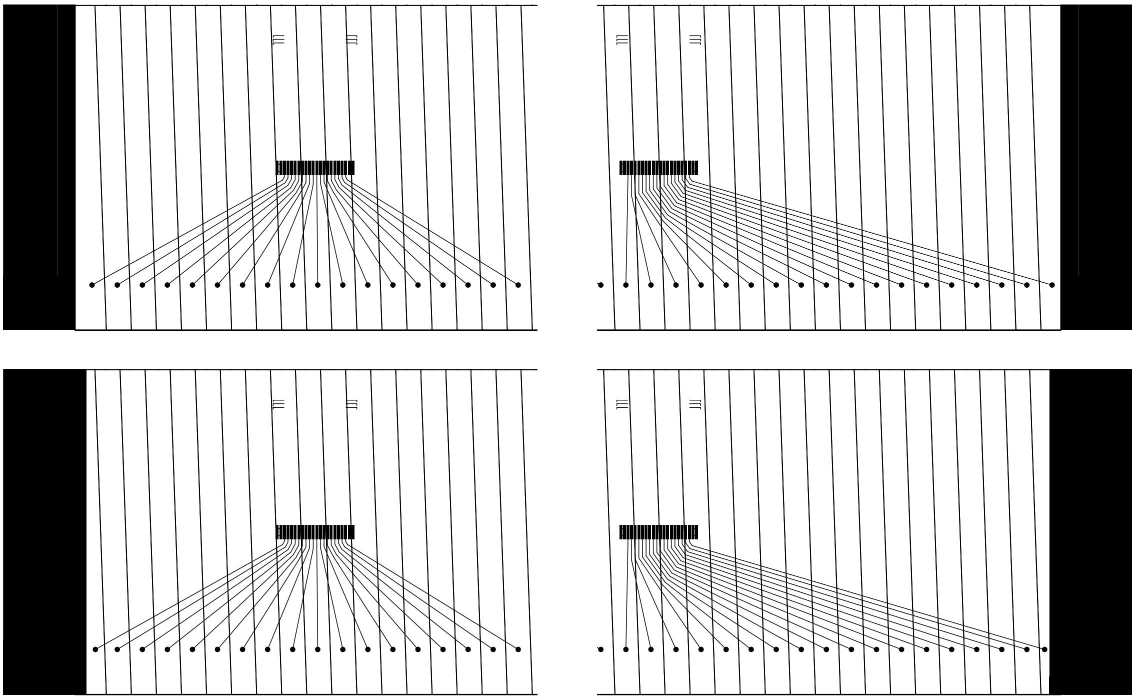

Figure 3.13: Zoom on a row of L2C0 pad plane, showing the modification of the outer pad width. Top panel: Pad plane layout of 2004 with wide outer pads. Bottom panel: Pad plane layout of 2006, where the outer pads are thinned by 3 mm each.

not clear whether the above design change will have any impact on the position resolution at the edge of the chambers. It may have happened that chambers were assembled with a combination of pad plane pieces from both batches, although it was not forseen to mix pad planes from the two batches.

3.1.7 Automated pad plane layout generation

For all 12 TRD chamber types a total of 24192 pads needs to be placed onto 30 pieces of pad plane, next slightly tilted and individually interconnected to 1344 soldering footprint locations. During the design phase of the TRD the chamber dimensions kept changing rather frequently. It was therefore not possible to manually draw the layout files of the pad planes, the design process had to be automated. The layout of the PCBs can be submitted to the manufacturer in Gerber data format [32], the specification of which is freely available. Based on this documentation a program was developed to automatically layout the pad plane PCBs. It reads the chamber geometry as input from a file, then generates the pad plane geometry (pads, vias, traces, soldering footprints, alignment marks etc.) for all PCB types and finally dumps the output in a set of 9 files for each of the different PCB types. Freely available Gerber viewer were used to crosscheck the automatically generated output. Once compiled this program allowed to generate the full TRD pad plane layout within a few seconds, allowing for easy implementation of design changes and fast optimisation cycles.

3.1.8 Soldering of flat cables

The signals induced on each pad of the pad plane need to be transferred to the front-end electronics located 25 mm away, on the backside of the chamber back panel. They are bundled in groups of 18 pads at the soldering footprints on the backside of the pad plane. It was chosen to use flat cables soldered directly to the pad plane PCB for this interconnection. On the front-end electronics side these cables are inserted into surface mounted connectors. The flat cables (65664 in total) have to be of low cost, low capacitance, cut to length at a 1 mm precision and solid enough to be bent upright just behind the soldering spot. The amount of heat applied during the soldering step needs to be limited as it must not permanently deform the thin pad plane PCB.

A specially designed soldering machine covering the entire surface of the PCBs was built for this task, see Figure 3.14. It uses an upside-down-Ω-shaped, electrically heated yoke (Figure 3.15), which is pneumatically pressed onto the soldering spot. The heat profile and applied pressure are programmable. A set of positioning tool-bars was provided to automatically adjust the soldering head position to the correct flat cable location for the 30 different pieces of pad plane.

3.1.9 Glueing of pad planes to the back panel

As a preparatory step prior to the final chamber assembly the pad plane PCBs need to be glued to the carbon fiber sandwich back panel. In order to ensure good gain uniformity the surface of the pad plane towards the amplification region needs to be flat to a 0.1 mm level. Therefore the pad plane pieces are aligned on a massive vacuum table serving as flat surface reference, see Figure 3.16. Once in place they are sucked onto the table surface by under-pressure. The vacuum table is specially designed to fit the 30 different types of pad plane pieces using a minimum number of 4800 vacuum holes. Up to three pieces of pad planes can be held in place for the glueing step of the back panel assembly. The vias in the pad planes must not lie on top of the vacuum holes in the table to avoid sucking glue through the vias into the table. Once the pad plane pieces are aligned, all (96/128) signal cables need to be placed and held in vertically upright position. A special tool was developed for this purpose, see Figure 3.16. Only once all cables stand in line, the glueing procedure can begin and one can easily feed them into the (96/128) cutouts of the back panel. Finally all signal cables stand out of the glued back panel without being blotted by glue as documented in Figure 3.17.

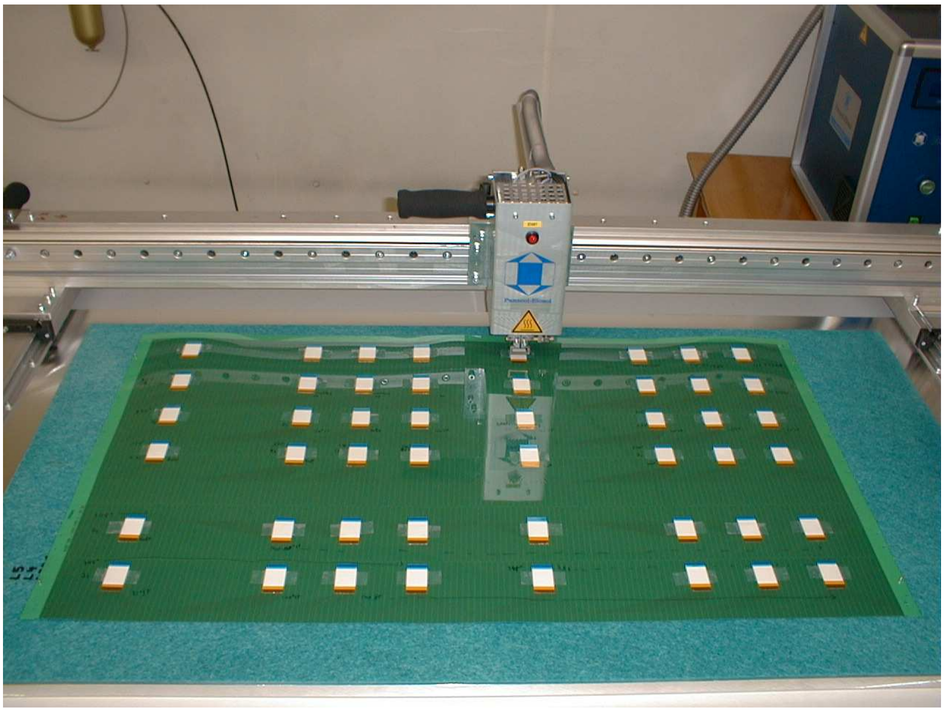

Figure 3.14: A piece of pad plane PCB is aligned in the pad plane soldering machine. Eight flat cables per row are positioned on the respective footprints. The soldering gun is located at he bottom of the cuboid box.

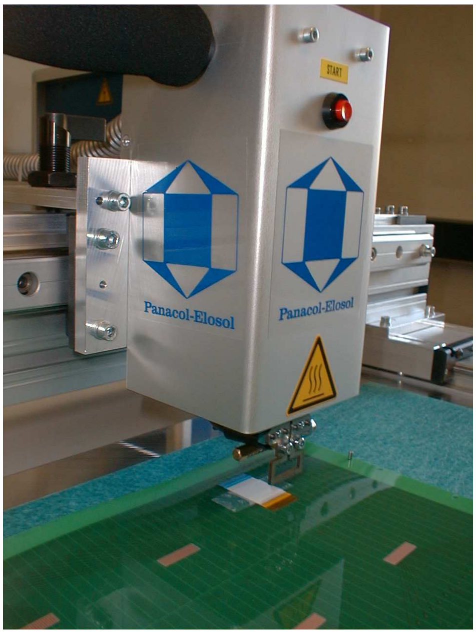

Figure 3.15: Zoom onto the soldering gun. The upside-down-Ω-shaped head is visible in position right on top of the yellow part of the flat cable.

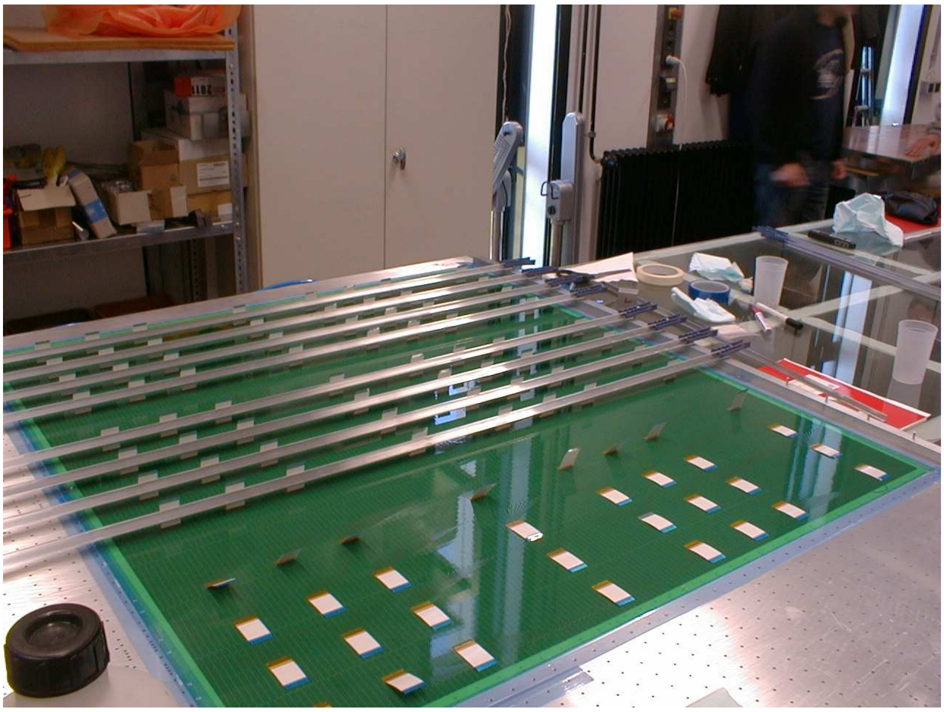

Figure 3.16: A pad plane is positioned on the vacuum table and being prepared for the gluing of the back panel. All the flat signal cables need to be put into vertically upright position to neatly fit through the holes in the back panel, prior to applying the glue.

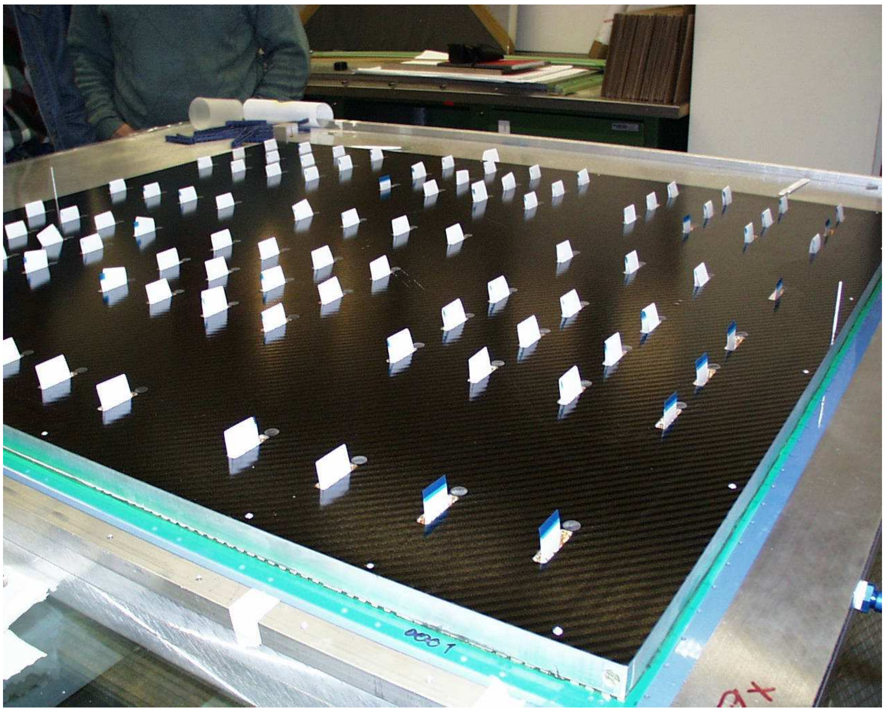

Figure 3.17: The back panel was lowered into the glue applied to the pad plane. All 96 flat signal cables were simultaneously holed-in without being smudged by the glue.

3.2 Part II - Physical properties of the pad plane

This section focuses on a correlation between the noise distribution observed in the readout electronics and the static pad capacitance distribution of the pad plane. It is quantitatively analysed which sources contribute to the noise. Finally, a way to normalise the noise distributions is presented.

3.2.1 Noise distribution in the TRD layers

During the integration phase and upon completion of a super module, noise data is taken to test the status of the readout electronics. The noise is measured by sampling a series of randomly triggered events and then looking for fluctuations of the baseline in each channel. In case of a problem with the detector, the noise distribution in the electronics can point to the source of the problem.

A noise measurement on a completed super module is displayed in the following six figures (3.18 to 3.23). Each figure represents a full TRD layer composed of 76 rows by 144 pads. Even a faultlessly assembled TRD super module displays characteristic noise patterns. The noise distribution in each layer exhibits stripes of increased noise along the z-direction, visible as green bands in the figures. The thick vertical black lines represent the boundaries between the 5 chambers of a layer. The thick horizontal black line delimits the two sides of a chamber covered with ROBs. While the dashed horizontal black lines show the borders between MCMs along a row.

The noise bands appear to follow the MCMs structure : In the lowest layers 0 and 1 (Figures 3.18 and 3.19) two noise bands are surfacing. Two additional bands appear in the layers 2 and 3 (Figures 3.20 and 3.21), but the bands do not yet entirely cover the 18 pads of the corresponding MCMs. While in layer 4 (Figure 3.22) the noise alternates from low to high level from one MCM to the next one, resulting in 4 bands of elevated noise. Layer 5 (Figure 3.23) shows extra noise around the borders, in ϕ-direction of stack 1 and 4, in addition to the noise bands. Due to this non-intrinsic noise, layer 5 will be discarded in the quantitative noise source analysis.

The observed noise bands correlate strongly with the distribution of the static pad capacitance along pad rows, as will be further investigated.

3.2.2 Static pad capacitance distribution

Independently from the measurement of electronic noise described above, the static pad capacitance to ground was measured on a representative set of six chambers. The chambers selected were all C0-type, one from each layer. These chambers from the central stack have identical pad length and differ only in the width of their pads. The pad capacitance was measured on the same row of each chamber, with all other (95) flat signal cables connected to ground. The traces on the pad plane PCB guiding the signals from the pads to the flat cable footprints are almost identical in shape for all rows of a layer. It can therefore be assumed that the shape of the pad capacitance distribution in a C0-type row is typical for all other rows in that same layer.

For each layer the pad capacitance distribution is shown as function of the pad number, compare Figures 3.24 to 3.29. In addition, each figure contains the projection

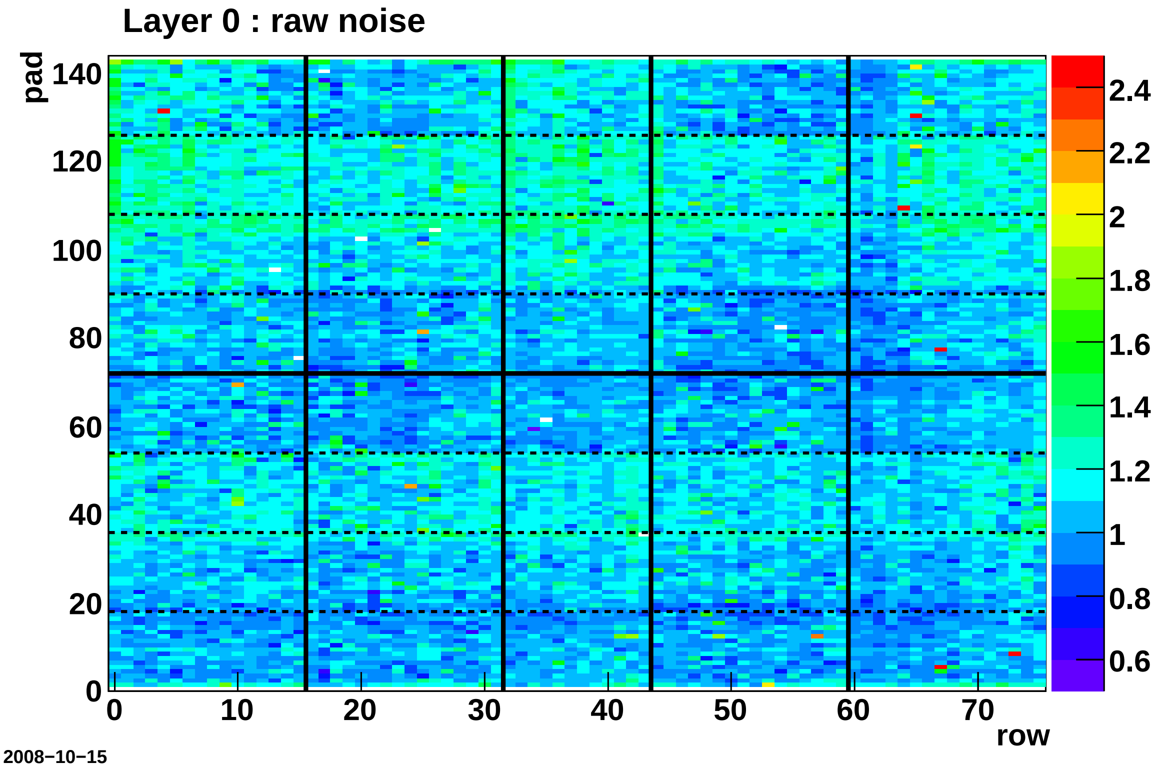

Figure 3.18: Raw noise distribution in layer 0, scale ADC channels.

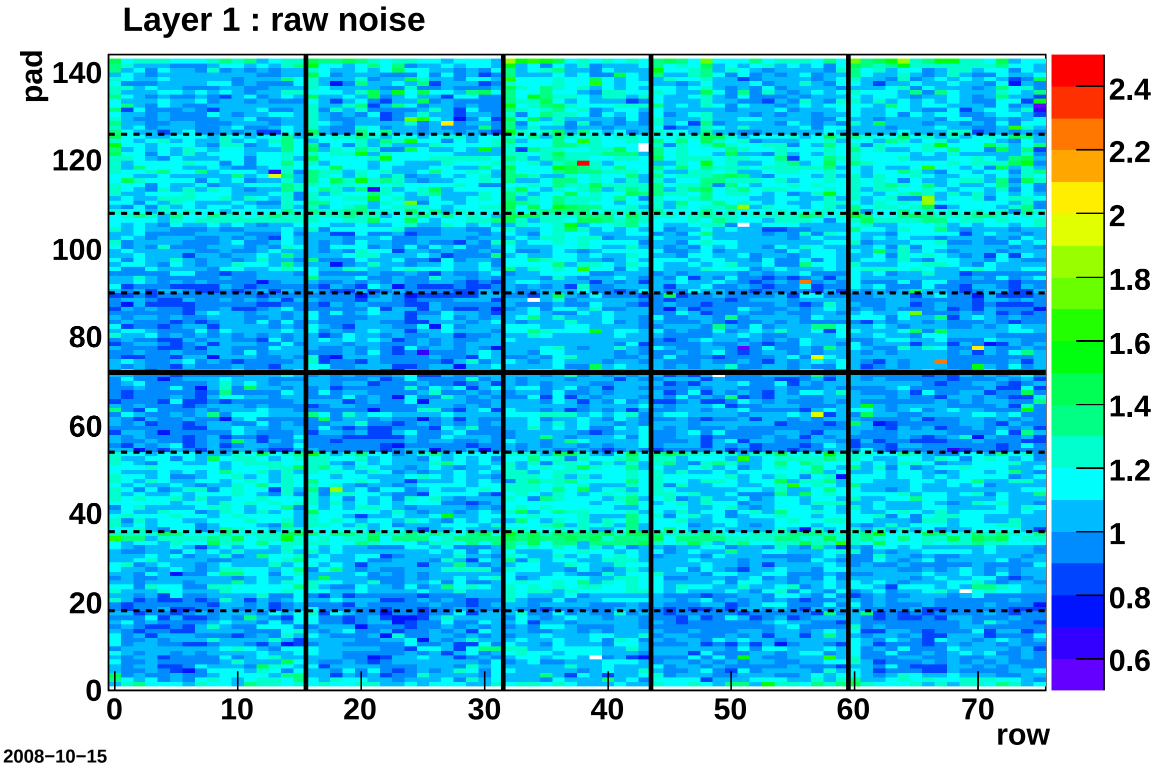

Figure 3.19: Raw noise distribution in layer 1, scale ADC channels.

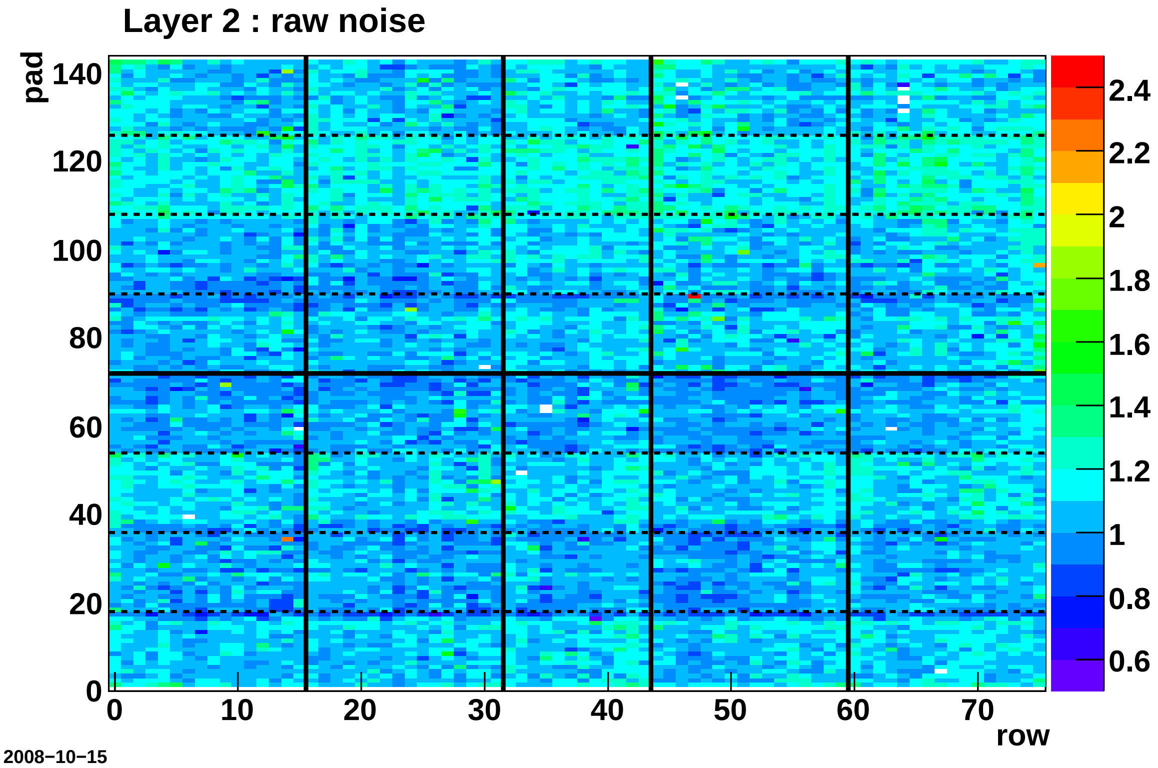

Figure 3.20: Raw noise distribution in layer 2, scale ADC channels.

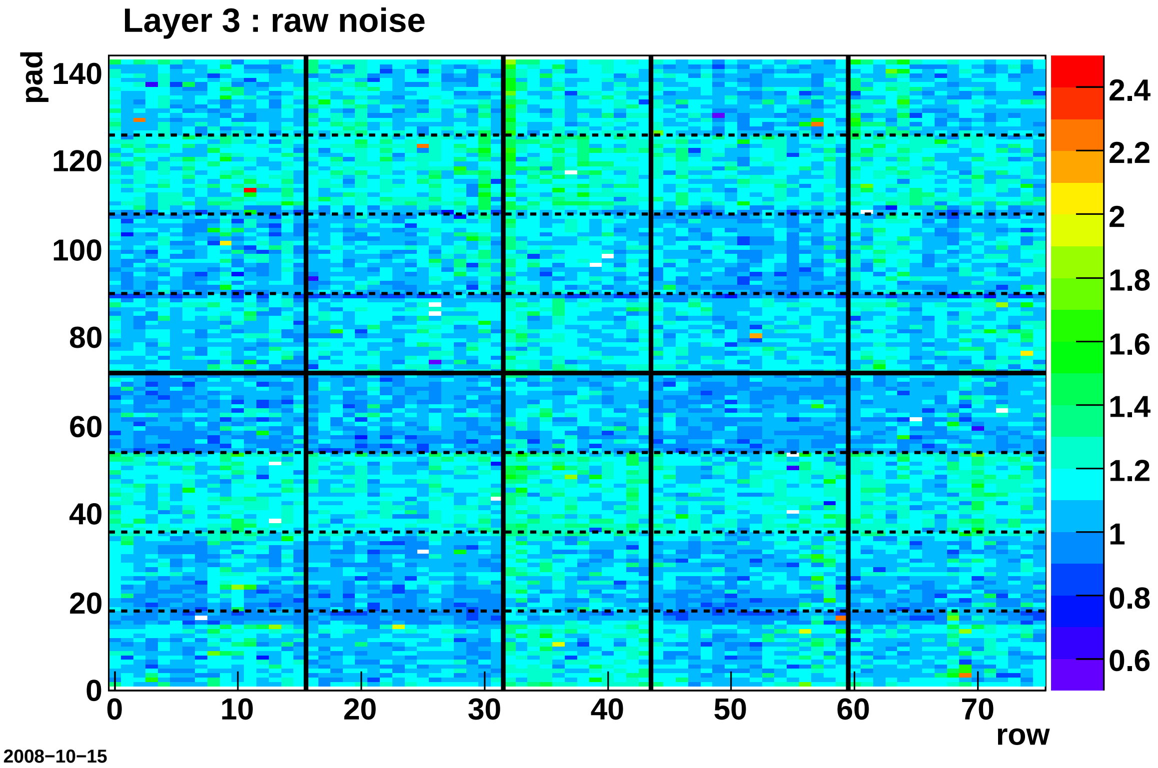

Figure 3.21: Raw noise distribution in layer 3, scale ADC channels.

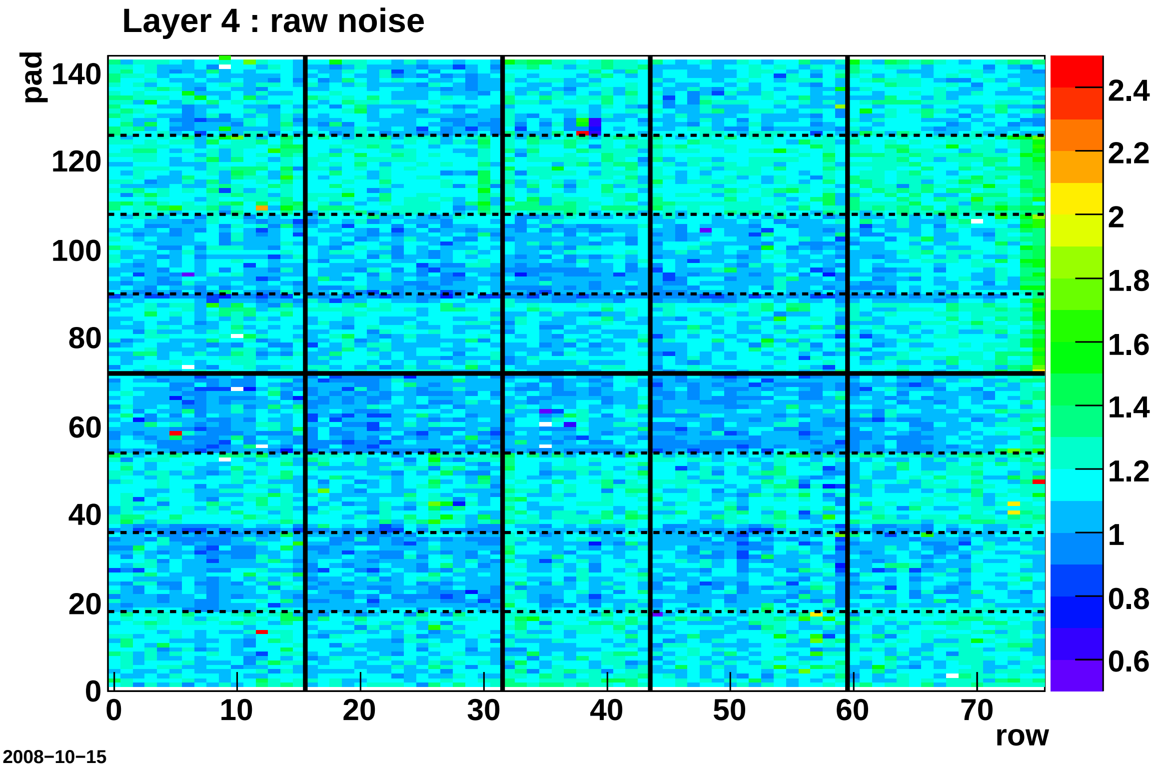

Figure 3.22: Raw noise distribution in layer 4, scale ADC channels.

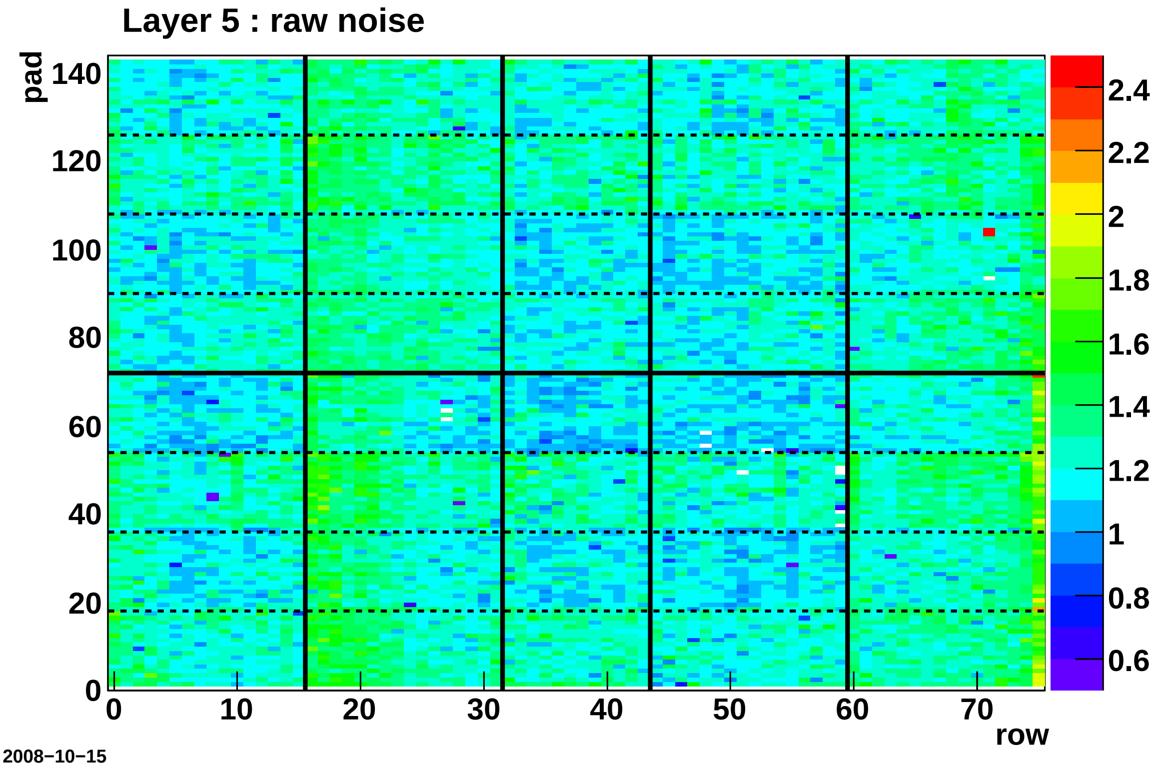

Figure 3.23: Raw noise distribution in layer 5, scale ADC channels.

onto a row of the noise distribution of the entire layer. On top of each figure one can see the corresponding pad row PCB layout. In the following we will highlight the correlation between PCB shape and static pad capacitance.

In order to be able to understand the static pad capacitance distribution, some deeper background information is required :

The pad planes of the TRD were designed hand in hand with the electronic readout boards. The geometry of the readout boards, i.e. their size and the position of signal cable cutouts, is tightly related to the pad plane layout. All readout board types have a unique four by four cutout spacing. Flat signal cables soldered onto the pad plane are fed through these cutouts to the PASA input connectors on the ROBs. The gaps between MCM columns (in ϕ-direction) are sized 180 mm, 80 mm and 80 mm. The large 180 mm gap accommodates the DCS and ORI boards.

At the time of the pad plane design, the TRD consisted of 6 layers numbered from 1 to 6. There was no layer 0, yet. Also, it was intended to use 4 different types of readout boards only, instead of the 7 readout board types built for the final setup. The ROB size was chosen such that the pad plane of a L1C1 chamber (with highest pad density) was entirely covered with 8 ROBs, arranged two by four. This fixed the position of the flat cable footprints in ϕ-direction for the layer 1. Towards higher layers the chamber width grows on average by 44 mm from one layer to the next. This extra space gives more freedom in positioning the ROBs along ϕ-direction. The ROBs were placed in a way that traces running from the pads to the flat cable footprints number 3 and 7 (counting from left to right and starting from 1) were looking almost symmetrical.

Later on, a layer 0 was introduced as a replacement for layer 6 to better accommodate the super modules within the detector envelope. This new layer is 44 mm narrower than layer 1 and the initial ROBs did not fit anymore to this new layer. The ROBs had to be shortened by 22 mm in ϕ-direction in order to match the layer 0 chambers. The cutout spacing had to be conserved for the ROBs. It was decided to cutoff a band on the ROB rim oriented towards the center of the chamber. From then on, the TRD had layers numbered from 0 to 5 and there were 7 different types of readout board, one type being used in two places.

Coming back to the six capacitance distributions (Figures 3.24 to 3.29). Each capacitance distribution has 8 local peaks along a pad row. Each of these capacitance peaks is position-correlated to a flat cable footprint on the PCB.

The pad plane of layer 1 (figure 3.25) has the ROBs placed symmetrically. The peaks for MCM number 2 and 6 are shifted into the area of their respective right neighbour due to the large gap for the DCS board. This asymmetric placement of the footprint with respect to the pad group center generates the plateau-like capacitance distribution around 22 pF. As these footprints are located on top of pads belonging to a different MCM, the two capacitance peaks are very well pronounced. Footprints with a more symmetric fan-out result in a lower average capacitance and their distribution appears symmetric towards the peak.

Comparing layer 0 (figure 3.24) to layer 1, the distributions look very similar. The peak of MCM number 2 is slightly offset to the right, since the pads are a little thinner. As the readout board on the right side got effectively shifted to the left by 44 mm the capacitance peak of MCM 6 dropped in amplitude and width.

For layers 2 (figure 3.26) and higher, there is more freedom to place the ROBs due

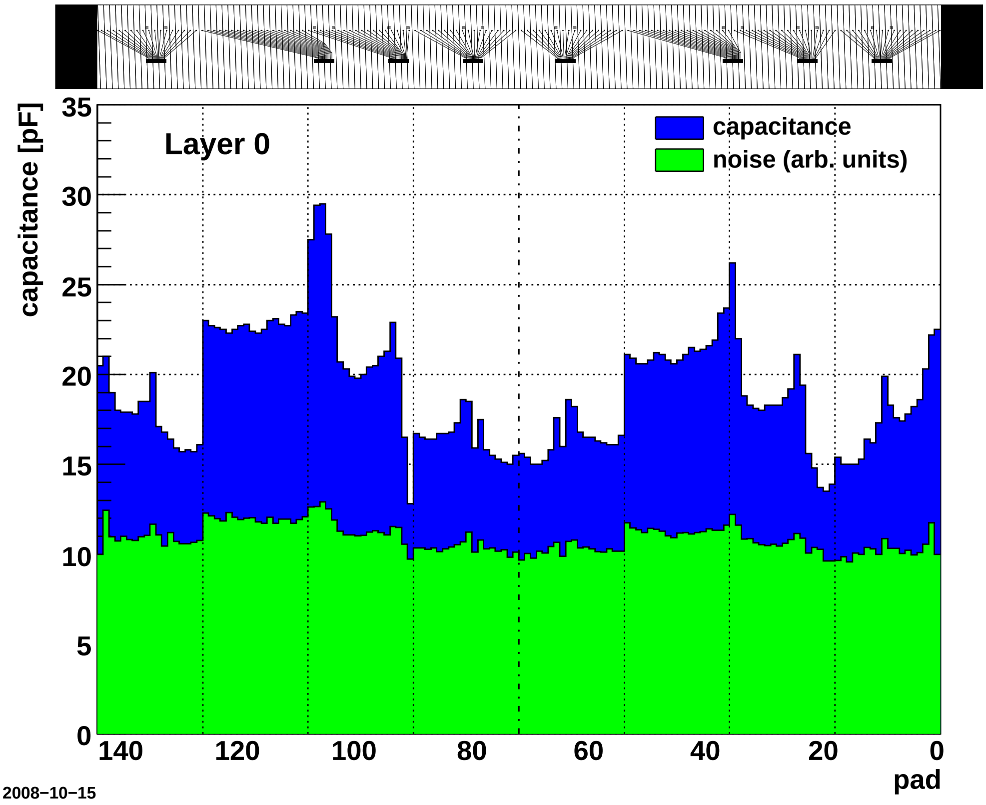

Figure 3.24: Pad capacitance, average noise in a row of L0C0.

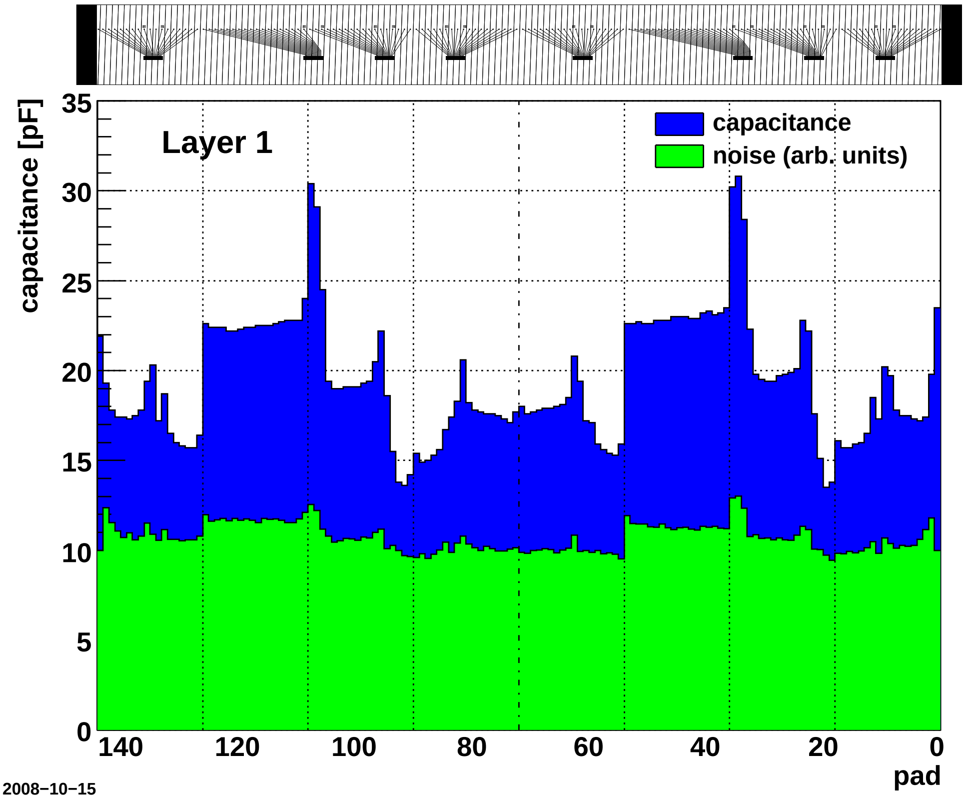

Figure 3.25: Pad capacitance, average noise in a row of L1C0.

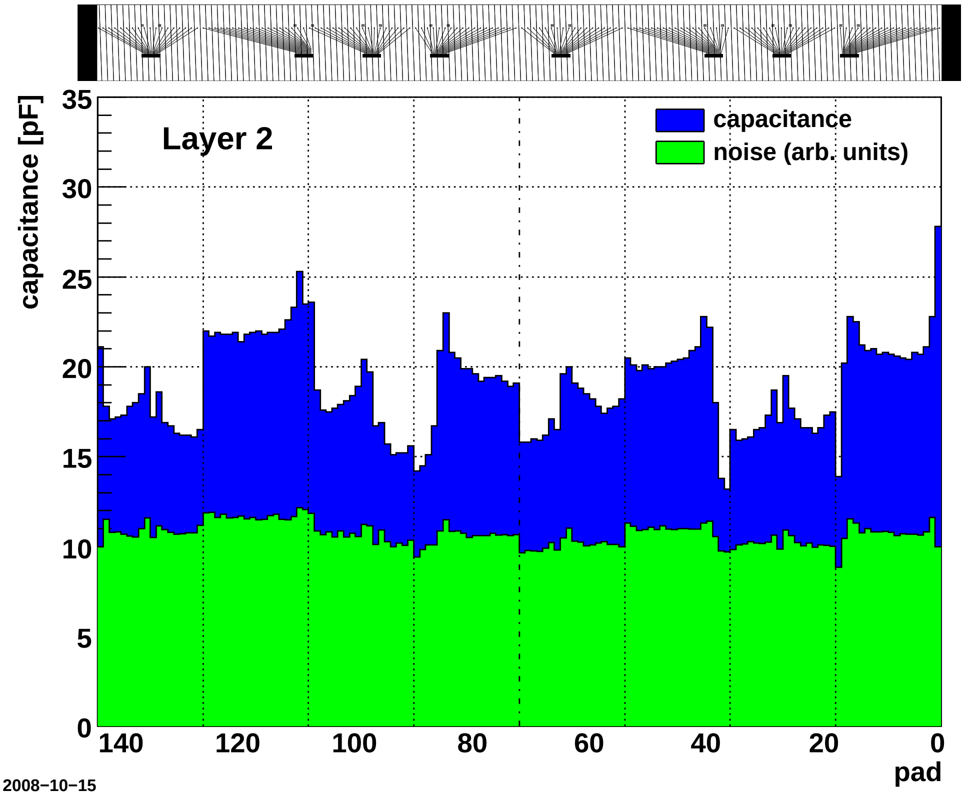

Figure 3.26: Pad capacitance, average noise in a row of L2C0.

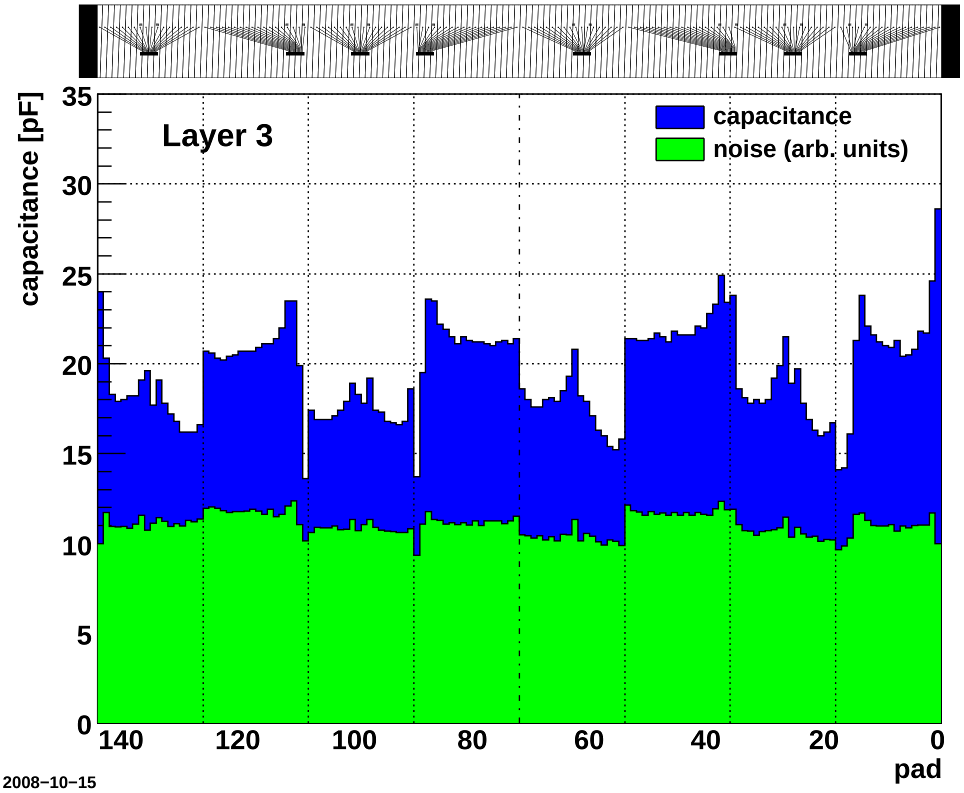

Figure 3.27: Pad capacitance, average noise in a row of L3C0.

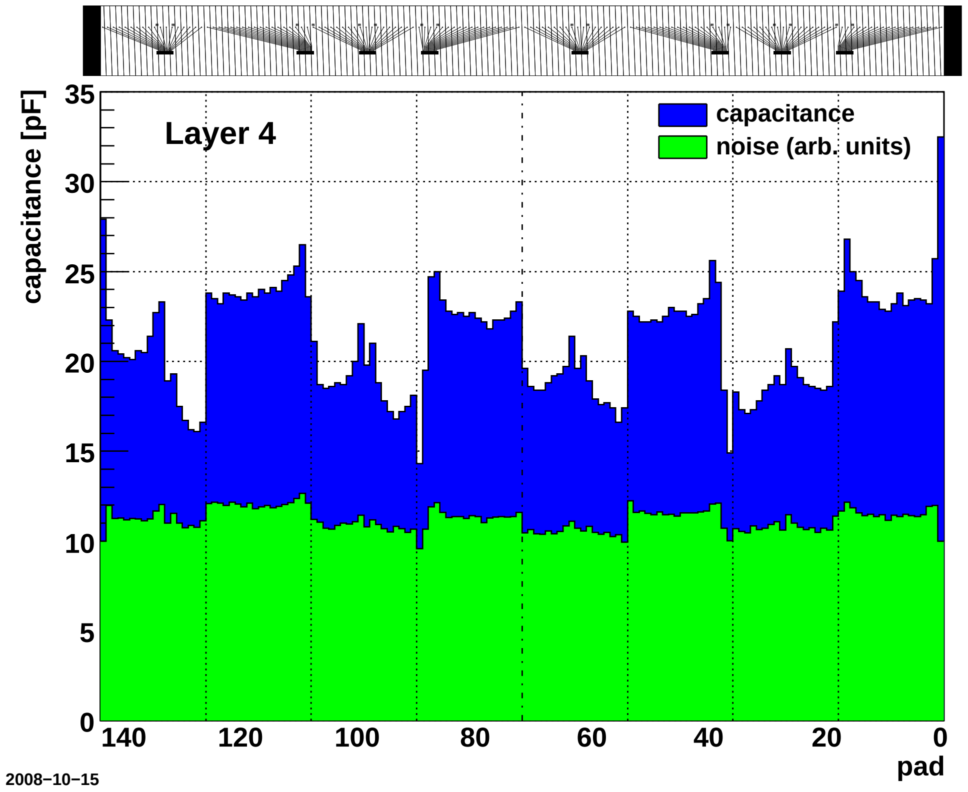

Figure 3.28: Pad capacitance, average noise in a row of L4C0.

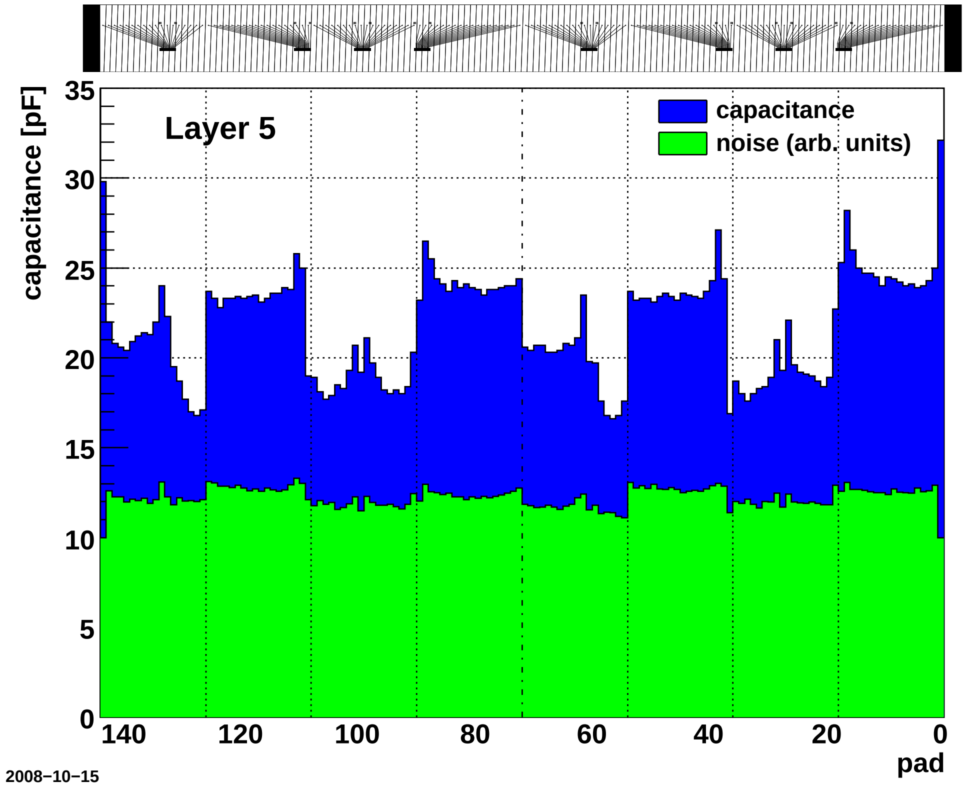

Figure 3.29: Pad capacitance, average noise in a row of L5C0.

to the increase in pad width. They are positioned in a way that MCM 3 and 7 have an almost symmetric fanout shape. Thus the neighboring footprints get increasingly asymmetric fan-outs. Footprints 2 and 6 are shifted to the right while 4 and 8 are forced to the left. As a consequence one can observe 4 plateaus for MCMs 2, 4, 6 and 8 emerging in layer 2. These plateaus grow in width and amplitude the higher and wider the layer. In the pad space the local capacitance peaks are displaced towards the MCMs 3 and 7.

Through some of the layers, single pads with low capacitance are visible as dips in the distributions (1 pad in layer 0, 2 in layer 2, 2 in layer 3, 2 in layer 4). These almost ideal traces are characterized by a short distance between the via and the footprint and usually do not leave the area of their own pad. The capacitance distribution shown in the 6 figures was measured for one distinct pad row in each layer. The position of the footprints in a layer is always identical along ϕ-direction. However, due to variations of the relative footprint distance to the center of the pad in z-direction, the pad tilt and the top or down orientation of the fan-out (see C0-type pad planes in figures B.1 to B.6), there are slight capacitance variations from row to row. Averaged over the 76 pad rows of a layer, only few of the low capacitance pads endure.

3.2.3 Correlation of noise and static pad capacitance

A remarkable aspect of Figures 3.24 to 3.29 is the very similar shape of the average noise distribution in a row (green) and the pad capacitance distribution (blue). The noise originates from the signal processing in the electronics and is basically driven by the PASA and the ADC. While the noise of the PASA has a linear dependence on the input capacitance (equation 3.6), the ADC contributes a fixed value to the noise (equation 3.7). The measured total noise is given in equation 3.8.

$$noise_{PASA} = a \times C + b \tag{3.6}$$

$$noise_{ADC} = d \tag{3.7}$$

$$noise_{TOTAL} = \sqrt{noise_{PASA}^2 + noise_{ADC}^2} \tag{3.8}$$

Figure 3.30 shows the distribution of noise versus capacitance in a 2-dimensional histogram for all available clean layers (from 0 to 4). The measured noise appears to be very well correlated with the pad capacitance. The distribution can be fitted with equation 3.8 for the total noise. An independent measurement [33], fixes the noise contribution at 0 pF input capacitance to $214e$ (parameter b in equation 3.6). The two remaining parameters, the PASA slope and the constant ADC contribution are then determined by a fit to the data. Results are given in equations 3.9 and 3.10.

$$noise_{PASA} = 214e + C \times 25.4e/pF \tag{3.9}$$

$$noise_{ADC} = 730e \tag{3.10}$$

The fit result for the PASA noise (3.9) is identical to a previous measurement preformed on a standalone PASA chip, see [33].

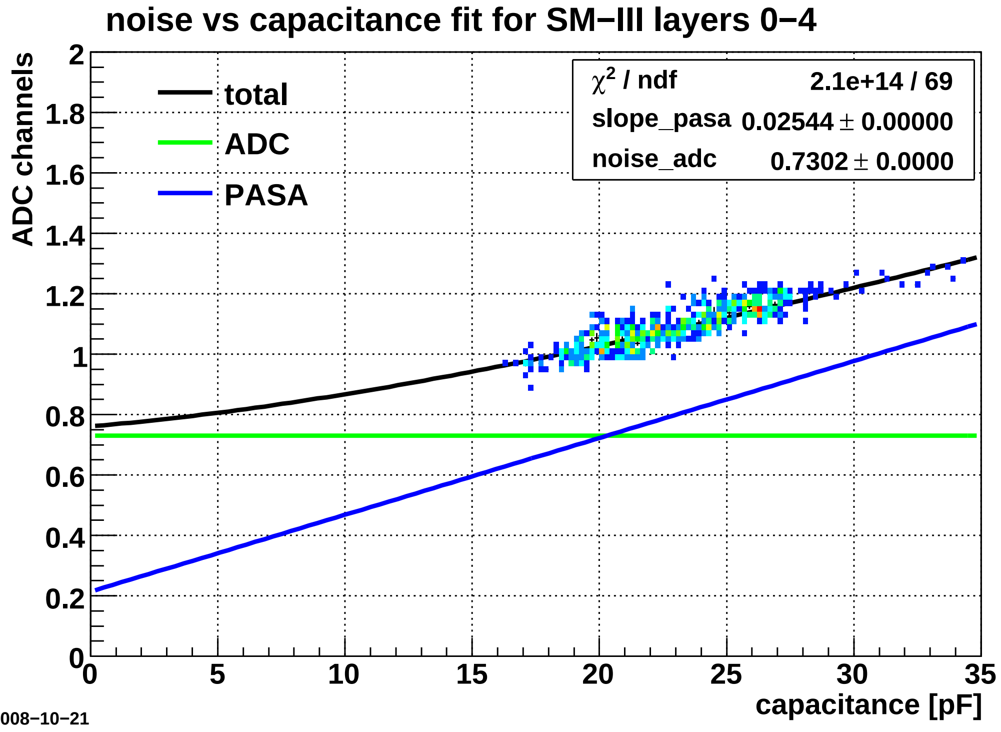

Figure 3.30: Fit (black) of the average noise distribution versus pad capacitance for SM III. The linear PASA (blue) and constant ADC (green) contribution are shown.

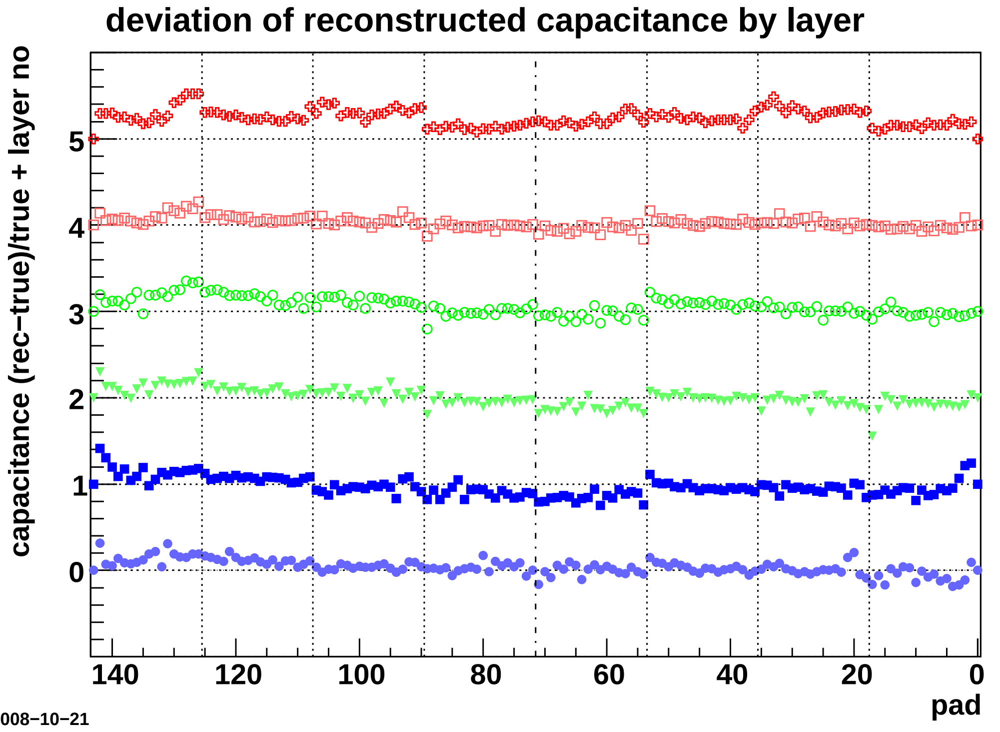

Figure 3.31: Relative deviation of reconstructed against true capacitance, layer by layer. The vertical dotted lines represent the boundaries between MCMs in a row.

The $noise_{TOTAL}$ function used for the fit can be inverted to obtain $noise^{-1}_{TOTAL}$. Using this inverted function, a reconstructed pad capacitance can be derived from the average noise of a row. The relative deviation of reconstructed capacitance against true capacitance for all layers is visible in Figure 3.31, the curves were shifted by the corresponding layer number for better visibility. The outermost bins were forced to 1. The five clean layers (0-4) are on average well reconstructed.

A slight linear trend falling towards lower pad numbers (from left to right) is visible in layers 0 to 4. Also a 10% bump in the noise level is visible at the limit between the 1st and the 2nd MCM from the left (around pad number 126). This coincides with the location of the DCS board and the ORI board of the ROB B-side. A little step is visible between the 5th and the 6th MCM, corresponding to the location of the ORI board on the ROB A-side. All these effects, the bump and the step might be due to the influence of the DCS and ORI circuits onto the readout board. Further investigations would be required to come to a final statement. Layer 5 shows 20% excess noise caused by the noise hot spots, as initially observed in Figure 3.23.

3.2.4 Correcting for pad capacitance induced noise

Along pad rows

As shown in Figure 3.30, the noise is well correlated with the pad capacitance. The noise distributions averaged over a layer can thus be used to correct the noise distribution for each individual row. The average noise distributions from Figures 3.24 to 3.29 are then employed as weighting factor to correct the individual noise distribution of a row by division for each pad. Noise plots corrected for their capacitance variation are presented in Figures 3.32 to 3.37. A little remnant noise appears in the corners of a few chambers. The non-intrinsic noise in layer 4 and especially in layer 5 becomes highlighted in those figures, it is again located towards the borders of the chambers.

Along pad columns

A similar correction procedure could be applied to the noise distributions in pad columns (along z-direction). The pad length usually differs between C0- and C1-type chambers. For layers 0 and 1, the inner pads in the central stack are 15 mm (20%) longer than those in the 4 outer stacks. This leads to increased capacitance and thus higher noise. For layers 2 and above this effect is marginal, as the length of the pads in C0- and C1-type chambers becomes comparable.

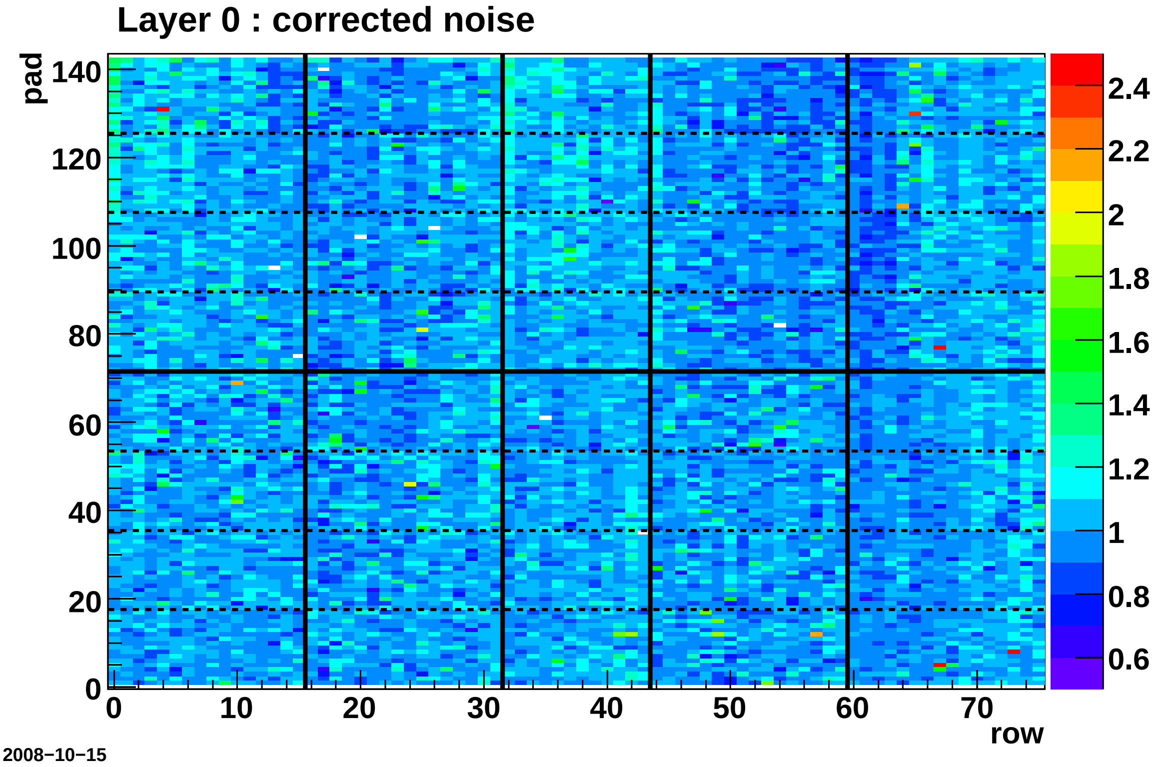

Figure 3.32: Corrected noise distribution in layer 0, scale ADC channels.

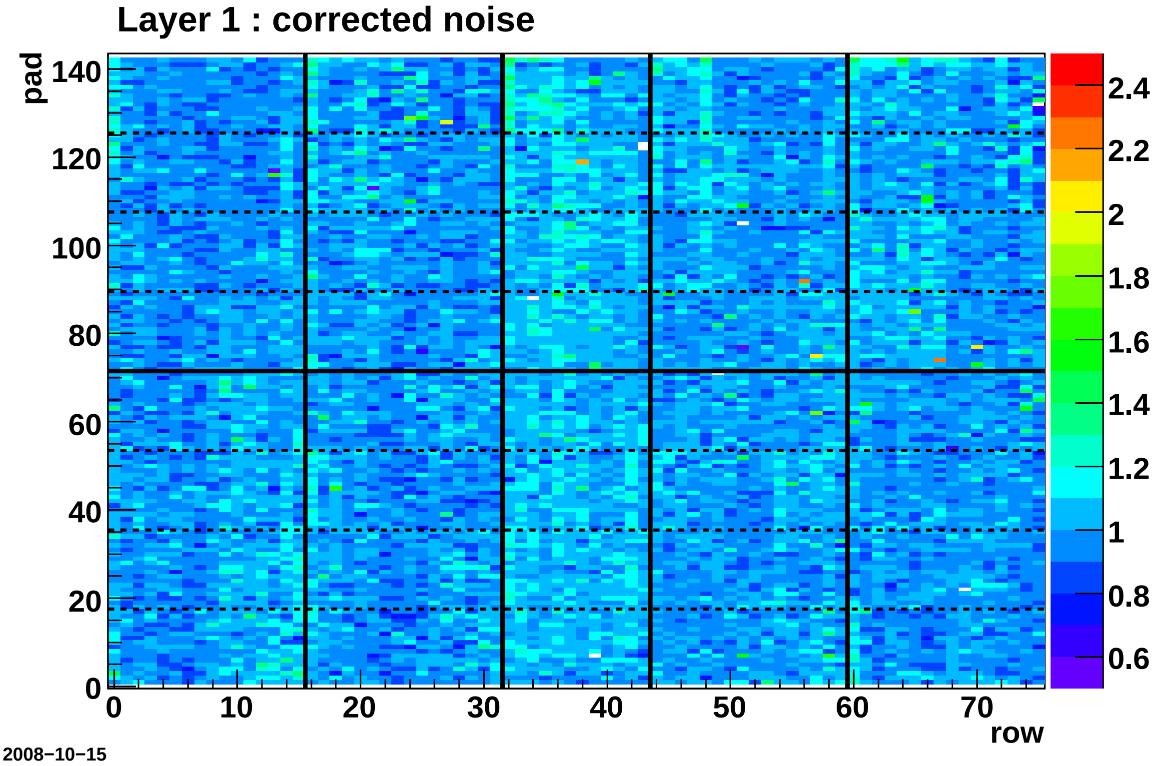

Figure 3.33: Corrected noise distribution in layer 1, scale ADC channels.

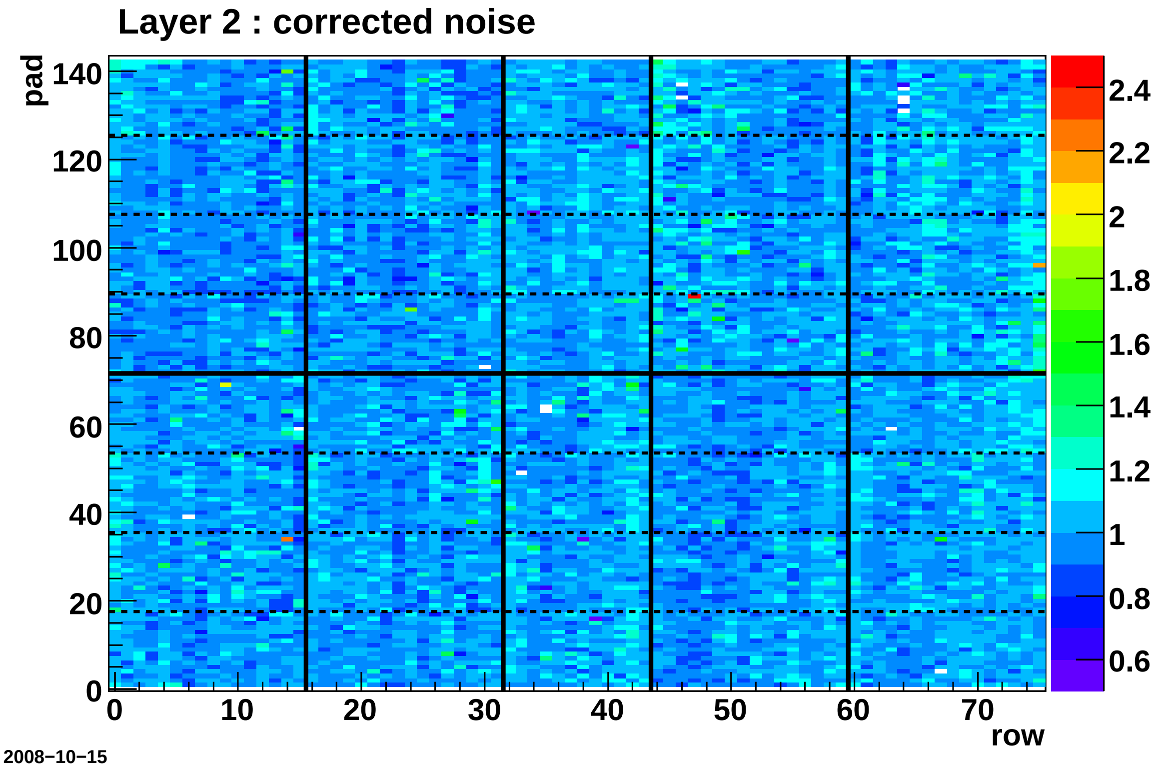

Figure 3.34: Corrected noise distribution in layer 2, scale ADC channels.

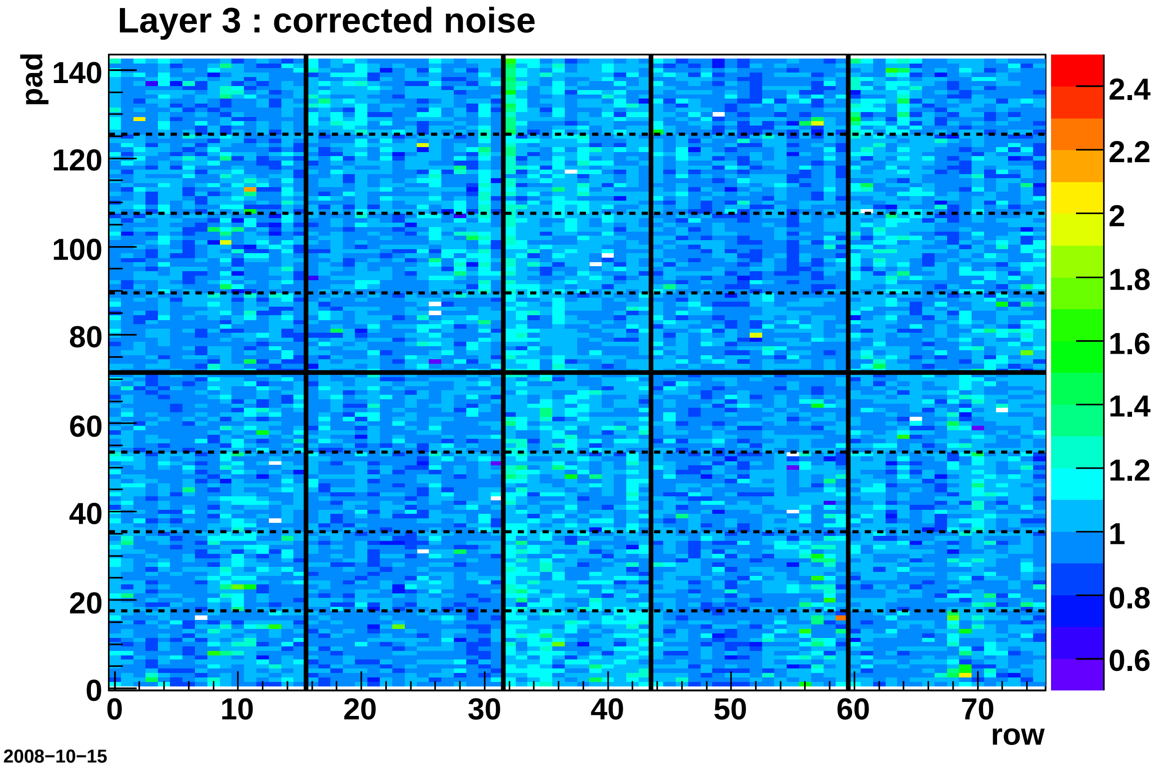

Figure 3.35: Corrected noise distribution in layer 3, scale ADC channels.

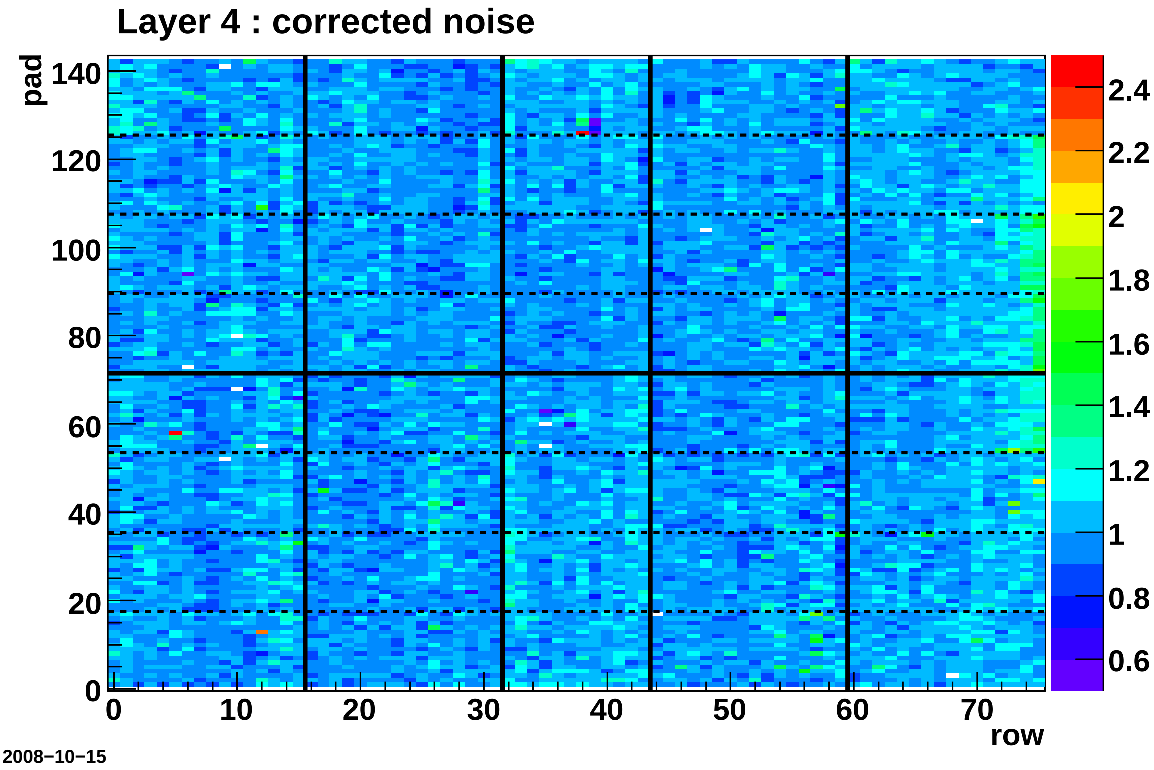

Figure 3.36: Corrected noise distribution in layer 4, scale ADC channels.

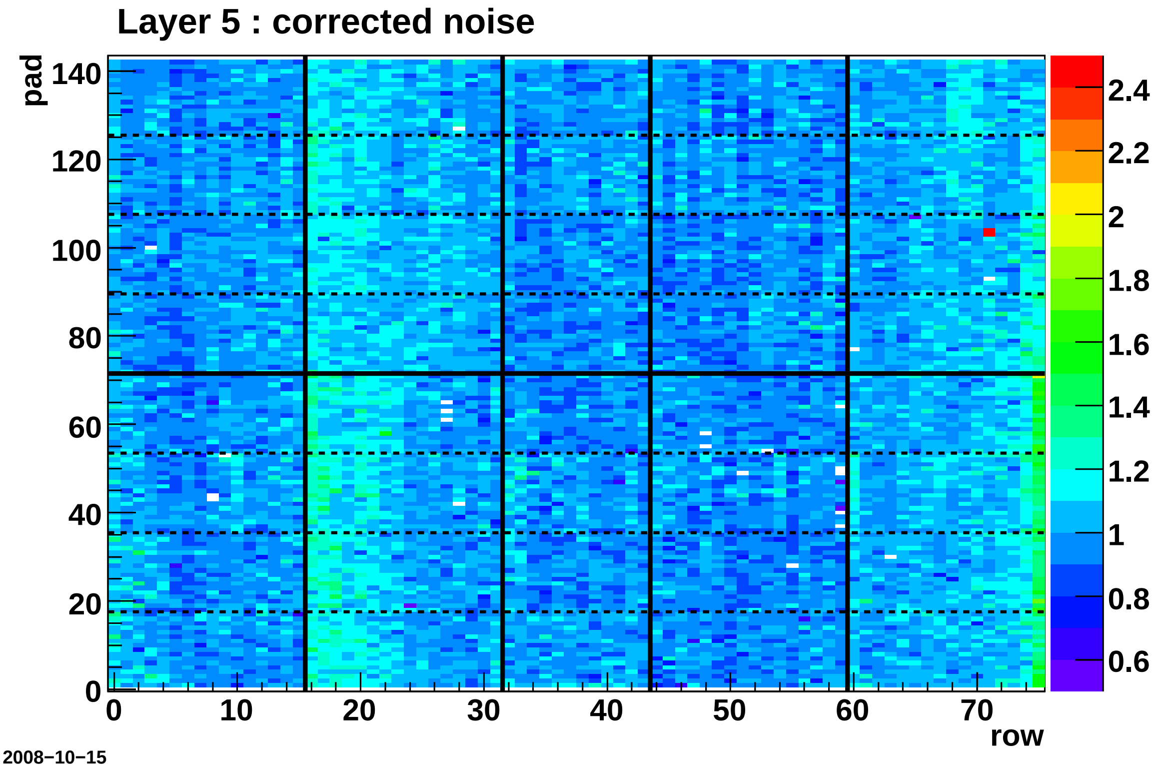

Figure 3.37: Corrected noise distribution in layer 5, scale ADC channels.

Chapter 4

Low voltage power distribution

4.1 Overview

Including the TRD infrastructure, a total of three subsystems needs to be supplied with low voltage :

- the 18 TRD super modules with their front-end electronics
- the Pre-Trigger system
- the Global Tracking Unit (GTU) and the Power Control Unit (PCU)

The core element of the TRD low voltage system is the water cooled Wiener PL512/MARATON (MAgnetic field and RAdiation TOleraNt) floating power supply, 89 units provide a total of 255 independent low voltage channels. We use four different types of power supply units, they differ in the number of output channels, voltage and current range, as detailed in Table 4.1.

type	subsystem	number of supplies	location	voltage range	number of channels and I_{max}
1	super modules	54	I/O-racks	2-7 V	2x 220 A
2		28	I/O-racks	2-7 V	3x 165 A + 1x 55A
3	pre-trigger	4	I/O-racks	5-15 V	2x - 6x 22 A
4	GTU and PCU	3	C-racks	2-7 V	3x 110 A + 4x 55A

Table 4.1: Number, location and type of the 89 low voltage power supply units.

4.2 Low voltage for the super modules

The main consumer of low voltage electricity in the TRD is the front-end electronics located on the backside of each chamber. The 4104 readout boards of the TRD are equipped with 1080 ORI boards and 70848 MCMs, these need to be supplied with four different voltage channels. In addition there are 540 DCS boards which are supplied

Figure 4.1: Photo of two racks with low voltage supplies during installation. Once fully equipped these two racks will power 4 super modules.

Figure 4.2: A low voltage patch panel, here sector 14 in the baby frame.

no	channel type	layers
01	A1.8V L01	2 (pair)
02	D1.8V L01	2 (pair)
03	A1.8V L23	2 (pair)
04	D1.8V L23	2 (pair)
05	A1.8V L45	2 (pair)
06	D1.8V L45	2 (pair)
07	A3.3V L01	2 (pair)
08	A3.3V L23	2 (pair)
09	A3.3V L45	2 (pair)
10	D3.3V L05	6 (all)
11	PDB	6 (all)

Table 4.2: List of all the voltage connections to a super module.

through the power distribution boxes (PDB), independently from the rest of the electronics. More than 65kW of electrical power are consumed in the front-end electronics, not accounting for the voltage drop in the power cables.

The TRD is located inside the L3 magnet which is considered as a closed volume. Every detector needs to cool away the self dissipated heat. As a consequence the TRD front-end electronics is equipped with ultra-low-drop voltage regulators to produce a minimum of heat and a water cooling system to take away the rest. Each MCM is covered by a thin aluminium plate acting as head conductor towards the cooling meanders.

The low voltage power supplies are magnetic field tolerant up to 300 Gauss (= 0.03 T), but they cannot be operated inside the L3 magnet as the nominal magnetic field rises to 0.4 T. The supplies are installed in racks outside the L3 magnet (see Figure 4.1) operating in a reasonable magnetic stray field of 80 Gauss. The racks are located on the I- and O-sides close to the magnet doors to minimise the cable length and thus voltage drop.

Cable bulk and weight of the copper conductors were a major challenge during cable installation. As the available space in the L3 magnet chicanes is limited, the cables for the read-out board power had to be divided between A- and C-sides. The majority or

number	channels	service	currents	comments
18	2x 220 A	A1.8V L01	120 A	
		D1.8V L01	124 A	
18	2x 220 A	A1.8V L23	120 A	
		D1.8V L23	124 A	
18	2x 220 A	A1.8V L45	120 A	
		D1.8V L45	124 A	
18	3x 165 A	A3.3V L01	108 A	PASA
		A3.3V L23	108 A	PASA
		A3.3V L45	108 A	PASA
	1x 55 A	—	—	not used
10	3x 165 A	D3.3V L06	118 A	
		PDB (1SM)	30 A	60A for two SM
		—	—	used by other SM
	1x 55 A	—	—	not used

Table 4.3: Typical low voltage currents in the 11 channels of a super module during operation. 82 power supply units are needed to power the 18 TRD sectors.

load	channel	power consumption in one super module		voltage at	
				SM input	end of SM
PASA	A3.3V	3x 425W =	1275W	3.92V	3.52V
ADC	A1.8V	3x 290W =	870W	2.43V	2.00V
TRAP	D1.8V	3x 300W =	900W	2.41V	1.98V
TRAP	D3.3V	1x 445W =	445W	3.76V	3.39V
DCS boards	PDB	1x 120W =	120W	4.03V	3.60V
	1 super module total		3610W		
	18 super modules total		65150W		

Table 4.4: Low voltage power consumption for 1 TRD super module, at 1.5kHz L1A trigger rate, only pedestal filter enabled.

the sectors are powered from the C-side, except for the four sectors 12-15, which receive their power from the A-side. The low voltage power for the DCS boards is supplied from the C-side for all sectors. Racks are allocated led by the asymmetric cabling : 2 racks with crates on the A-side of the magnet and 8 racks on the C-side, see Figure A.1. The cross-section of the power cables, starting in the racks with 150 mm^2, was doubled after passing the chicanes to 300 mm^2 inside the magnet, in order to reduce heat dissipation. The patch panel interface to a super module is shown in Figure 4.2.

Each super module is connected to 11 low voltage channels, the channel mapping is given in Table 4.2. The distribution of the 11 channels onto the power supply units together with typical currents is denoted in Table 4.3 and Table 4.4 summarises the power consumption per channel and for the full detector. Usually a low voltage channel powers a pair of 2 neighbouring layers, exceptions are the the PDB and D3.3V channel

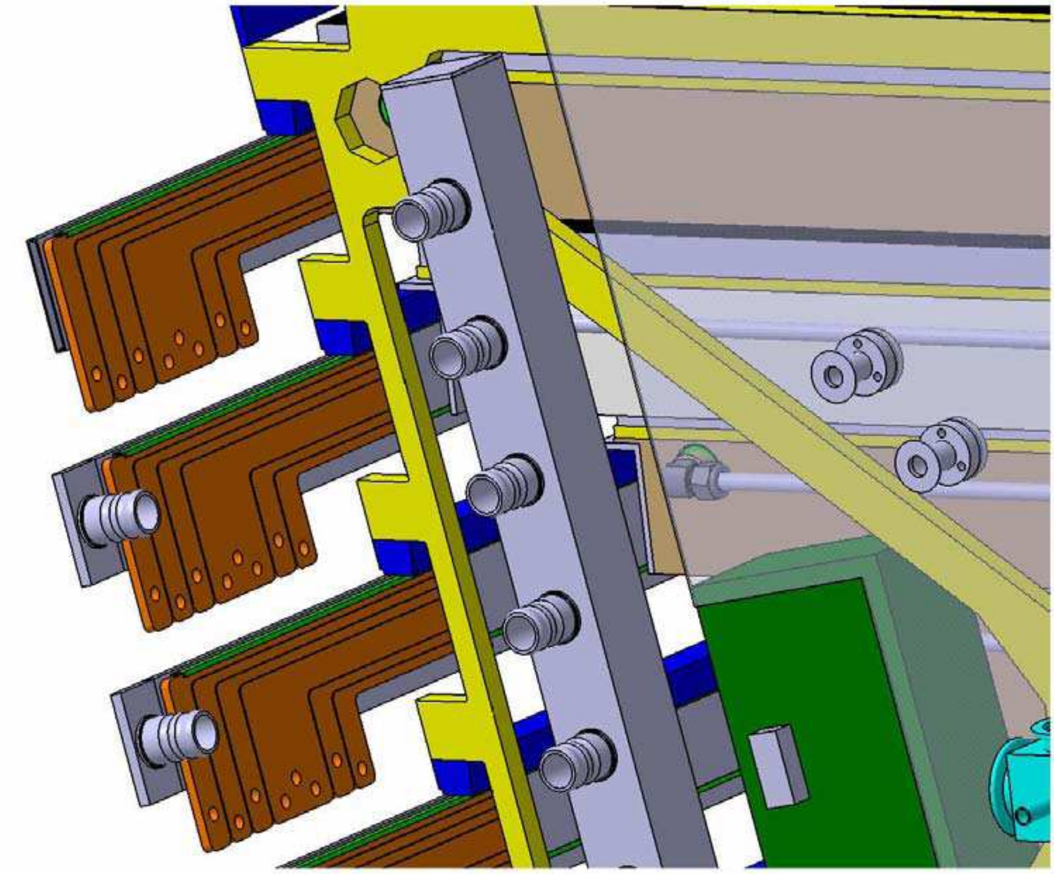

Figure 4.3: Power bus bars sticking out at the super module end cap, A-side.

Figure 4.4: Cross-section of a low voltage bus bar.

powering the entire super module. At least five power supplies are required to power a super module, the low voltage distribution scheme is depicted in Figure A.2. Channels (A1.8V, D1.8V, A3.3V) powering layer pairs are supplied from a stack of 4 Wieners with fixed mapping for all sectors. The D3.3V and PDB channel originate from one or two additional power supplies. The free grouping of D3.3V and PDB channels allowed to save 8 power supplies.

The currents are guided from the patch panels to the electronics through bus bars running all along the super module length, see Figure 4.3. Each of the four power channels has its own 36 mm^2 conductor, see Figure 4.4. Only the return line of the 3

TRAP/ADC channels is grouped, the PASA has a dedicated A3.3V return line. The large cross-sections of the bus bar allow to keep the voltage drops around 0.4 V along the 7 m length of the super module (Table 4.4).

The power distribution boxes share a common LV channel between two neighbouring super modules. Each PDB has point-to-point connections to the 30 DCS boards in its super module. The PDBs are controlled remotely by the Power Control Unit (PCU) as described in a later section.

4.2.1 Optimisation of the SM low voltage

# of PSUs	channels	services	currents	comments
18	3x 165 A	A1.8V L01	120 A	layers 0+1
		D1.8V L01	124 A	
		A3.3V L01	108 A	
	1x 55 A	D3.3V L01	39 A	
18	3x 165 A	A1.8V L23	120 A	layers 2+3
		D1.8V L23	124 A	
		A3.3V L23	108 A	
	1x 55 A	D3.3V L23	39 A	
18	3x 165 A	A1.8V L45	120 A	layers 4+5
		D1.8V L45	124 A	
		A3.3V L45	108 A	
	1x 55 A	D3.3V L45	39 A	
2	10x 55 A	PDB (1SM)	30 A	9 channels for 9 PDBs

Table 4.5: Optimised low voltage power setup. A pair of layers is fully served by one power supply. Each super module has an individual PDB channel. The 18 TRD sectors are powered by 56 power supplies only, instead of 82. Knowledge of exact power consumption of the electronics PASA + TRAP would have been required during the planning phase of the LV cabling in 2005.

The current layout of the LV system does not exploit the full capacity of the 82 power supplies in charge of powering the super modules. A total of 31 out of 220 channels are not used in the current setup. The units powering the A1.8V and D1.8V channels are operated at 60% respectively 50% of their nominal current of 200A. On each of the units powering the A3.3V and D3.3V channels the fourth (50A) channel is not used at all. In the super modules the LV is usually distributed in units of layer pairs (three per super module). Except for the D3.3V channel supplying the full super module, which is entangling the layers. The power to the PDB is delivered to a group of two neighboring super modules sharing the same channel.

It would have been more elegant to power the layer pairs individually with the four voltage types, not sharing the D3.3V across the full super module. The recovery procedure from single channel trips would be simpler. Also, keeping the super modules separated from each other using individual PDB channels would have been advantageous. The LV power consumption of a layer pair amounts to 120 / 124 / 108 / 39

/ 30 A for the A1.8V / D1.8V / A3.3V / D3.3V / PDB channels. Choosing supplies with 150 / 150 / 150 / 50 / 50 A nominal current per channel would have allowed the following simple setup, also detailed in Table 4.5 : The low voltage power of a full layer pair is provided by a single type of supply with the following channel mapping : 3x 150A + 1x 50A. This PSU is identical to the 28 PSUs currently used for A3.3V and D3.3V. The 50A channels are used for the D3.3V lines. Only 54 supplies would be required to provide power for all TRD readout boards. The PDBs need to be powered by 18 individual low voltage channels, for this 2 PSUs with 10x 50A would be required. Only 2 out of 236 channels would be unused with this layout. The required rack space would shrink from 10 to 6 racks. One can argue that a failure of a PDB supply would stop the operation of 9 super modules. This could however be minimised by the use of 2 additional power supplies of this type. The number of connections to the super module would increase from 11 to 13, on the other hand the cable cross-sections for the D3.3V line could be reduced. The streamlined version of the super module LV system would have reduced the complexity of the setup and and saved more than 200 kCHF. Unfortunately the system layout could not be altered anymore once the order for the cable infrastructure inside the L3 magnet had been placed.

4.3 Low voltage for the pre-trigger system

The low voltage power for the pre-trigger system is provided by 4 power supply units installed close to the four corners of the L3 magnet. As visible in Figure A.3, page 101, it is taken care that all pre-trigger system components can be redundantly powered. Each pre-trigger crate can be supplied either from the I– or O–side. The availability of the pre-trigger system is mandatory for operation of the TRD.

4.4 Low voltage for the GTU and PCU

The 3 seven-channel power supplies in the C-racks provide the low voltage power for the GTU and the PCU. The GTU consists of 9 cPCI crates installed in 3 racks, as sketched in Figure 4.5. A super module is connected to a GTU partition, two partitions make up a crate. Each GTU crate is powered by 2 channels (5.0V and 3.3V) from the local power supply in the same rack. The GTU crate of SM04/13 located in the center of rack C17 houses in addition the TGU, which is the interface of the TRD to the trigger. The power supply alidcswie091 in rack C17 is the single point of failure in the TRD LV system as it is the unique source of power for the TGU, there is no redundancy forseen. Should this supply fail, the TGU would be off and as a consequence the TRD would be down. To assure proper startup of the GTU crates, the 2 LV channels of a GTU crate must be simultaneously switched on or off, which can be hard-coded in the power supply.

The Power Control Unit (PCU) in rack C18 is in charge of remotely controlling the 540 DCS boards in the TRD super modules. Each DCS board can be individually power-cycled. To switch on the front-end electronics on a TRD chamber it is mandatory that the local DCS board is up. As top level controller node of the TRD power the PCU needs a redundant design. It consists of 2 redundant pairs of DCS boards, 4 boards in

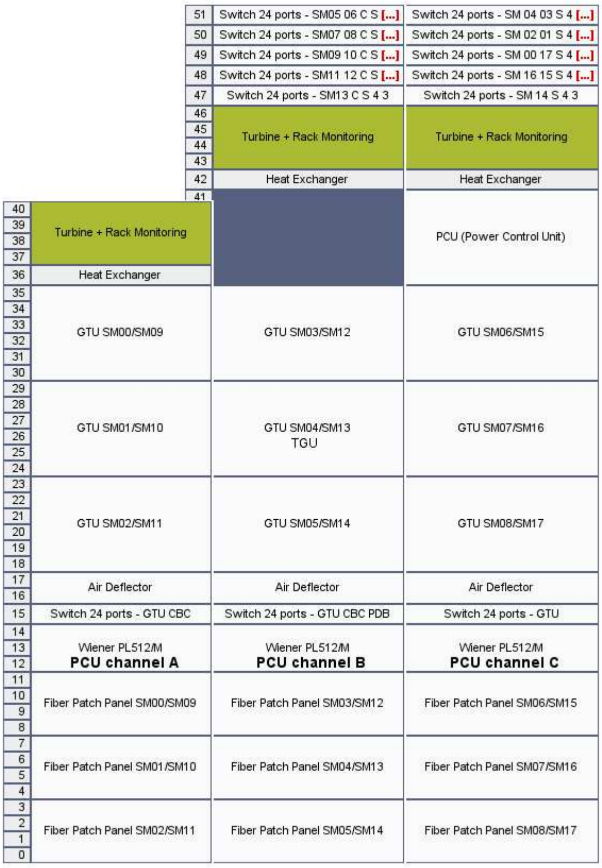

Figure 4.5: The GTU racks as defined in the ALICE racks depot database.

rack	power supply	channel	line	PCU boards			
C16	alidcswie090	U9	A	00	01		
C17	alidcswie091	U9	B			02	03
C18	alidcswie092	U9	C	00	01	02	03

Table 4.6: Low voltage channel mapping of the PCU.

total. Each DCS board (pair) can power up 9 (all) super modules. The PCU itself is equipped with redundant low voltage power. A power line from each supply in each of the three C-racks connects to the PCU as listed in Table 4.6. Even if the main power in any 2 out of the 3 C-racks was down, the PCU would remain operational.

4.4.1 Load balancing

Electrical power in the cavern is distributed through 3 phases labeled R, S and T. During the planning phase it was made sure that the load of the 89 power supply units is equally balanced on all 3 phases for a completely installed TRD at full load.

4.5 The power-up sequence of the TRD

During power-up of the TRD a well defined sequence of steps, summarised in Table 4.7, has to be followed. This procedure will finally be handled by a final state machine running in the detector control system. Once fully powered, the TRD detector and it's infrastructure consume roughly 70 kW of power provided by 224 channels in 89 supplies.

action	steps	# supplies	# channels
power up the infrastructure :			
	switch on the Pre-trigger system	4	14
	switch on the GTU crates	3	18
	switch on the PCU crate	(3)	3
power up the 18 super modules :			
	switch on the PDBs	(5)	9
	switch on D3.3V	10	18
	switch on the 3 layer pairs	72	162
start up the electronics :			
	switch on the DCS boards from the PCU		
	switch on ROB power from DCS boards		
the TRD is powered with LV		89	224

Table 4.7: The power-up sequence of the TRD low voltage.

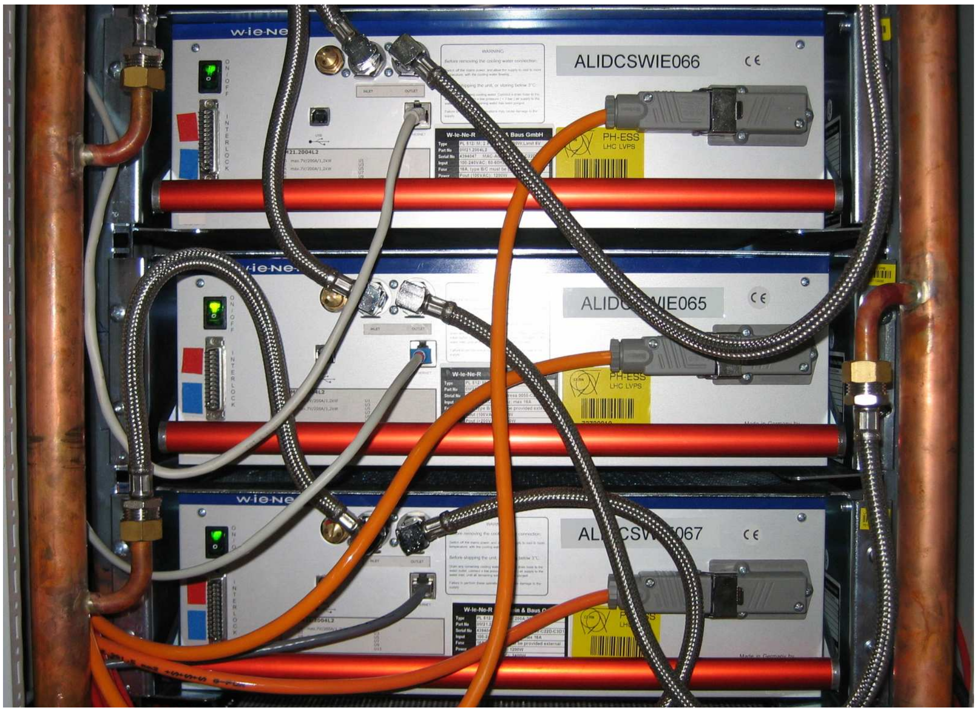

Figure 4.6: Photo of power supplies for surface testing.

Chapter 5

The TRD high voltage system

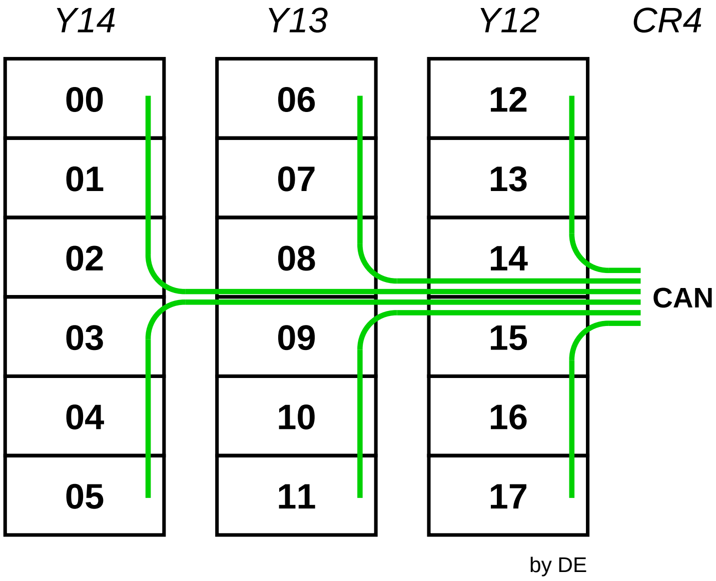

Figure 5.1: Location of the 18 ISEG crates in the racks of CR4. Each crate supplies drift and anode HV to one TRD sector, in total 1080 HV channels. The crates are controlled in groups of 3 by 6 individual CAN busses.

5.1 Requirements

The TRD HV system is located in counting room 4 (CR4), in the shaft to the ALICE cavern, in a zone free of magnetic stray fields. The baseline design of the TRD foresees individual high voltage power for the drift and anode voltages of each of the 540 detector chambers. Each channel should be independent in terms of voltage setting, current limit, switching on and off and monitoring of current and voltage. The ramp speed can be set by super module. The 18 TRD super modules are each connected via 2 multi-conductor HV cables, one for negative and one for positive voltages, the grounds of the individual sectors are separated.

The HV system offers 540 negative drift and 540 positive anode channels, bundled in groups of 30 channels, with a common ground for each super module. The ripple of both type of modules was specified to be smaller than 50mV peak to peak and the stability better than 0.1% over 24 hours.

The TRD will be operated with the nominal Xe/CO_2 (85%/15%) gas mixture. With a drift potential of -2100V applied over the 3 cm drift gap (700 V/cm) this results in a drift velocity of 1.5 cm/μs and a maximum drift time of 2 μs. At nominal voltages, the current through the resistor chain of the drift field cage amounts to 165 μA. The chosen negative HV modules can supply up to -2500 V with a current of up to 500 μA per channel.

The anodes are operated at $+1600$V in order to reach the required gas gain of 10^4, the currents can reach up to few μA during Pb–Pb collision. The chosen positive HV modules can deliver up to $+2500$ V with a current of up to 20 μA per channel.

5.2 High voltage power supply modules

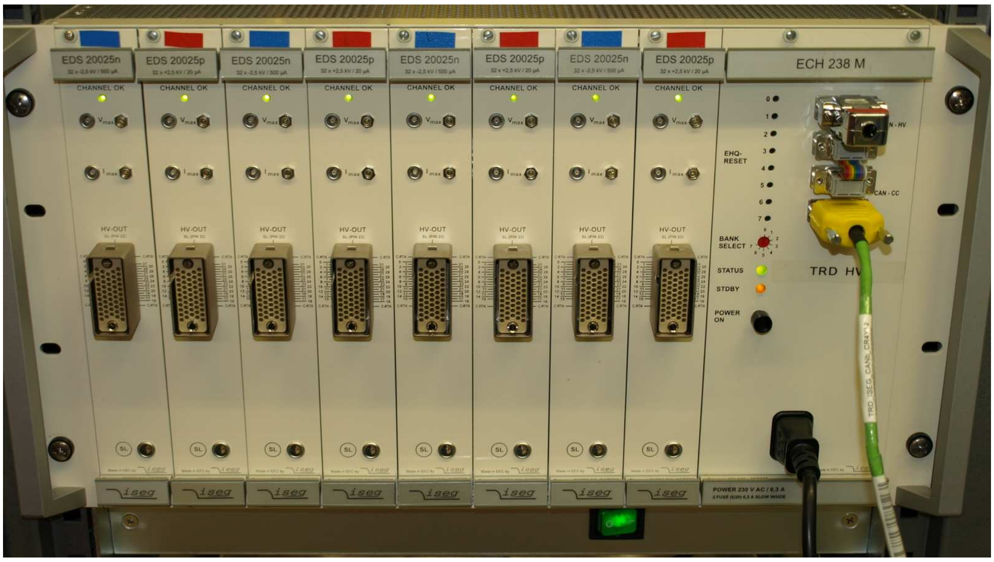

Figure 5.2: Photo of a high voltage crate with eight 32 channel modules.

According to the above requirements, the ISEG modules of our choice are the "EDS 20 025n_504" for drift and the "EDS 20 025p_203" for anode high voltage, for technical details see Table 5.1. These modules are operated in a ISEG ECH 238 M crate, which can take up to 8 EDS modules, as shown in Figure 5.2.

The EDS module offers 32 channels of one polarity, 2 channels are kept as spares, 30 outputs are directly connected through a multi-conductor cable to the HV fan-out box on the A-side end cap of the super module. The cable length between the HV racks in CR4 and the super modules inside the L3 magnet is approximately 80 meters. Thirty conductors are used to feed voltage to the 30 chambers, the current flows back through

ISEG	drift module EDS 20 025n_504	anode module EDS 20 025p_203
channels	32	32
U_{max} [V]	-2500	$+2500$
I_{max} [μA]	500	20
$\dot{U}_{ramp}$ [V/s]	1 – 500	1 – 500
U_{set} resolution [mV]	50	50
U_{meas} resolution [mV]	5	5
I_{meas} resolution [nA]	10	0.4
I trip response time [ms]	100	100
ripple max. U_{pp} [mV]	< 20	< 10
stability	$< 5 * 10^{-5}$	$< 5 * 10^{-5}$

Table 5.1: Specifications of the ISEG high voltage modules for drift and anode voltage. 36 of those modules offer the 1080 channels required for the operation of the TRD. A pair of positive and negative modules per crate provides HV power for the 30 detector chambers of a TRD super module.

4 common return lines. Not only all channels of a module have common ground, also all modules mounted in the same crate share the same ground. This common ground of the modules can float up to 20V at maximum with respect to the crate power input ground.

A pair of a negative and a positive EDS modules provides all HV power for the 30 detector chambers of one TRD super module. The grounding point of the TRD detector is by definition each individual super module, all LV and HV power supplies have to be floating. As long as only one pair of HV modules is operated in a crate, the ground separation of the TRD sectors is preserved. With more than a single pair of modules in a crate, the ground potentials of the corresponding sectors would be merged, which might result in a higher noise level.

In order not to mix ground connections between different super modules, only 2 EDS modules (1 drift + 1 anode) are mounted in each crate, connecting to the same destination sector, see Figure 5.8. For the full TRD, there will be 36 modules in 18 crates, as drawn in Figure 5.1. Two worker nodes are remotely controlling the crates in groups of 3 through 6 CAN busses arranged in star topology.

5.3 HV in the super module and chambers

A pair of multi-conductor cables, one for each polarity, connects to two high voltage fan-out boxes mounted on the A-side end cap of the TRD super modules. From these fan-out boxes two coaxial high-voltage cables are routed to each TRD detector, where they end in a small high voltage filter box (see Figure 5.3) mounted alongside the TRD chambers. The filter box acts as a low pass filter, reducing pick-up noise especially for the sensitive anode wire grid. It offers a two stage RC-filter for up to 8 anode segments and a single stage RC-filter for the voltage divider in the field cage of the drift volume.

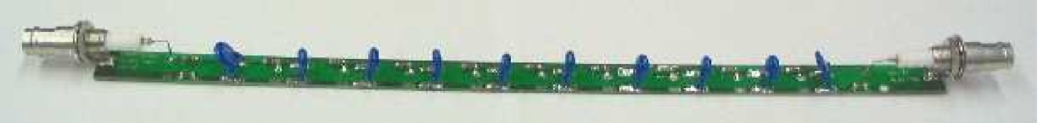

Figure 5.3: Photo of a high voltage filter box. It offers a two stage low-pass filter for up to 8 anode segments and a single stage low-pass filter for the voltage divider in the drift field cage.

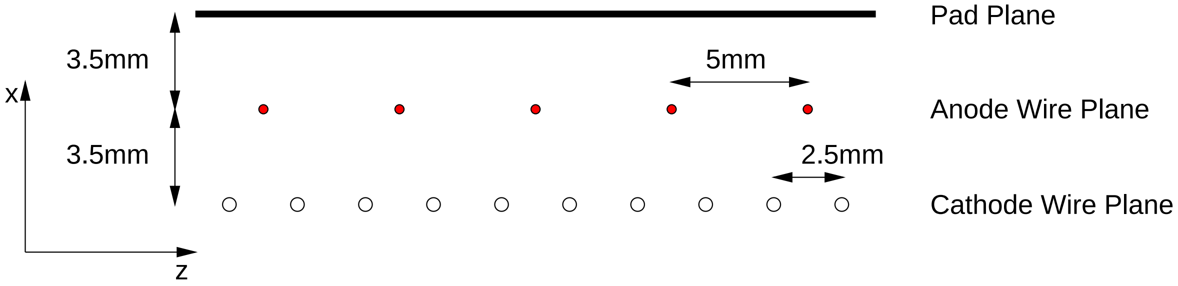

Figure 5.4: The wire geometry of the TRD readout chambers.

Cables from the outlets of the HV filter box are routed inside the detector chamber, where they connect to the anode wire grid or to the resistor chain of the drift volume.

The anode wire grid is subdivided into 6 or 8 segments (depending on the number of pad rows in the chamber), each segment covering the area of 2 adjacent rows of pads. This segmentation minimizes possible discharges inside the chamber and reduces the charge-up time of the anode wires. The anode system is an open system, there is no direct return line to the supplies. All anode current inside the chamber (Figure 5.4) travels through the avalanche ionized gas mixture either to the cathode wire grid or the drift electrode, which are both at ground potential, or to the pad plane, which in turn is connected to the readout electronics. At the nominal gas gain of 10^4 an anode current of 1 μA/m^2 is expected for Pb–Pb operation.

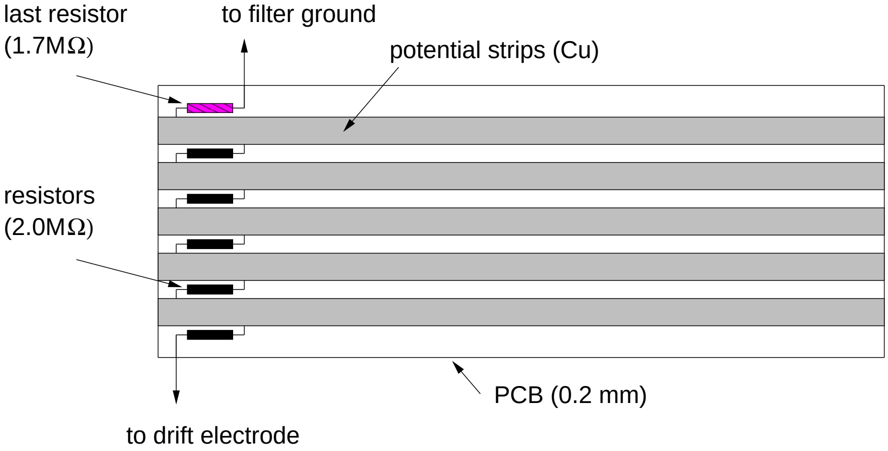

Figure 5.5: The resistor chain of the field cage inside the chamber, ($R_{total} = 11.7\text{M}\Omega$).

The drift cable is soldered to the drift electrode on the inner surface of the radiator. From there, the current flows through the 11.7 MΩ voltage divider chain of the field cage, see Figure 5.5, and returns to the ground of the filter box. The electrostatic matching of the drift region to the amplification region is achieved by proper choice of the last resistor of the voltage divider chain. With only 1.7±1% MΩ, compared to 2.0±1% MΩ for the other resistors, it compensates for the shift of the effective ground plane away from the cathode wire grid into the drift region. The drift current compensates for the ion back-drift from the amplification region to the drift electrode. Together with the 1.01 MΩ from the RC-filter the resistors in the drift loop sum up to 12.71 MΩ. The resulting drift current amounts to 165 μA at 2100 V.

5.4 HV calibration for operation

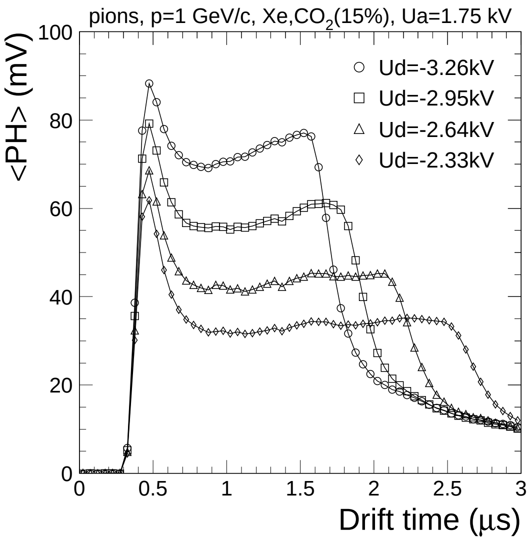

Figure 5.6: Typical spectra of average pulse height and drift time for different drift voltages.

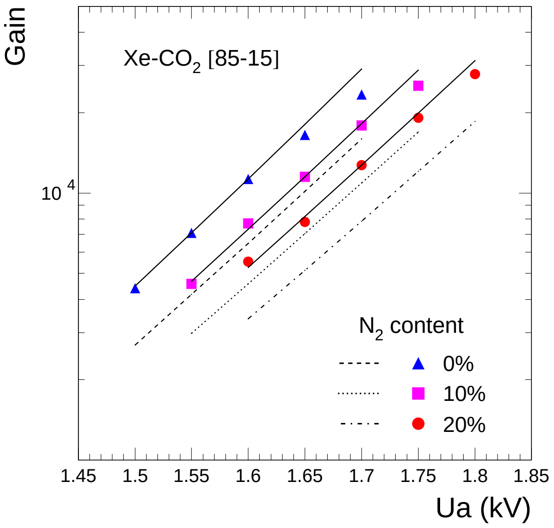

Figure 5.7: The gas gain increases exponentially as function of anode voltage, accumulation of N_2 reduces the gain.

The calibration of the high voltage for TRD chamber operation is an iterative process. First, the gas composition in the detector needs to be stable. Initially, default values are applied to the anode and drift HV settings. In a next step one takes a few events of data to generate the average pulse height spectrum and determines the average drift time. Then, the drift voltage is tuned such that the signal spreads over 20 time bins (2 μs), see Figure 5.6. Finally, the anode high voltage is adjusted such that the plateau for pions settles between 80 to 100 ADC counts. As visible in Figure 5.7, the gain depends exponentially on the anode voltage. This calibration procedure needs to be automated for a standalone operation of the detector.

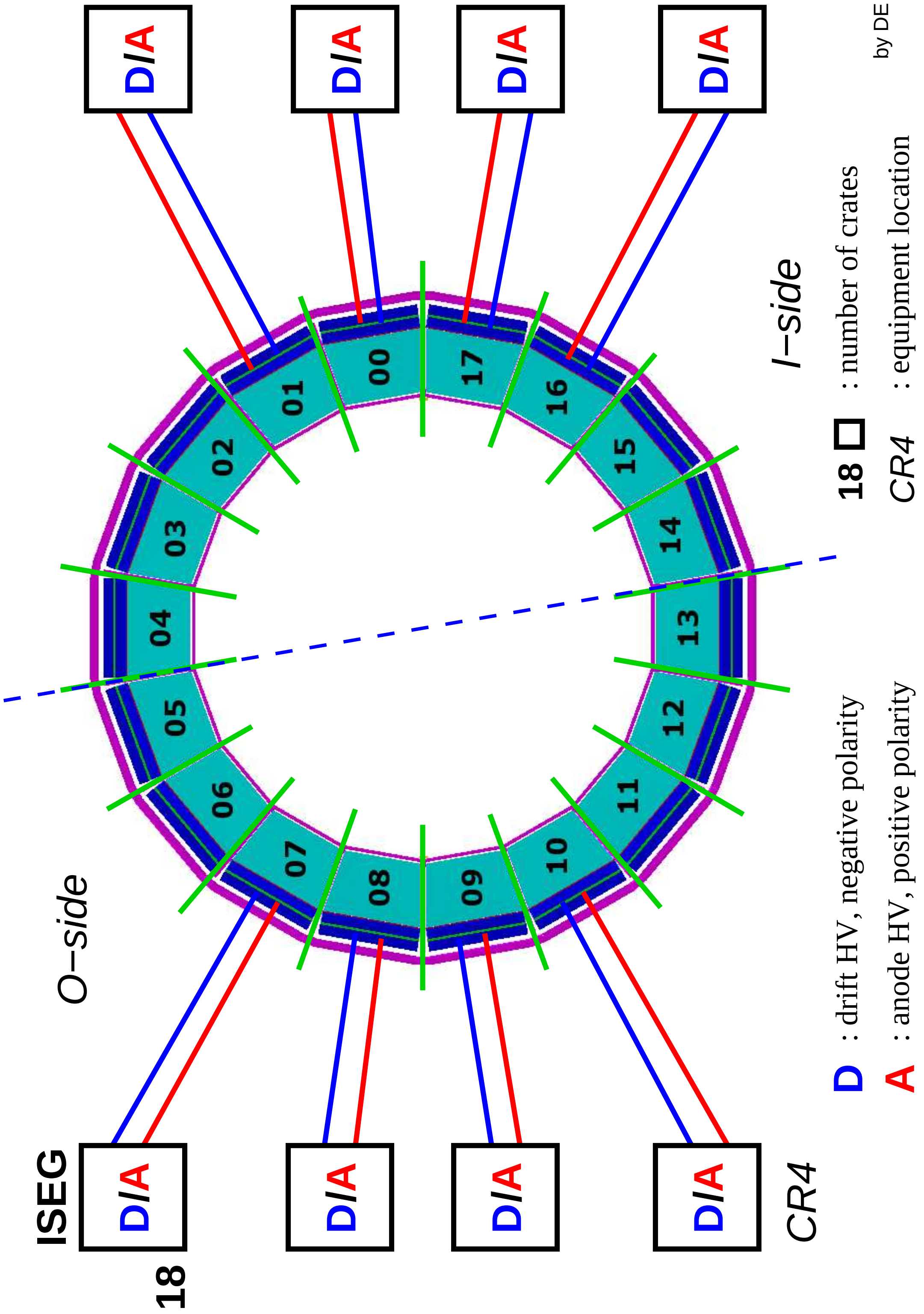

Figure 5.8: Topology of the TRD high voltage system, each sector is powered by its own crate. Each crate holds a negative and a positive 32 channel HV module for drift and anode HV respectively.

Chapter 6

The HV distribution system

6.1 Preface

The high voltage system described in Chapter 5 was adopted during the year 2007. Before, we had a different approach, the so-called high voltage distribution system (HVDS), which will be summarised in this chapter. The HVDS was only partially built: 4 secondary crates are available, which could supply 6 TRD sectors. As of February 2009, the decision is still pending to operate or not the HVDS, in a mixed setup together with the high voltage system for the remaining 12 sectors.

6.2 Requirements for the HVD system

Each of the 540 TRD detector chambers has 2 individual high voltage inputs : a negative voltage for the drift field and a positive voltage for the amplification region. In order to create the necessary drift field, a potential of -2.1 kV is needed. For the anodes the required potential is around $+1.6$ kV in order to reach sufficient gas gain. The ripple of each channel needs to be smaller than 50 mV peak to peak and the stability better than 0.1% over 24 hours.

6.3 The HVD system layout

A two-stage architecture was chosen for the HV distribution system, in order to provide the 1080 HV channels to the detector. The system is sketched in Figure 6.3, page 79. At first stage, a commercial ISEG high voltage system provides 192 channels of primary HV power, with sufficient current for the full TRD detector. The second stage consists of self-made HV distribution crates, which fan-out each primary high voltage channel to 6 secondary outputs. The HVD crates allow to monitor and control the 1080 channels individually with the required sensitivity for detector operation. Two types of crates are used in the HVDS, one for each polarity, they are built by the University of Athens. Both stages of the HVD system, primary and secondary, are controlled through PVSS, the process control system commonly used at CERN. The connection of the HVD crates to the TRD super modules is done via the standard multi-conductor cable interface, identical to the connection of the ISEG EDS modules.

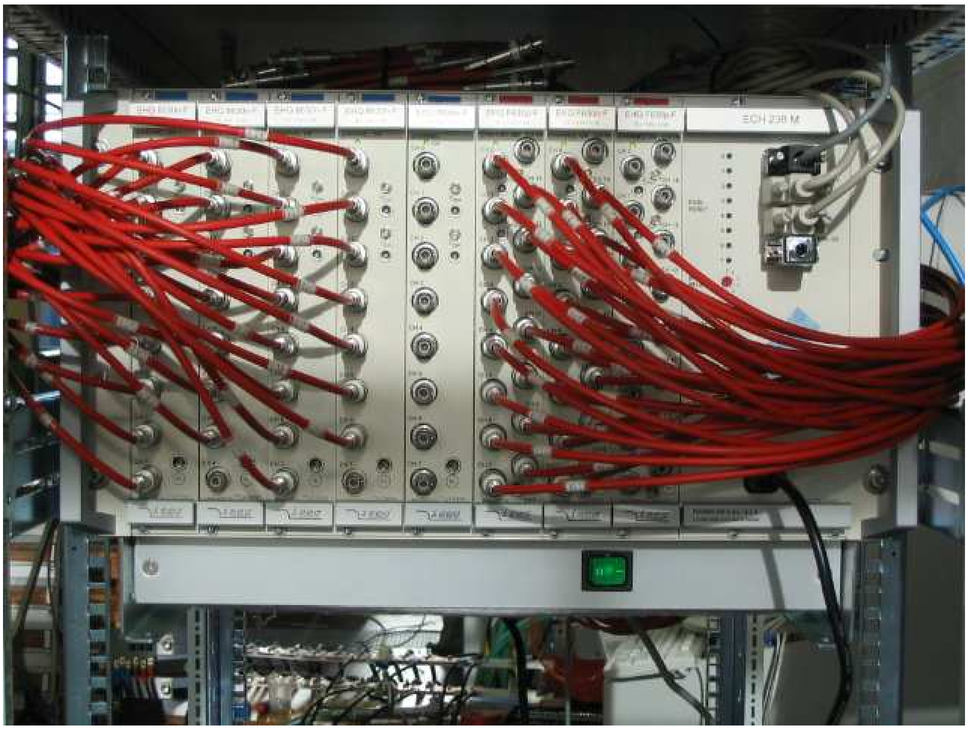

Figure 6.1: Picture of a primary ISEG high voltage power crate for the HVDS, supplying 64 channels to the HVD crates.

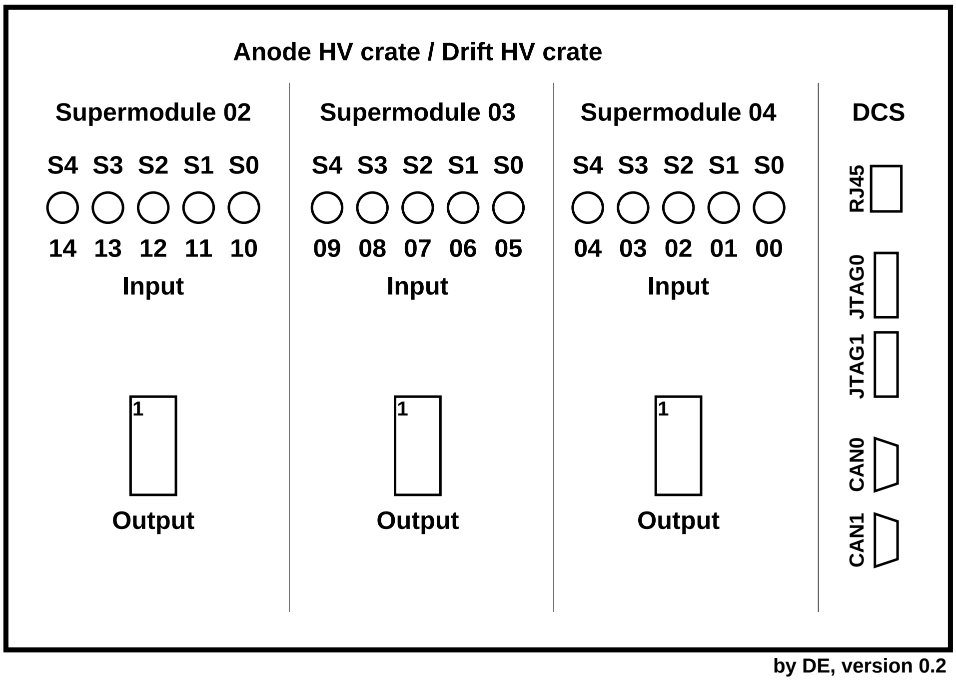

Figure 6.2: Schematic front view of a HV distribution crate. It has 15 primary HV inputs, and supplies one polarity of high voltage to 3 super modules.

ISEG	EHQ 8630n_305-F drift module	EHQ F630p_205-F anode module
number of output channels	8	16
U_{max} [V]	-3000	$+3000$
I_{max} [μA]	3000	2000
$\dot{U}_{ramp}$ [V/s]	0 – 600	0 – 600
U_{set} resolution [mV]	60	60
I_{set} resolution [nA]	60	40
ripple max. U_{pp} [mV]	< 10	< 10
U_{meas} resolution [mV]	< 30	< 30
I_{meas} resolution [nA]	< 30	< 20

Table 6.1: Parameters of the two types of ISEG high voltage modules used in the HVD system. The primary HV crates offer a total of 96 negative and 96 positive channels.

HVDS	drift card	anode card
number of input channels	1	1
number of output channels	6	6
U range [V]	-1450 to -2500	$+900$ to $+1900$
I_{max} [μA]	230	7
$\dot{U}_{ramp\ up}$ [V/s]	30	30
$\dot{U}_{ramp\ down}$ [V/s]	100	100
ripple max. U_{pp} [mV]	< 30	< 30
U sampling rate [Hz]	10	10
I_{meas} resolution	$< 5\%$	$< 2\%$
response time [ms]	< 50	< 50

Table 6.2: Parameters of the HVD cards. 5 negative and 5 positive cards are needed to operate one TRD super module. 15 cards of the same polarity are grouped into one HVD crate providing HV power for 3 super modules.

6.4 The primary ISEG HV power supplies

The primary HV power is generated in 3 ISEG crates of type ECH 238 M equipped with 6 modules of 2 different types, see Figure 6.1 and Table 6.1 for technical parameters :

- the negative drift voltage is supplied by EHQ 8630n modules
- the positive anode voltage is supplied by EHQ F630p modules

Each of the primary crates provides enough high voltage power to operate 6 TRD super modules. They are located in counting room 4 (CR4), in the shaft to the ALICE cavern, allowing operation in a zone free of magnetic stray fields. The crates are remotely controlled via CAN bus. The primary HV system uses 180 SHV cables to connect to the HVD crates in the ALICE cavern, located in proximity of the L3 magnet.

6.5 The secondary HV distribution crates

The main task of the HVD crates is to redistribute and control the incoming 180 channels from the primary ISEG system to 1080 output channels. In addition it allows for enhanced sensitivity in the measurement of anode currents. It is located in the I- and O-racks of the ALICE cavern on the A-side of the L3 magnet. The HVDS divides into 12 crates, spread over 4 racks. Each of the crates feeds high voltage of one polarity to 3 TRD super modules. A HVD crate (see Figure 6.2) consists of 15 HV-cards, each card converts 1 input channel to 6 output channels, Table 6.2 presents technical parameters. The output channels of the HVD crates can be individually configured and controlled. In each HVD crate a single DCS board controls the HV-cards through CAN. The CAN buses of two neighbouring HVD crates are interconnected to a single bus, such that two DCS boards are redundantly present on each CAN segment. As the HVD crates are installed in the ALICE cavern, they have to withstand magnetic fields up to 80 Gauss. The HVD crates are connected to the TRD super modules via multi-wire high voltage cables. Each super module has 2 such cables, one for each polarity. The 6 output channels of a HV-card map to a stack of 6 TRD chambers in the super module.

6.6 Controls of a mixed high voltage setup

The control system for a mixed high voltage setup are sketched in Figure 6.4. The mixed system would consist of 12 sectors directly powered from EDS modules and another 6 sectors powered through the HVD system. As the 2 subsystems rely on completely different hardware emphasis was put on a complete separation of the control systems. The top level interface, however, should be totally transparent for the operator, independent of the underlying hardware.

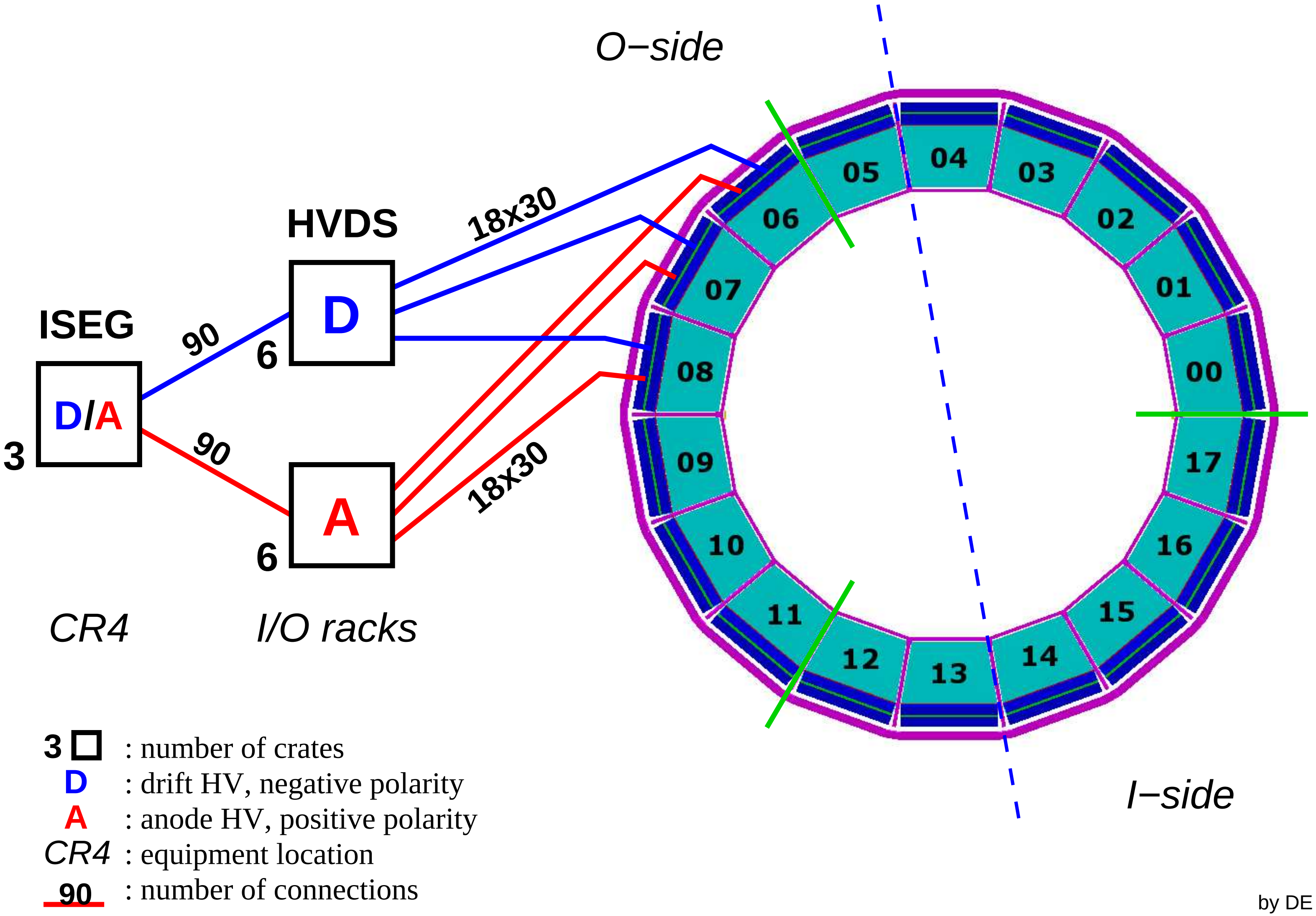

Figure 6.3: Topology of the high voltage distribution system, only $\frac{1}{6}$ of the connections between the HVDS crates and the TRD super modules are drawn.

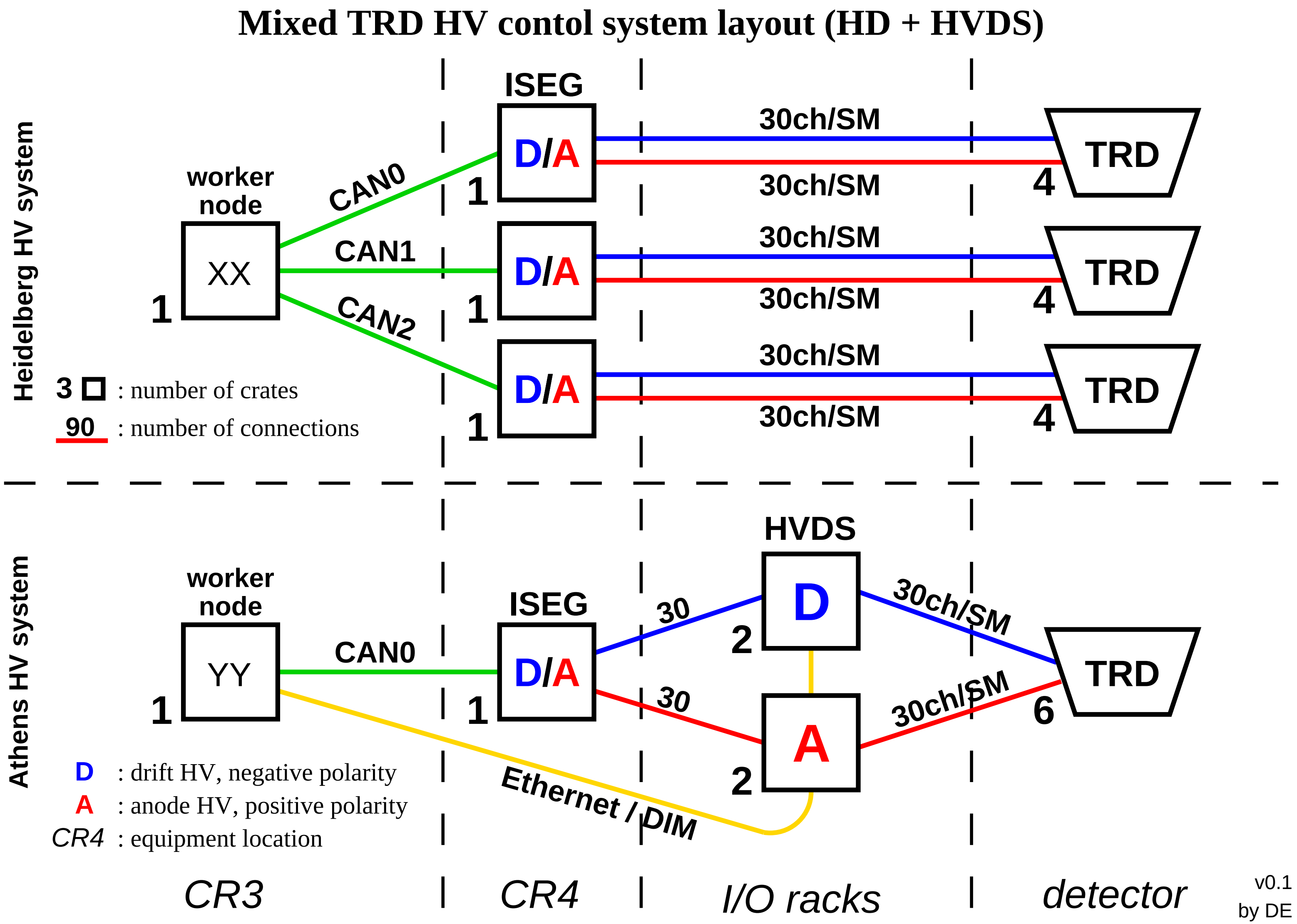

Figure 6.4: Layout of the controls for a mixed TRD high voltage and HVD system.

Chapter 7

Ethernet Network

The TRD detector and its infrastructure in the pit rely heavily on network communication, more than 600 Ethernet nodes are in use for the full system. The setup consists out of two major subsystems :

The low voltage infrastructure has 89 Ethernet interfaces, one connection per power supply. They are used to remotely monitor and control the low voltage power system.

569 nodes are used for configuration and control of the TRD detector itself and the major part of the infrastructure systems. A small, single board computer, the Detector Control System (DCS) board has been developed for this purpose. Each TRD chamber is equipped with one DCS board, they amount to 540 (with the hole in front of PHOS only 522) Ethernet connections for the TRD super modules. The DCS boards in the TRD infrastructure sum up to 29 nodes : 19 DCS boards are built into the Global Tacking Unit (GTU), 4 DCS boards in the Power Control Unit (PCU) and 6 more are controlling the pre-trigger Control Boxes (2 in each CBA, CBC and CBTOF). Should the full High Voltage Distribution System (HVDS) be realised, it would add an extra 12 DCS boards.

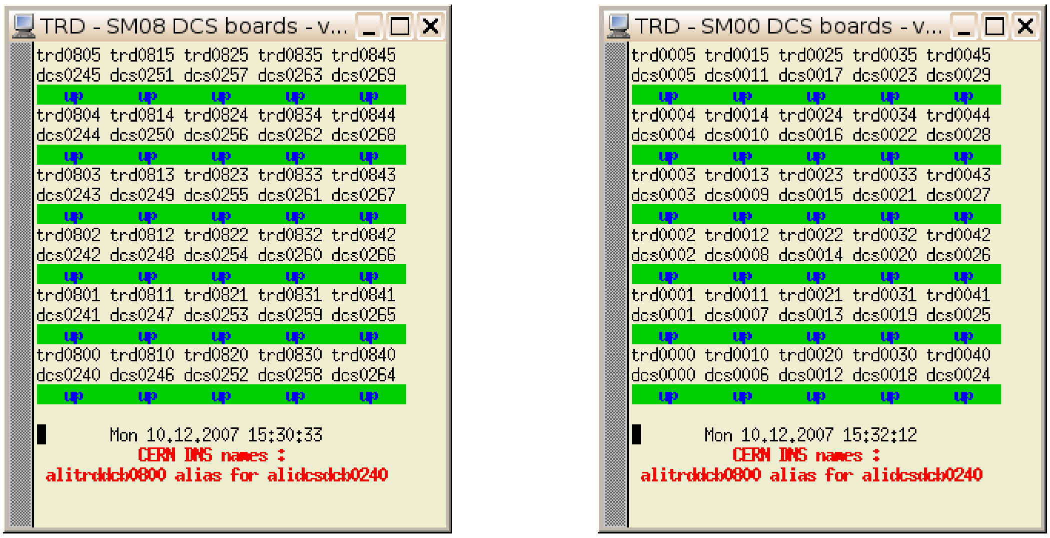

```
trd0805 trd0815 trd0825 trd0835 trd0845
dcs0245 dcs0251 dcs0257 dcs0263 dcs0269
   up      up      up      up      up
trd0804 trd0814 trd0824 trd0834 trd0844
dcs0244 dcs0250 dcs0256 dcs0262 dcs0268
   up      up      up      up      up
trd0803 trd0813 trd0823 trd0833 trd0843
dcs0243 dcs0249 dcs0255 dcs0261 dcs0267
   up      up      up      up      up
trd0802 trd0812 trd0822 trd0832 trd0842
dcs0242 dcs0248 dcs0254 dcs0260 dcs0266
   up      up      up      up      up
trd0801 trd0811 trd0821 trd0831 trd0841
dcs0241 dcs0247 dcs0253 dcs0259 dcs0265
   up      up      up      up      up
trd0800 trd0810 trd0820 trd0830 trd0840
dcs0240 dcs0246 dcs0252 dcs0258 dcs0264
   up      up      up      up      up

        Mon 10.12.2007 15:30:33
            CERN DNS names :
 alitrddcb0800 alias for alidcsdcb0240
```

```
trd0005 trd0015 trd0025 trd0035 trd0045
dcs0005 dcs0011 dcs0017 dcs0023 dcs0029
   up      up      up      up      up
trd0004 trd0014 trd0024 trd0034 trd0044
dcs0004 dcs0010 dcs0016 dcs0022 dcs0028
   up      up      up      up      up
trd0003 trd0013 trd0023 trd0033 trd0043
dcs0003 dcs0009 dcs0015 dcs0021 dcs0027
   up      up      up      up      up
trd0002 trd0012 trd0022 trd0032 trd0042
dcs0002 dcs0008 dcs0014 dcs0020 dcs0026
   up      up      up      up      up
trd0001 trd0011 trd0021 trd0031 trd0041
dcs0001 dcs0007 dcs0013 dcs0019 dcs0025
   up      up      up      up      up
trd0000 trd0010 trd0020 trd0030 trd0040
dcs0000 dcs0006 dcs0012 dcs0018 dcs0024
   up      up      up      up      up

        Mon 10.12.2007 15:32:12
            CERN DNS names :
 alitrddcb0800 alias for alidcsdcb0240
```

Figure 7.1: Ping monitors for DCS boards in sectors 08 and 00.

Two star points provide the Ethernet infrastructure in the pit. Connections to the

A-side of the cavern (I and O racks up to 24) are fed from star point 2222-P5, a rack located in the main access shaft on level 5, next to the gas distribution system. The C-side of the cavern (I and O racks with numbers above 25) is served by star point 2227-0 in the LHC service tunnel. The low voltage power supplies have point-to-point connections to the star points. Four class-C subnets are used to address these power supplies, depending on their rack location.

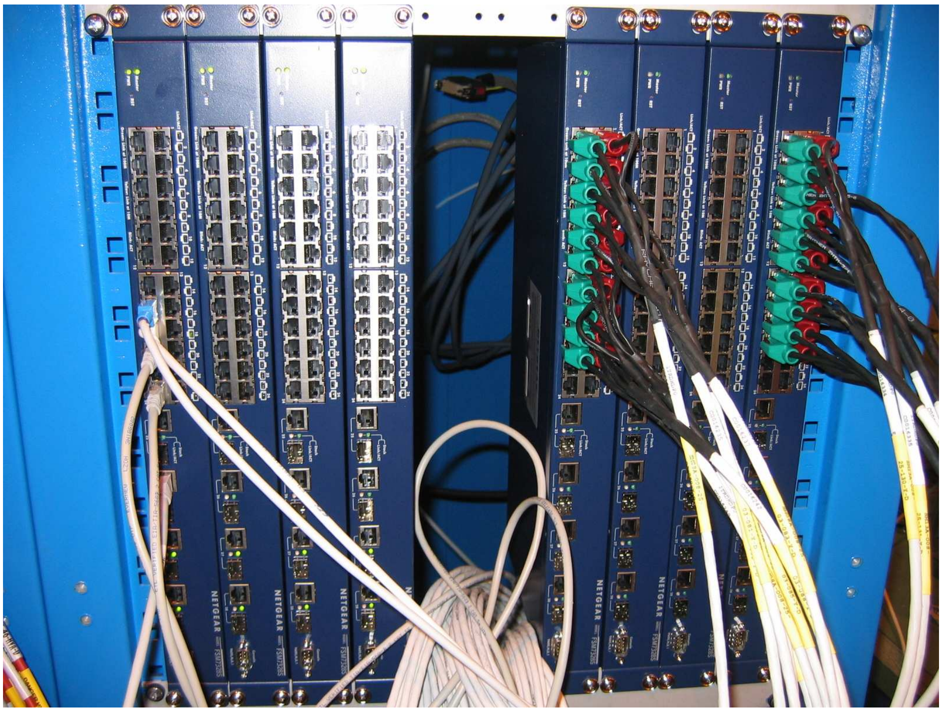

Figure 7.2: Photo of Ethernet switches in rack O08 during installation. They are used provide up-links to DCS boards from the 3 first stacks on the A-side of the super modules. Here, connections for 2 super modules are plugged in.

A total of 31 TRD-owned 24-port Netgear switches is installed across 5 racks in the cavern, see Figure 7.2. They have individual up-links to the star points and act as fan-outs for the 10 MBit DCS board up-links. A big issue during cable installation was the restricted space available in the chicanes leading into the L3 magnet. Therefore the number of Ethernet connections had to be balanced between the A- and C-side of the magnet. It was decided to route 60%/40% of the connections through the A-/C-side. For each super module, the DCS boards of the first 3 stacks (S0–S2) connect to switches on the A-side of the L3 magnet, while the other 2 stacks (S3, S4) are linked to switches in the C-area.

Some devices in the TRD infrastructure are equipped with two or more DCS boards for redundancy, e.g. the PCU or the pre-trigger crates. Network connections to these devices are done to switches located in different racks. This allows to keep the connectivity to a device, even if a power failure occurs in one of the racks.

Chapter 8

Beam tests and data acquisition

During the prototyping and construction phase of the TRD several beam tests took place to validate the detector design. Two beam tests were conducted at the CERN PS accelerator using full sized TRD chambers from the series production. The following sections will highlight a few aspects of those tests in the context of this thesis.

8.1 Beam test 2004

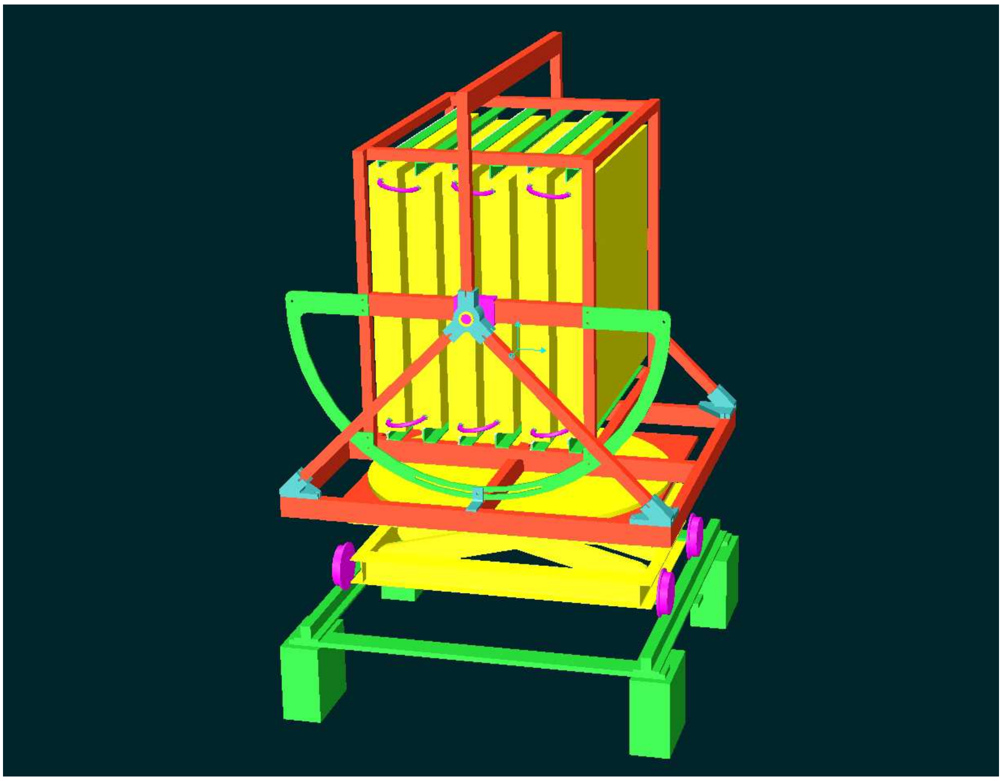

Figure 8.1: Drawing of the test stack especially built for the beam test 2004. It consists of 6 full size chambers. The setup can be horizontally and vertically displaced. Also rotations around the horizontal ϕ- and the vertical θ-axis can be performed.

In autumn 2004 a stack with the first 6 full-size TRD chambers from series production was tested in beam at the CERN PS accelerator. All the conception, planning and organisation of this beam test was part of this thesis work. A mechanical structure was specially constructed to support and position the chambers, a drawing is presented in Figure 8.1. It allows horizontal and vertical displacements of the chambers perpendicular to the beam axis. The device can also be rotated around the horizontal ϕ- and the vertical θ-axis. The stack can be placed into any orientation with respect to the incoming beam which will be covered by TRD chambers installed in ALICE with respect to particles originating from the interaction vertex. Figure 8.3 shows the setup installed in the T9 beam line, providing particles in a momentum range of 1 to 10 GeV.

The production of readout boards was slowly starting up a few weeks prior to the beam time. Therefore the chambers were only partially equipped with the available 8 ROB prototypes. Their positions were carefully selected across 36 possible locations to allow for wide angular scans. The boards were read out with a custom system. A two layer binary tree of 3 single MCMs collected the data from the 8 ROBs, see Figure 8.2. The root MCM was connected via LVDS to an ACEX card which was plugged into a computer forwarding the data into the DAQ system through a DDL. As a water cooling system was not yet available, the electronics was cooled with air.

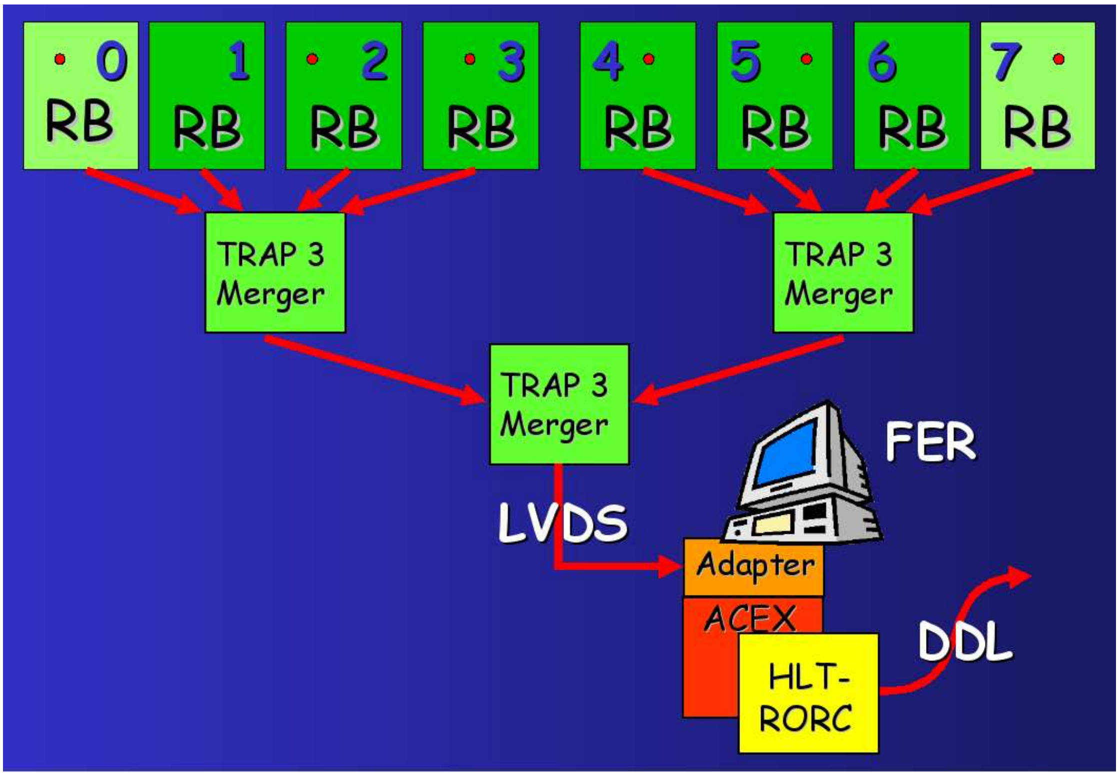

Figure 8.2: MCM readout tree used in the beam test 2004.

The layout of the TRD beam line is schematically shown in Figure 8.5. In addition to the device under test a set of monitoring detectors is used to trigger, track and identify the particles. First, there are three scintillators along the beam line used as trigger detectors. Two silicon strip detectors provide an external position reference for the particle tracks. Finally, we used Cherenkov detectors and a lead-glass calorimeter

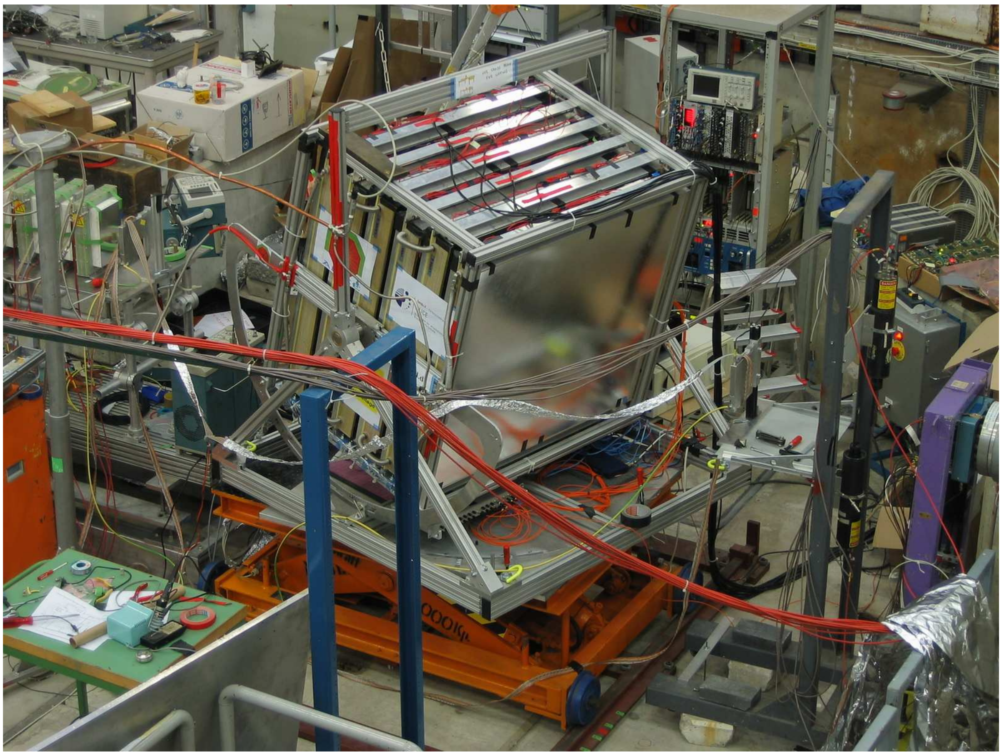

Figure 8.3: The TRD beam test setup in 2004: The stack of 6 chambers partially equipped with electronics was under test in the T9 beam line at the CERN PS.

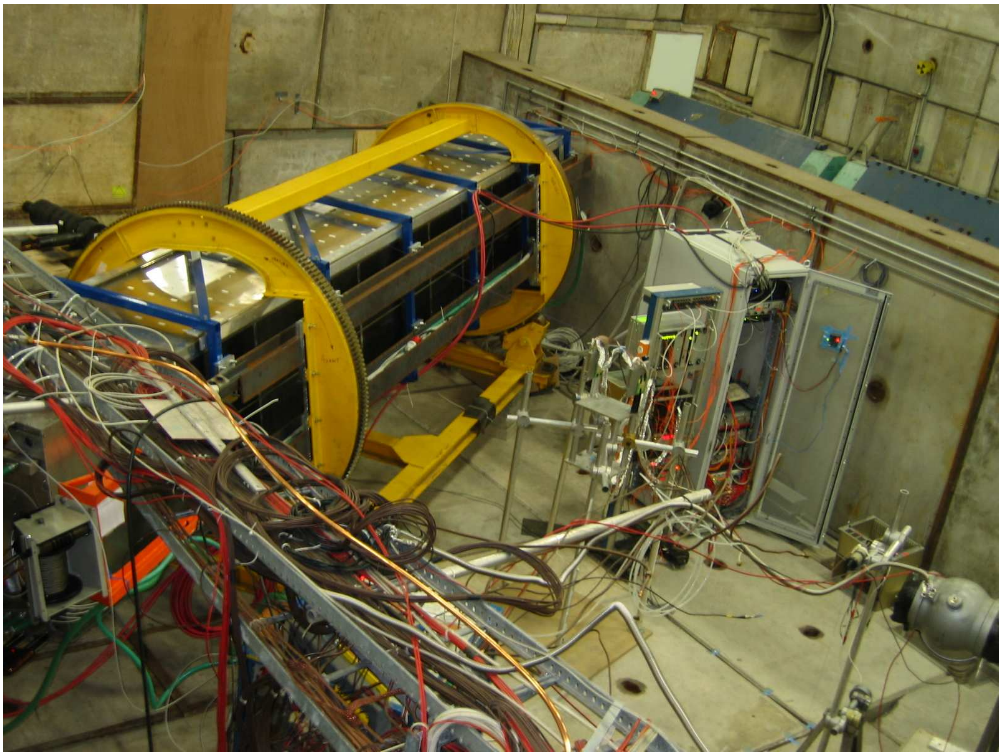

Figure 8.4: The TRD beam test setup in 2007: Super module III was installed in the T10 beam line at the CERN PS. The beam passed through the chambers of stack 1.

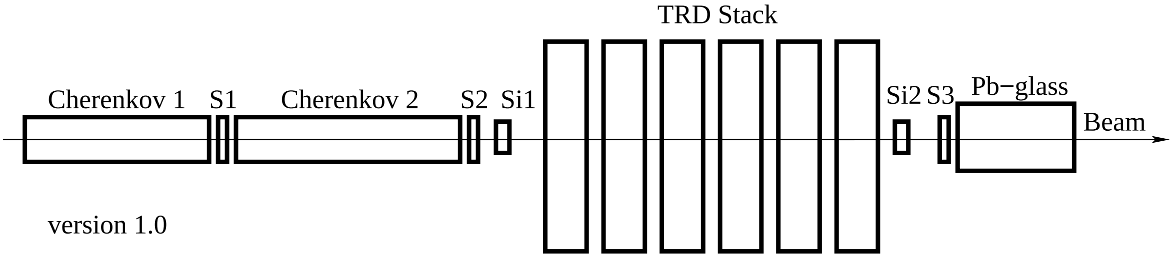

Figure 8.5: Beam line setup schematics for the beam test 2004.

for particle identification. The data recorded by the monitoring detectors is used offline to reconstruct the true particle ID in the TRD performance analysis. An online event display of a track passing through the 6 chambers of the stack is presented in Figure 8.11.

The data acquisition system for this beam test was also developed in the framework of this thesis. Details will be presented in section 8.5, based on the further evolved DAQ system of the beam test 2007.

8.2 Beam test 2007

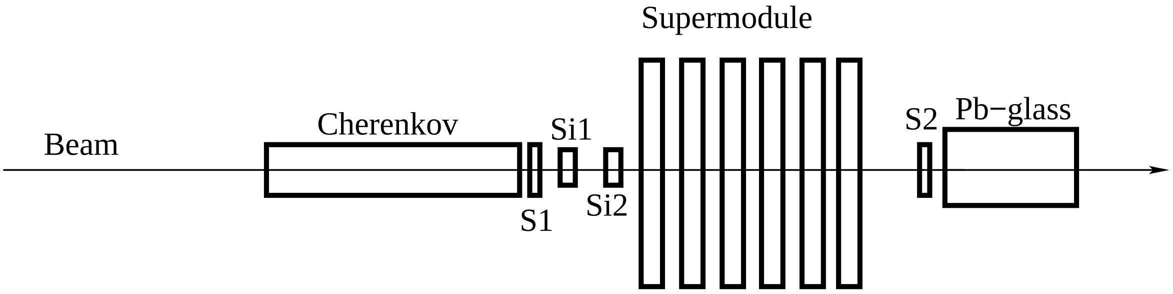

Figure 8.6: Beam line setup schematics for the beam test 2007.

During the year 2007 the series integration of TRD super modules started up. For the beam campaign in autumn 2007 the TRD super module III was installed in the T10 beam line at the CERN PS accelerator, see Figure 8.4. The beam line setup (Figure 8.6) was almost identical to the one in 2004, except that for space reasons only one Cherenkov detector was used and the super module replaced the stack. Particles with a momentum range of 1 to 6 GeV are available in the T10 beam line. A HLT online event display of three tracks passing through the stack of chambers is shown in Figure 8.12. Due to space constraints the super module could not be displaced with respect to the beam. It was installed such that the beam passed through stack number one at $\theta = 16°$ and $\phi = 10°$. The 4 other stacks were powered off in order to reduce the low voltage power consumption and to decrease the data volume by 80%. The super module was equipped with an Optical Readout Interface (ORI) and a GTU unit served as front-end to the data acquisition system. The later was an upgraded and extended version based on the DAQ system used in 2004.

8.3 Discovery of gas leaks in the super modules

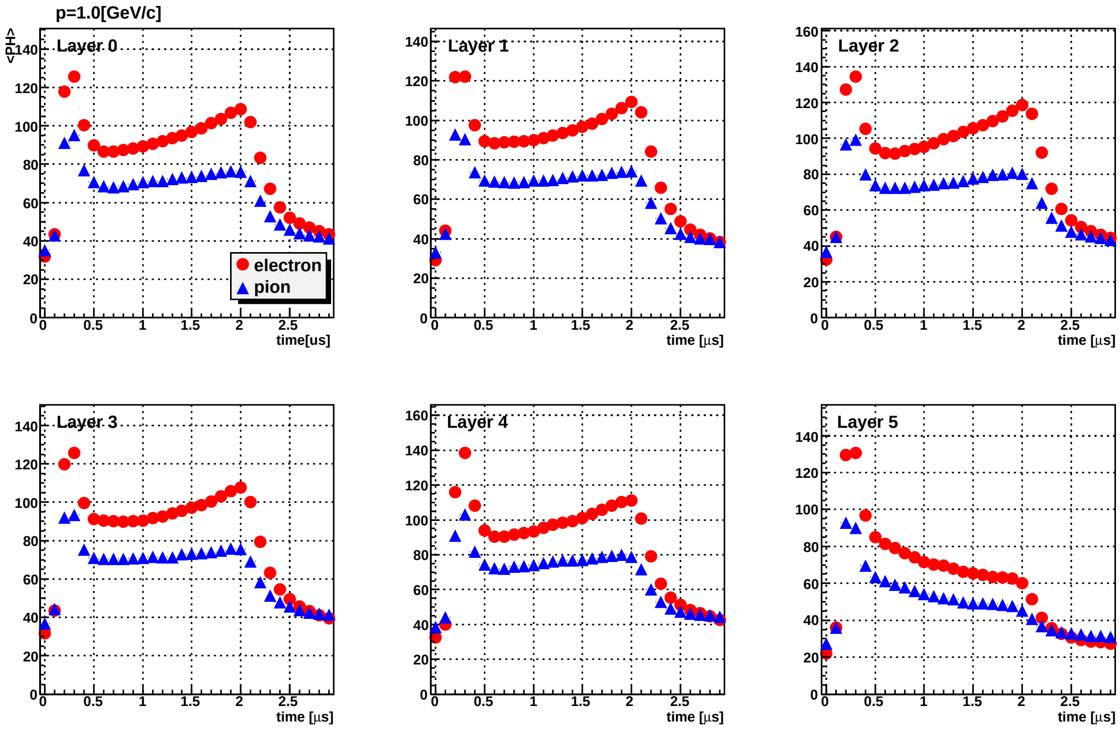

Figure 8.7: Average pulse height for the 6 chambers of the 2007 beam test, from [40]. The chamber in layer 5 (bottom right) shows an attenuation of the signals, which is due to electron attachment caused by contamination of the counting gas with oxygen.

An important discovery of the beam test 2007 was the detection of a large gas leak in the super module. After flushing with the Xe/CO_2 gas mixture the detector was first operated at 0.4 mbar over-pressure, where the average pulse height distributions looked as expected. In order to reduce the gas consumption, it was then decided to reduce the over-pressure level. Within only one hour after switching to 0,0 mbar (no overpressure) the pulse height distribution deteriorated in the chamber of layer 5, as visible in Figure 8.7. The signal breakdown at late drift times is caused by electron capture due to O_2 contamination of the gas mixture. The leak was located in proximity, upstream of the suspicious chamber, with an estimated huge leak rate of 30 bar l/h at 0.4 mbar overpressure, equivalent to a leak conductance of 75000 mbar l/h, (8.1).

$$\mathrm{leak}_{rate}(mbar\frac{l}{h}) = \mathrm{leak}_{conductance}(\frac{l}{h}) \times \Delta \mathrm{p}(mbar) \tag{8.1}$$

Prior to the 2007 beam test, the leak tightness test of TRD chambers was sensitive to diffusive leaks only. The test was a measurement of the oxygen residual in the gas at overpressure. The type of viscous leaks observed at the beamtime went unnoticed, as even with no oxygen penetrating into the chamber, the counting gas mixture could still escape from the chamber volume, due to the overpressure. The operation of the TRD at the observed leak rate would not have been affordable, as the quantity of xenon lost would have been far too expensive. As a consequence the leak testing procedure was altered, monitoring the oxygen contamination in the chambers at under-pressure.

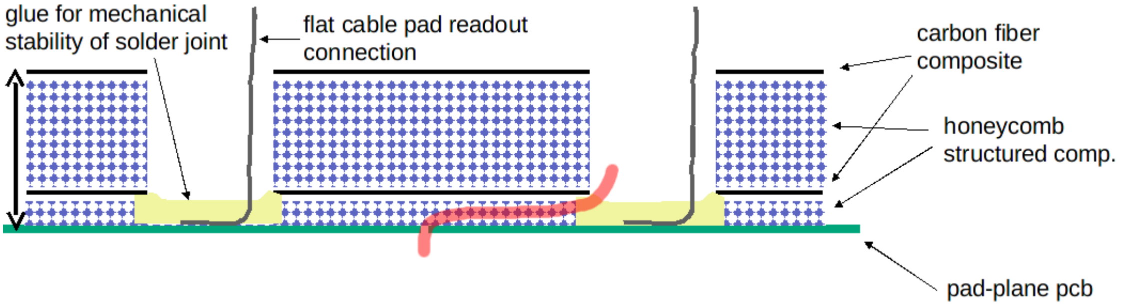

Figure 8.8: Gas from inside the active volume of the TRD chambers can escape along the red path through the backpanel composite structure to the outside, from [41].

At the time of the beam test 2007, 2 super modules were already installed in the ALICE cavern, 2 more super modules integrated and another 270 TRD chambers produced. This total batch of 390 TRD chambers had to be re-inspected and patched for leaks, which took a considerable amount of time and man power. The majority of the leaks were located at the joint between the pad plane and the back-panel of the chambers, as indicated in Figure 8.8. The amount of glue applied in that area was too little to reliably seal the vias in the pad plane and the gaps between the pad plane pieces. With additional glue deposited around the flat cables in the feedthroughs of the back panel these leaks could be sealed. The average leak conductance of the chambers prior to the re-inspection was 236 l/h. It was reduced by two orders of magnitude to 1,73 l/h final leak conductance per chamber on average [42]. Today, monitoring of the leak rate is a routine task, already during the integration of the super modules.

The anticipated leak rate of 1 mbar l/h per chamber from the TDR could be undercut: The leak conductance for the entire TRD (540 chambers) is roughly 1000 l/h. During regular operation of the TRD, gas is supplied at 0.1 mbar overpressure [43], which results in a total leak rate of 100 mbar l/h for the entire detector.

8.4 The ALICE data acquisition system

Off-the-shelf computers operated in two different modes make up the core element of the ALICE DAQ system. The Local Data Concentrators (LDCs) collect data from the detector readout electronics through optical fibers, the so-called Detector Data Links (DDL). ALICE uses more than 500 DDLs, the TRD owns 18 DDLs. For each super module one DDL interconnects a GTU partition as TRD front-end to the DAQ LDCs. A DDL is capable to transport about 200 MB/s of data, it is plugged into a Read-Out Receiver Card (D-RORC) in the LDC. The D-RORCs host up to two DDLs and can be operated in a data forwarding mode, in which the incoming data on link 1 is copied as output stream to link 2. This mode is used to pipe raw data to the High Level Trigger (HLT) farm. Once an incoming event fragment is completely read out by the LDC, it is shipped by TCP/IP through a Gigabit Ethernet network to the Global Data Collectors (GDC), for event building. Upon completion of the event building the data

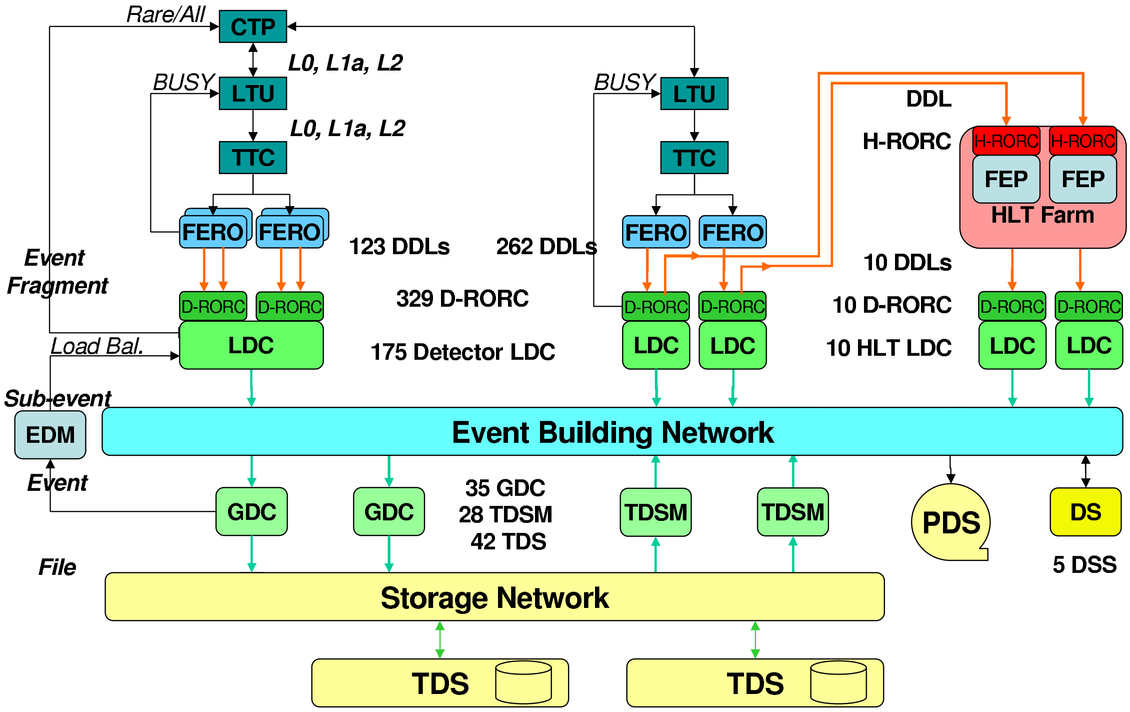

Figure 8.9: Schematical layout of the ALICE DAQ system, from [39].

is temporarily kept in the Transient Data Storage (TDS) system prior to being shipped continuously to Permanent Data Storage (PDS) in the remote CERN computing center. The ALICE DAQ system (Figure 8.9) has a readout capability of up to 40 GB/s, an aggregate event-building bandwidth above 2.5 GB/s and a large bandwidth to mass storage of 1.25 GB/s. The LDCs and the GDCs are controlled by the DATE (Data Acquisition and Test Environment) software package. DATE allows easy scalability, from a single PC system to the operation of the entire ALICE DAQ.

8.5 Data acquisition setup for beam tests

The TRD computing infrastructure used for beam tests is setup in a private network with a gateway connection to the outside world. As an advantage of this approach, all hosts can operate with identical configuration, whether during the setup phase in the lab or the data taking at the beam-line. The only interface which needs to be reconfigured when moving to a different site belongs to the gateway, this can be done within minutes. The data acquisition setup for the beam test in 2007 is sketched in Figure 8.10. It involved 3 PCs, two of them running DATE version 6.11 under SLC 4.6 and the third being the HLT satellite.

A first LDC (vmeldc) located in a VME crate was in charge of the monitoring detector readout. We used a CCT VP110, a VME form factor Pentium III with a local hard disk, for this task. It collected data from a set of VME modules :

- RCB 8047 CORBO – VME readout control board
- CAEN V550 – 2 channel 10-Bit ADC for multiplexed signals

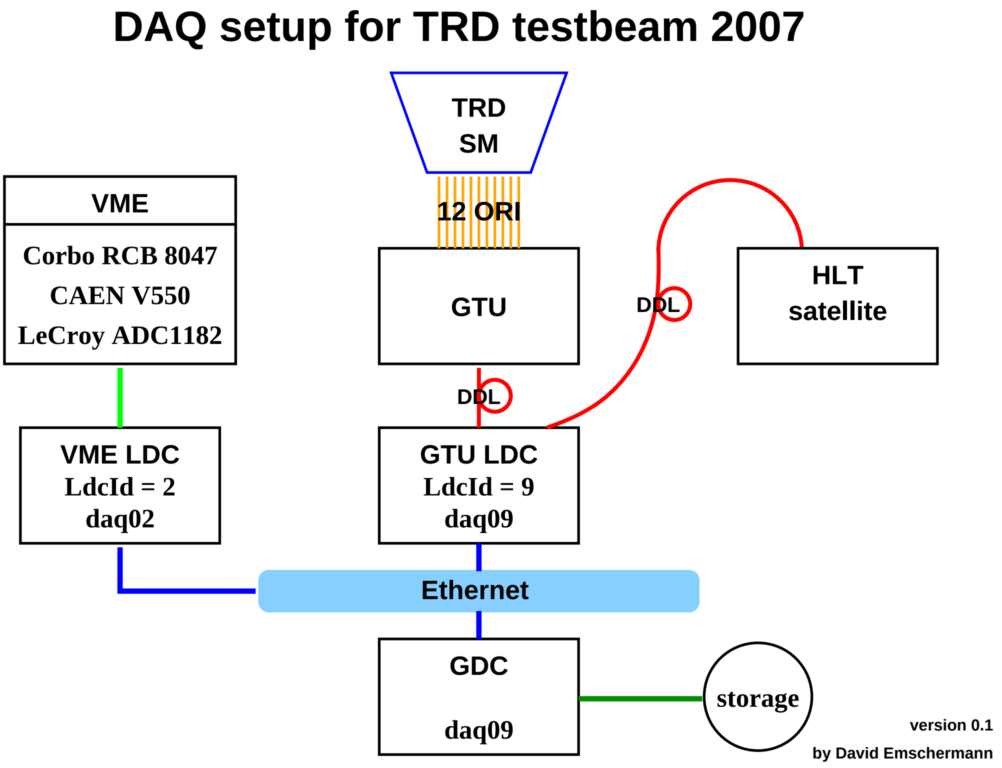

Figure 8.10: Data acquisition setup for the TRD 2007 beam test.

- LeCroy ADC 1182 – 8 channel 12-Bit ADC

The modules were processing trigger signals or reading the silicon strip, Cherenkov and lead-glass detectors. For each of those modules a dedicated hardware dependent DATE readout process had to be compiled on the LDC.

The 6 chambers in stack one were connected through 12 ORI fibers to a GTU partition serving as detector front-end to the DAQ system. The GTU was forwarding the raw data through one DDL into the second LDC (gtuldc). At this point the data stream from the super module could optionally be forked to the HLT satellite node through a second DDL.

The two LDCs then sent their recorded event fragments via (Gigabit-)Ethernet to a single GDC (trdgdc) performing event building and data storage. The roles of (gtuldc) LDC and (trdgdc) GDC were both implemented on the same PC, a Pentium 4 with a PCI-X mainboard. With spills lasting for half a second every 30 s, the data rate reached 170 events of zero suppressed data per spill. During the 2007 beam time 2.5 million events were recorded in more than 200 GB of data.

For the beam test in 2004 an online monitoring display was developed based on the MOOD package. The DATE data stream was interfaced to a monitoring host, which decoded and displayed the data in a ROOT interface. An event display showing tracklets in the six active MCMs is displayed in Figure 8.11. The MOOD package has been discontinued in the meantime. During the 2007 beam test the functionality of the TRD-HLT online event monitoring was successfully exercised.

A bit of effort is required to keep the event counters well synchronised throughout the beam-test setup. Trigger signals are optically or electrically distributed to the following four subcomponents : the MCMs in the super module, the DCS boards in the GTU, the monitoring detectors and the Corbo module. The trigger signals are generated by a coincidence of the scintillators in the beam-line. At start of run all the event counters in the MCMs, the GTU and the CORBO module are reset. From then on any trigger signal is counted in the local entities. In order to avoid a counter mismatch the GTU and the CORBO module must raise their busy signal as long as the readout from the respective super module or monitoring detector is ongoing. Once successfully initialised the trigger system kept running stable.

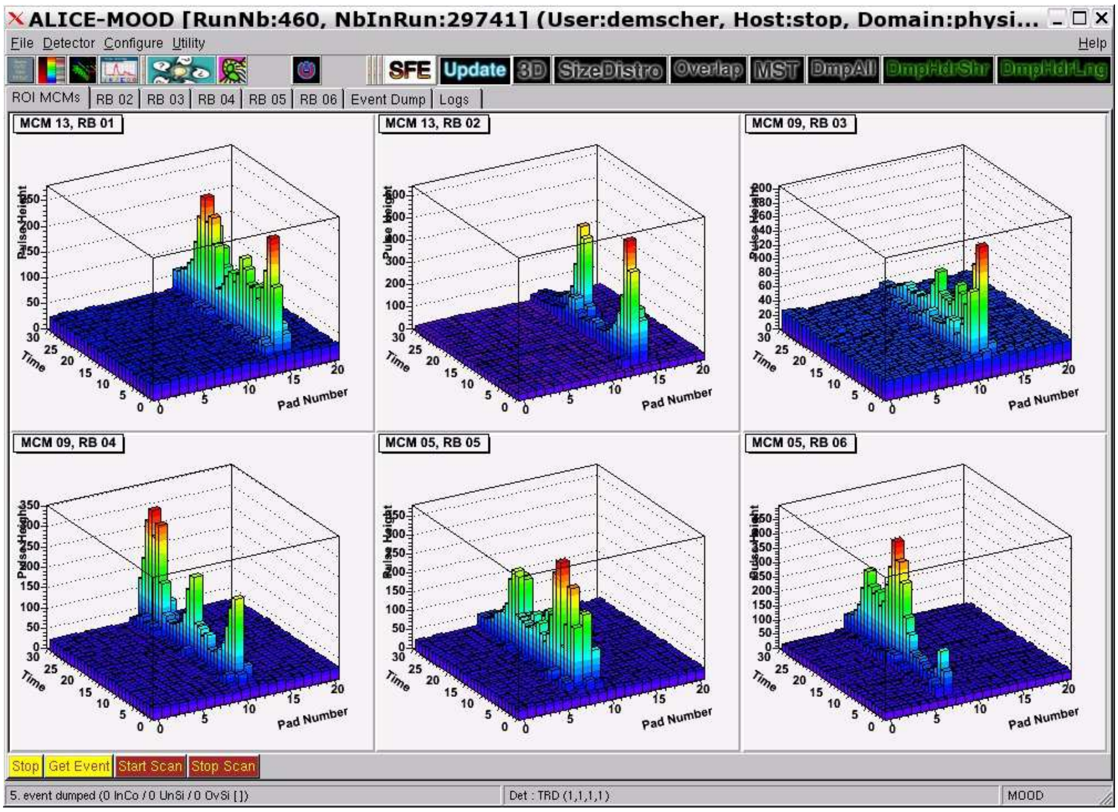

5. event dumped (0 InCo / 0 UnSi / 0 OvSi [])

Det : TRD (1,1,1,1)

Figure 8.11: Online event display from 2004 showing a track passing the 6 layers.

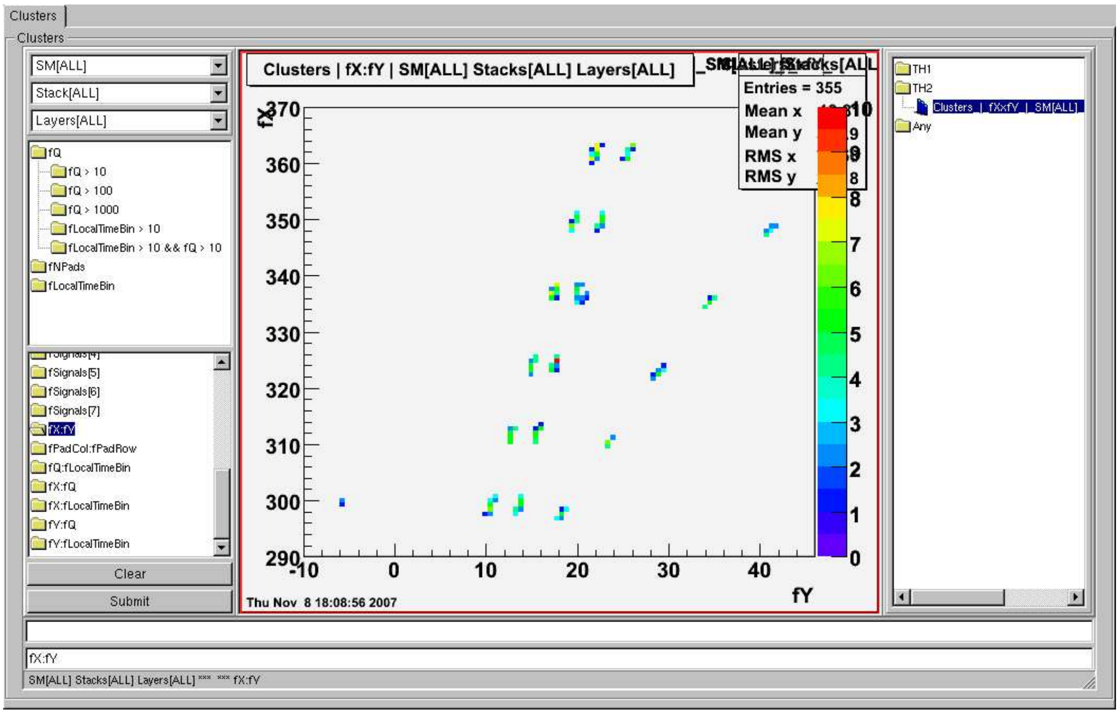

Figure 8.12: HLT online event display from 2007 showing the clusters along the 3 tracks passing through the TRD stack, from [44].

Chapter 9

Detector Performance

We will now evaluate the performance of the TRD based on various beam tests conducted from 2002 until 2007. The particle identification capability and the tracking performance are of special interest.

9.1 Electron identification

The electron identification performance of the TRD is characterised by its power to reject pions at a fixed electron efficiency, we choose 90%. Usually this is expressed in terms of the pion efficiency, the TRD aims at 1% pion efficiency for 3 GeV/c momentum. A prerequisite for this is a precise parameterisation of the measured average amplitude spectra (Figure 9.1) as a function of drift time and momentum both for electrons and pions. It provides the necessary likelihood distributions that allow an evaluation of the electron identification performance. An alternative approach is the use of neural networks for the determination of the particle identity.

Ionisation energy loss The measurements of specific energy loss (dE/dx) in the TRD will contribute to the identification of charged particles, supplementing the tracking identification of the TPC. A precise understanding of the details in dE/dx of electrons and pions is a prerequisite for the correct understanding of the particle separation capability with transition radiation. A beam test using TRD prototype chambers without any radiators was performed in 2002 to allow the measurement of the pure ionisation energy loss, see [46]. Figure 9.3 shows measurements along with simulations of the specific energy loss of pions and electrons in the nominal Xe/CO_2 gas mixture for 2 GeV/c momentum. A remarkable level of agreement was achieved in the simulation of the tails of the energy distribution, when taking into account the δ-electrons. Those are energetic electrons produced in inelastic collisions of primary particles with gas atoms. Some of the energetic δ-electrons can escape the detection volume, if created close enough to the chamber border. One therefore needs to distinguish between the energy loss and the energy deposit, which comprises only the detected signal and is obviously smaller than the former. The specific energy loss spectra for all particle momenta available in the beam (in the range from $1-6$ GeV/c) have been simulated with similar accuracy. This is the basis towards a better understanding of the transition

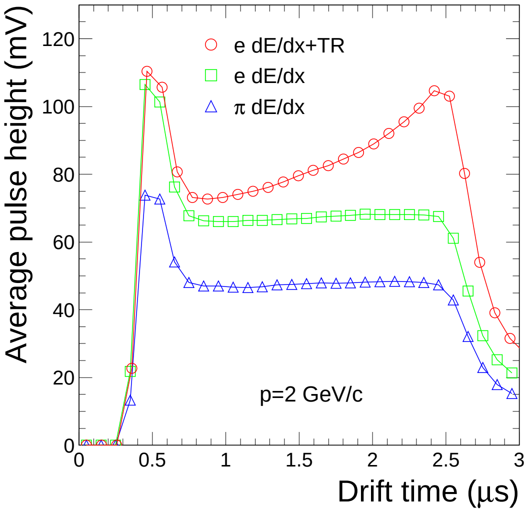

Figure 9.1: Average pulse height as a function of drift time for electrons with a TR (circles), electrons without TR (squares) and pions (triangles), for 2 GeV/c particle momentum, from [22].

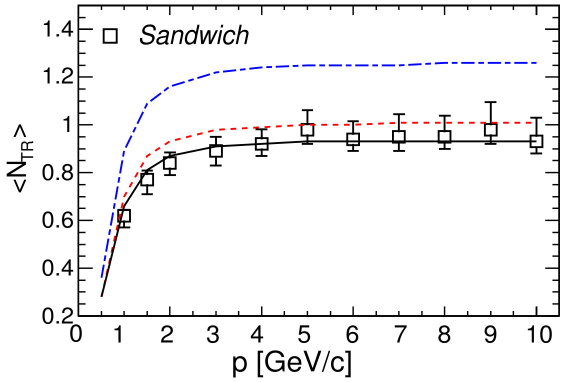

Figure 9.2: Dependence of the mean number of detected TR photons on momentum, from [50]. The simulated values are shown: for a standalone chamber (blue, dot dashed line) for this test setup (red, dashed line) and reconstructed in this test setup by the TR cluster search algorithm (black line).

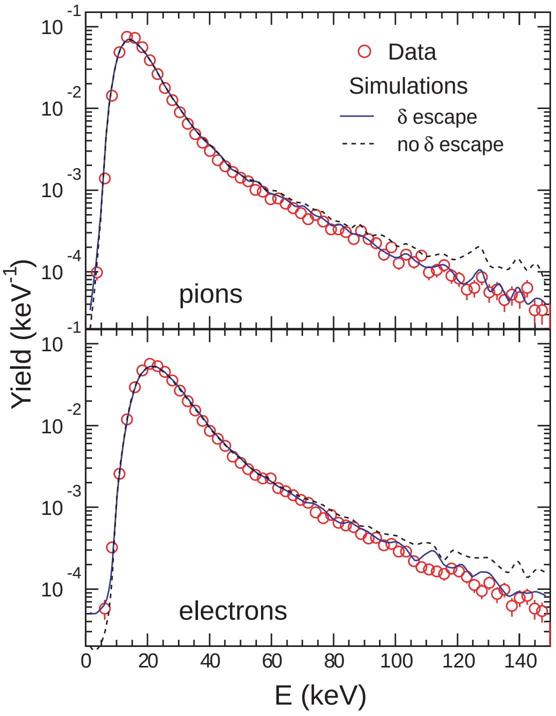

Figure 9.3: Spectra of the energy deposit of pions (top) and electrons (bottom) for the momentum of 2 GeV/c, see [46]. Taking into account the escape of δ-electrons, the measurements for both particle types are well reproduced in simulations.

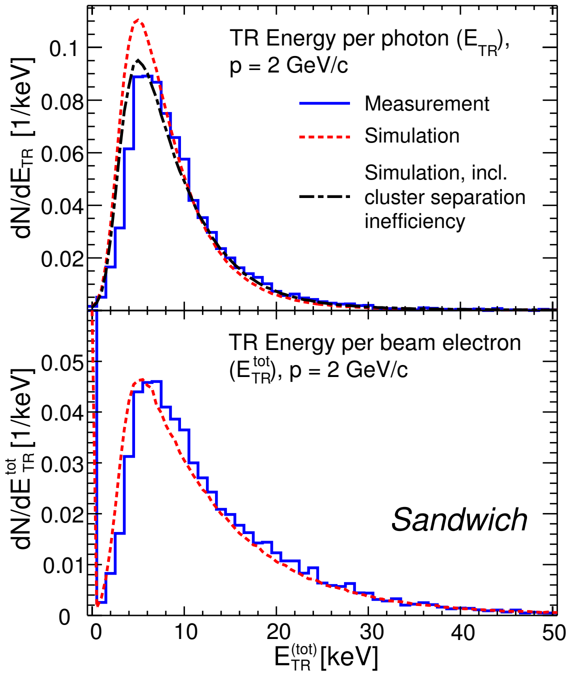

Figure 9.4: Transition radiation spectrum from 2 GeV/c electrons with the ALICE TRD radiator sandwich, from [50]. Energy distribution of single transition radiation photons (top). Total transition radiation energy per beam electron (bottom).

radiation in the TRD.

Transition radiation For relativistic electrons in the TRD, transition radiation is superimposed on the ionization energy loss. A beam test dedicated to the measurement of pure TR spectra with the ALICE TRD was conducted in 2004, see [51]. The TRD prototype chambers with detachable radiators were used for this campaign. A radiator is placed in front of a dipole magnet, its field separates the charged beam particles from the TR photons produced in the radiator. In order to minimise the absorption of TR photons on their way to the drift chamber a pipe filled with helium is placed along the roughly 1.6 m long flight path. The deflection in the magnetic dipole field is tuned such that both, the TR photons and the beam particles, can be detected in spatially well separated clusters in the same drift chamber. The type of radiator used in the TRD chambers was already introduced in chapter 2. The upper panel of Figure 9.4 shows the measured transition radiation spectrum of single TR photons. In order to enhance the quantitative understanding of transition radiation production, the measurements are compared to simulations of TR produced in foil stacks. The adjustable simulation parameters are the number of foils N_f, the thickness of one foil d_1 and the distance between the foils d_2. The three parameters ($N_f = 120$, $d_1 = 15$ μm and $d_2 = 400$ μm) were adjusted such that the simulation, including cluster separation inefficiency in the detector, matches the measured spectra. In the lower panel of Figure 9.4 on can see the distribution of the total total transition radiation energy per incident beam electron. Transition radiation photons in the TRD radiators are produced above a minimum electron momentum of 0.5 GeV/c and level off at about 2 GeV/c, as visible in Figure 9.2, where on average 1.25 TR photons are detected per incident electron (dashed blue line). Realistic simulations on the electron pion separation performance can now be performed with the obtained TR simulation parameters.

Pion rejection The parameterisation of the energy loss and the transition radiation allow to simulate the pion rejection of the TRD and to compare it with measurements from beam tests. Various methods of pion efficiency calculation have been investigated (Figure 9.5), namely the likelihood on total deposited charge (L-Q), the two-dimensional likelihood on total deposited charge and position of the largest cluster (L-Q1,Q2 or L-QX) and an alternative approach based on neural networks (NN). The resulting pion rejection capability was determined as a function of particle momentum. Distributions of the total deposited charge for electrons and pions at fixed momentum (Figure 9.6) are normalised to give probability distributions which serve as input for the L-Q method. For a certain energy deposit E_i in layer $i, P(E_i|e)$ is the probability that it was produced by an electron and $P(E_i|\pi)$ is the probability that it was produced by a pion. Assuming that the six layers have identical performance and that there is no correlation between them, the likelihood L to be a electron is computed as follows :

$$L = \frac{P_e}{P_e + P_\pi} \tag{9.1}$$

$$P_e = \prod_{i=0}^{N} P(E_i|e) \quad ; \quad P_\pi = \prod_{i=0}^{N} P(E_i|\pi) \tag{9.2}$$

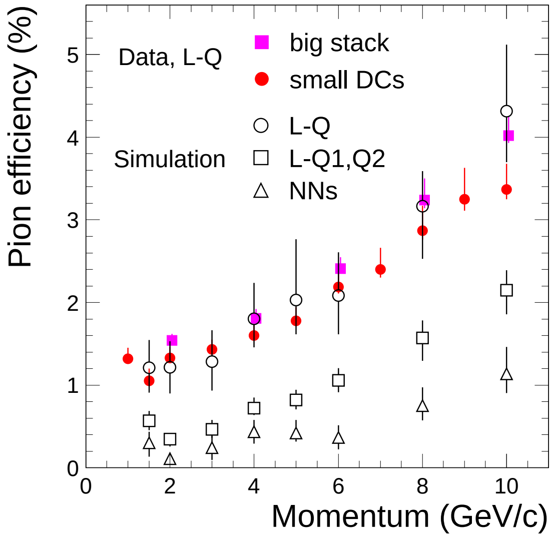

Figure 9.5: Pion efficiency as a function of beam momentum measured with a stack of six chambers and smaller prototype chambers applying a likelihood on the total deposited charge (L-Q) (full symbols), from [19]. The results are compared to simulations (open symbols).

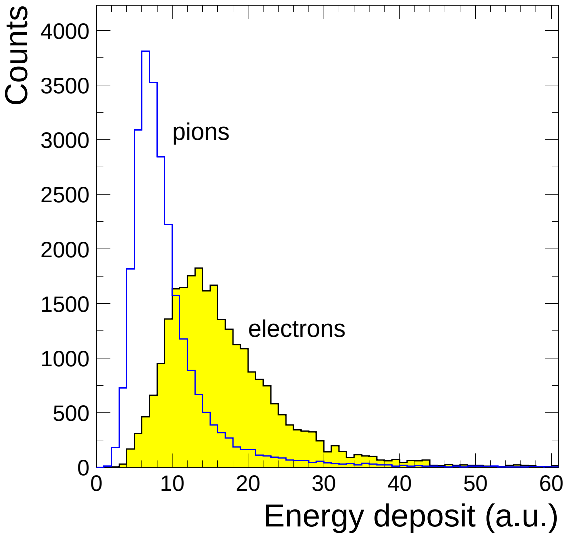

Figure 9.6: Distribution of the total deposited energy for electrons and pions for a momentum of 1 GeV/c, from [22]. After normalisation these distributions serve as input to the likelihood on total charge.

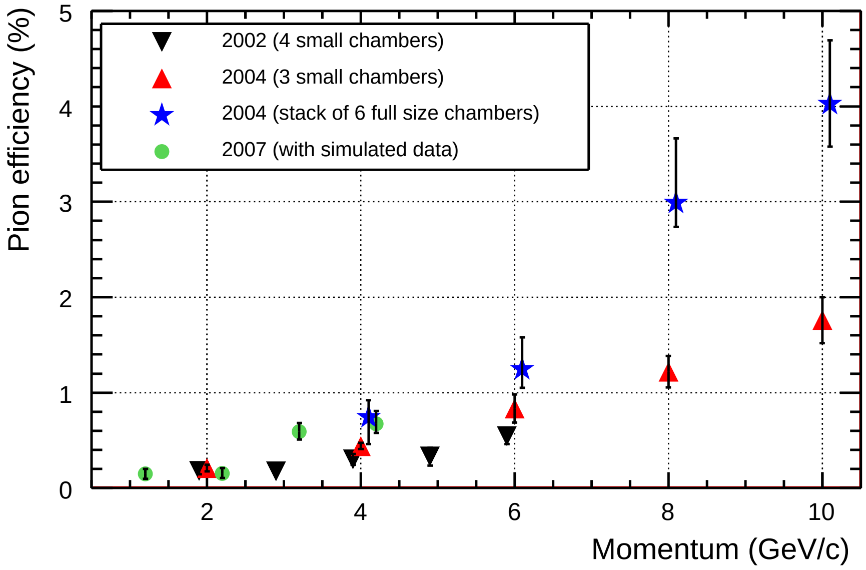

Figure 9.7: Pion efficiency from simulated data obtained with neural networks trained on data sets from different test beams, from [45]. The results between the different beam times are consistent. A significant improvement of more than a factor 3 is reached as compared to the L-Q method. A slight degradation of pion efficiency for full size chambers (stars, circles) is visible as compared to the small prototypes (triangles).

A good agreement between beam data from final and prototype chambers reconstructed with the L-Q method and simulations has been achieved as shown in Figure 9.5. Plotted is the percentage of pions mis-identified as electrons versus momentum at an electron efficiency of 90%. Due to the relativistic rise, the pion efficiency increases as expected with higher momentum, where the pions deposit more charge inside the drift chambers. Relying on an integrated parameter, the L-Q method neglects the shape of the charge distribution. In order to benefit from the dominant TR peak at late drift times in the amplitude spectrum of electrons, a bi-dimensional likelihood on total charge and position of the maximum cluster (L-Q1,Q2) was introduced. It results in a net improvement of pion rejection as compared to the L-Q method, see Figure 9.5.

It has been shown that further improvement can be achieved with a neural network algorithm, see [49]. Compared to standard likelihood methods an improvement in pion rejection up to a factor of 4 is obtained with NN, as these can fully exploit the signal shape. Neural networks were trained on data sets of different test beams and then fed with simulated data. The results, again for for 90% electron efficiency, are shown in Figure 9.7, they are consistent between the different beam times. A slight degradation of pion efficiency for full size chambers as compared to the small prototypes is visible and is probably due to an increased signal-to-noise ratio with the more complex readout electronics of the final chambers. The targeted pion efficiency of 1% at 3 GeV/c momentum is easily undercut with the NN method.

9.2 Particle tracking

The TRD needs a high tracking efficiency (90% for p > 1 GeV/c) and a good momentum resolution (5% for p = 5 GeV/c) to provide a reasonably sharp trigger threshold for individual particles in the range of up to $p_\mathrm{t} \approx 10$ GeV/c. For particles with large momentum the tracking through the six layers of the TRD will improve the overall momentum resolution of the tracking through the central barrel. An efficient track matching between the TRD and the TPC is therefore essential.

Position resolution In the nominal magnetic field of 0.4 T, a position resolution for each time bin of $\sigma_y < 400\mu$m and a resulting angular resolution of $\sigma_\varphi < 1^\circ$ per layer in the bending plane are mandatory to meet the tracking requirements. These resolutions define the transverse momentum resolution of the TRD.

A measurement of the achievable respective resolutions at a fixed incident angle of $\phi = 15.5^\circ$ as function of the signal-to-noise ratio was performed and is shown in Figure 9.8, see [48]. The signal-to-noise ratio is tuned by variation of the gain, which depends on the high voltage applied to the anodes and the gas mixture. The gas gain was adjusted to values of 2400, 3900, 6200 and 9600, while a value around 4000 is the nominal gain of the TRD. The detector meets the requirements at a signal-to-noise ratio of about 40. At a fixed signal-to-noise value, the resolution for electrons is worse as compared to pions. The deterioration of the resolution is due to the energy deposition process of the TR photons, with can spatially deviate from the particle track.

Another measurement of the resolutions under variation of the incident angle has been performed with pions in a magnetic field of up to 0.56 T, see Figure 9.9. For

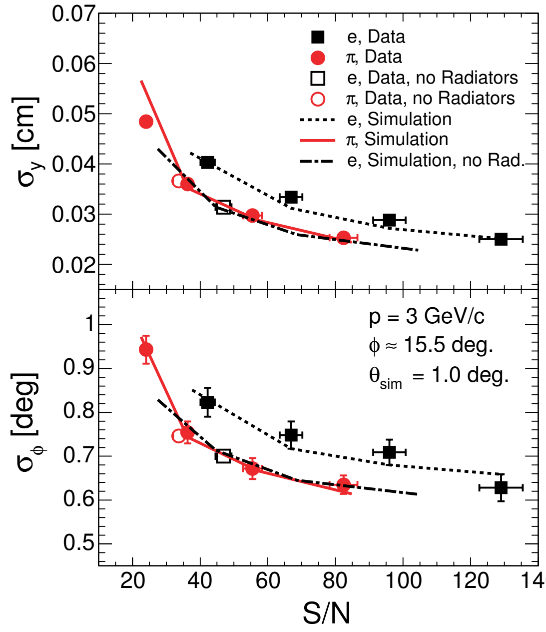

Figure 9.8: Measurements and simulations of the position resolution σ_y (top) and angular resolution σ_ϕ (bottom) as a function of the signal-to-noise ratio (S/N), which can be tuned by gain variation, from [48]. Full (open) symbols refer to electrons and pions measured with (without) radiator.

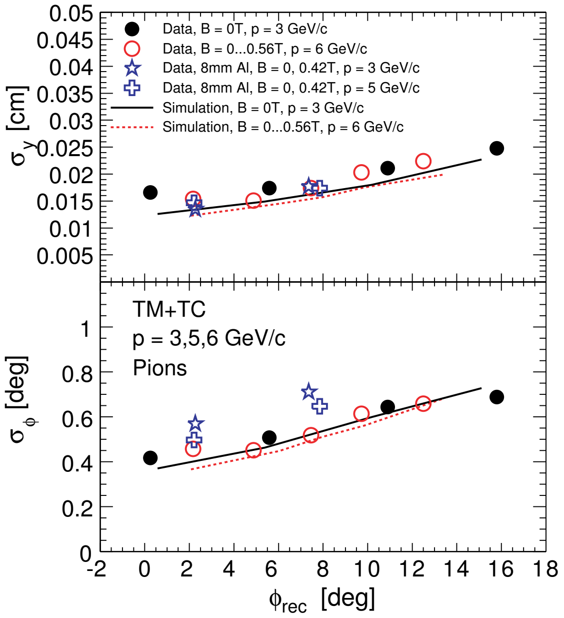

Figure 9.9: Measurements and simulations of the position resolution σ_y (top) and angular resolution σ_ϕ (bottom) as a function of the reconstructed angle for pions with and without magnetic field, from [48].

particle tracks with incident angles from 0° to 15° a position resolution better than 300 μm is achieved. The magnetic field does not have a negative effect on the respective resolutions.

Momentum resolution The stand-alone tracking resolution of the TRD can be derived for different momenta as a function of multiplicity density using the above position and angular resolutions. For momenta below 2 GeV/c the stand-alone momentum resolution of the TRD is around $\Delta p_\mathrm{t}/p_\mathrm{t} \approx 2.5-3\%$ with little multiplicity dependence. Including the TRD into the tracking in the central barrel an overall momentum resolution of better than 5% can be obtained up to momenta of about 100 GeV, as presented in Figure 1.15.

Appendix A

Low voltage power details

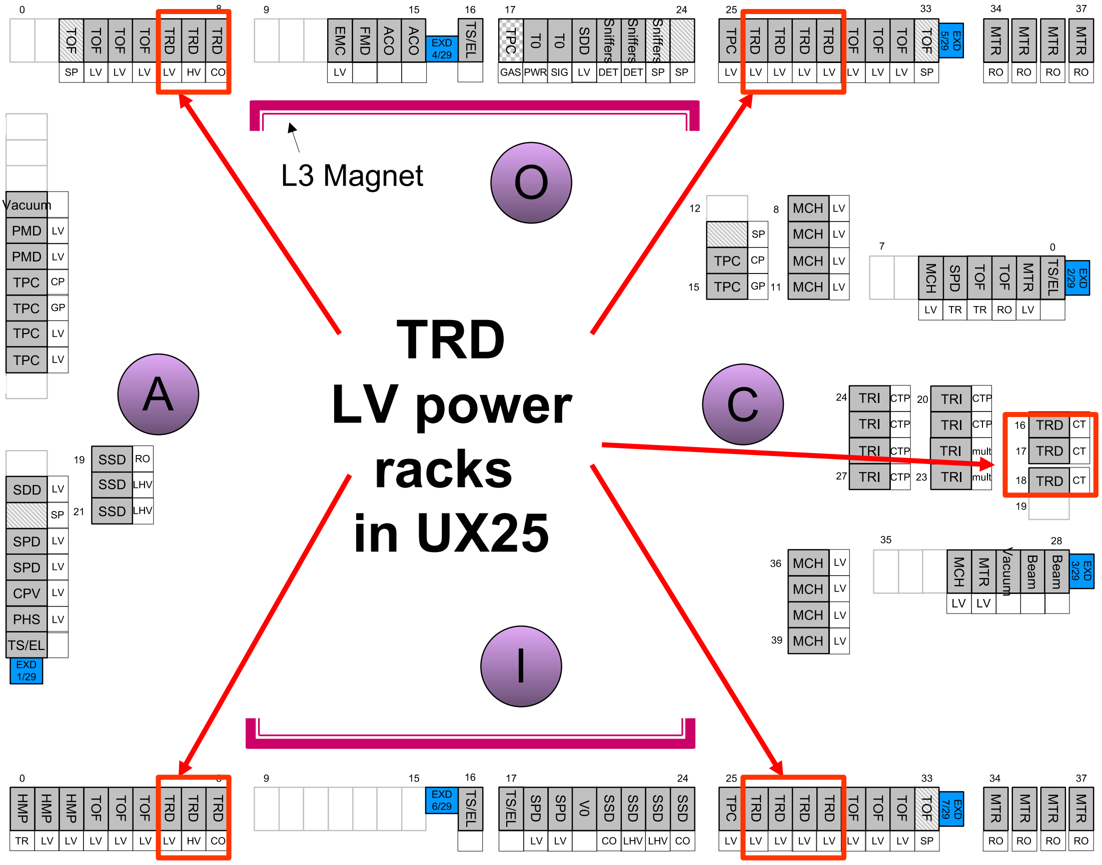

Figure A.1: Location of TRD LV power racks in the ALICE cavern (UX25). Super module power is provided from racks O06, O26, O27, O28, O29, I06, I26, I27, I28, I29. The GTU/PCU power is supplied in racks C16, C17, C18.

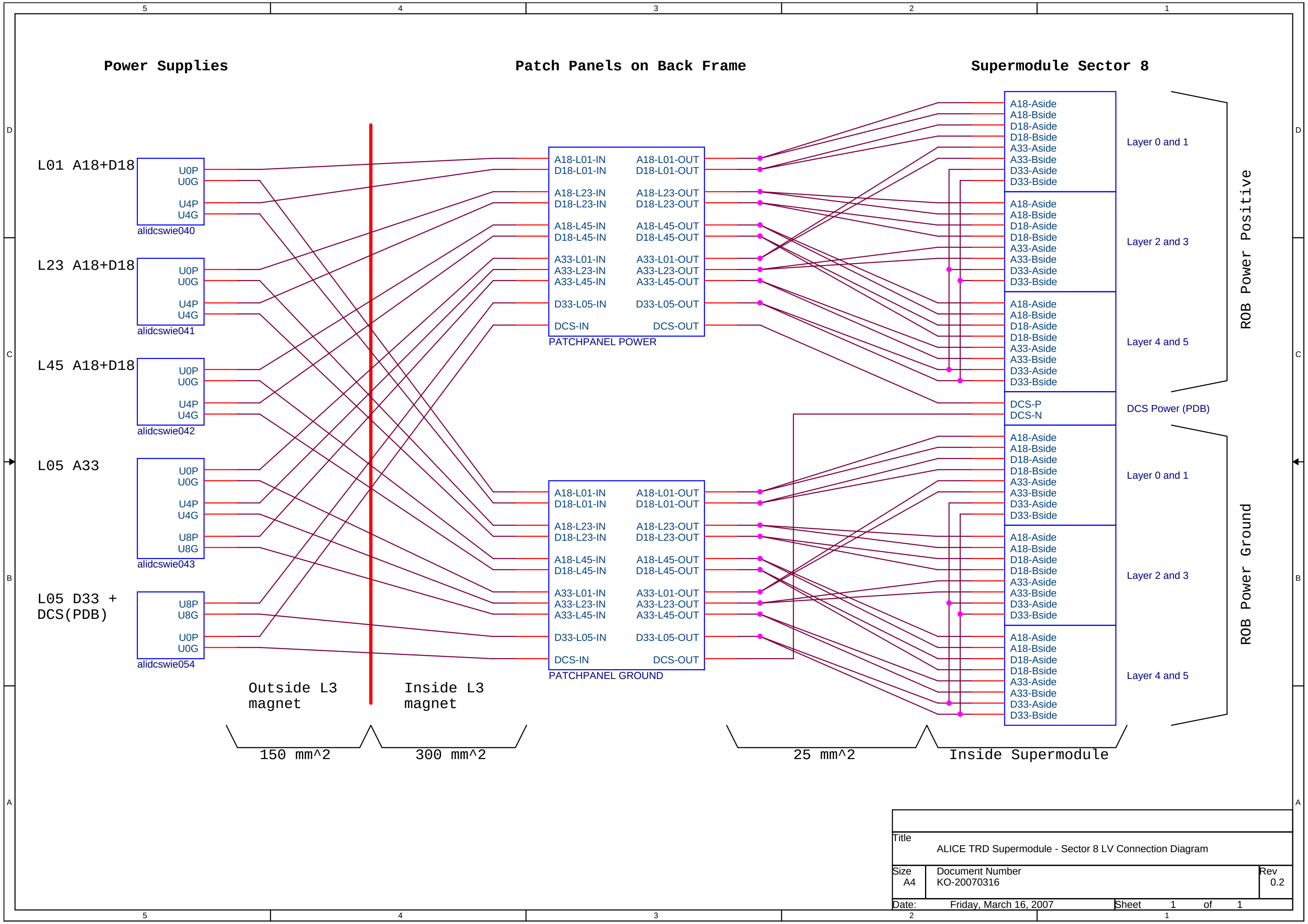

Figure A.2: LV distribution scheme for one super module.

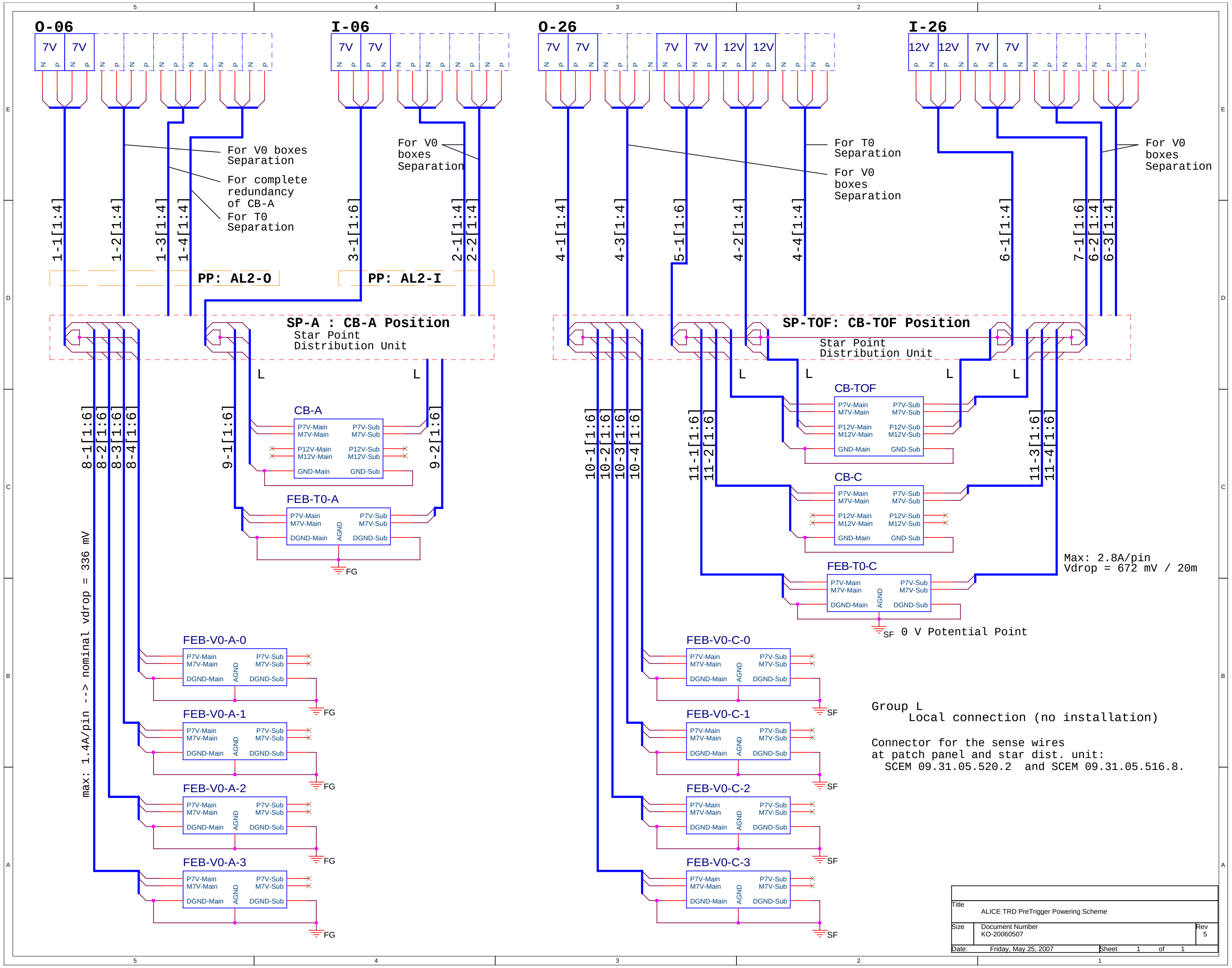

Figure A.3: LV distribution scheme for the pretrigger system.

Appendix B

The layout of TRD pad planes

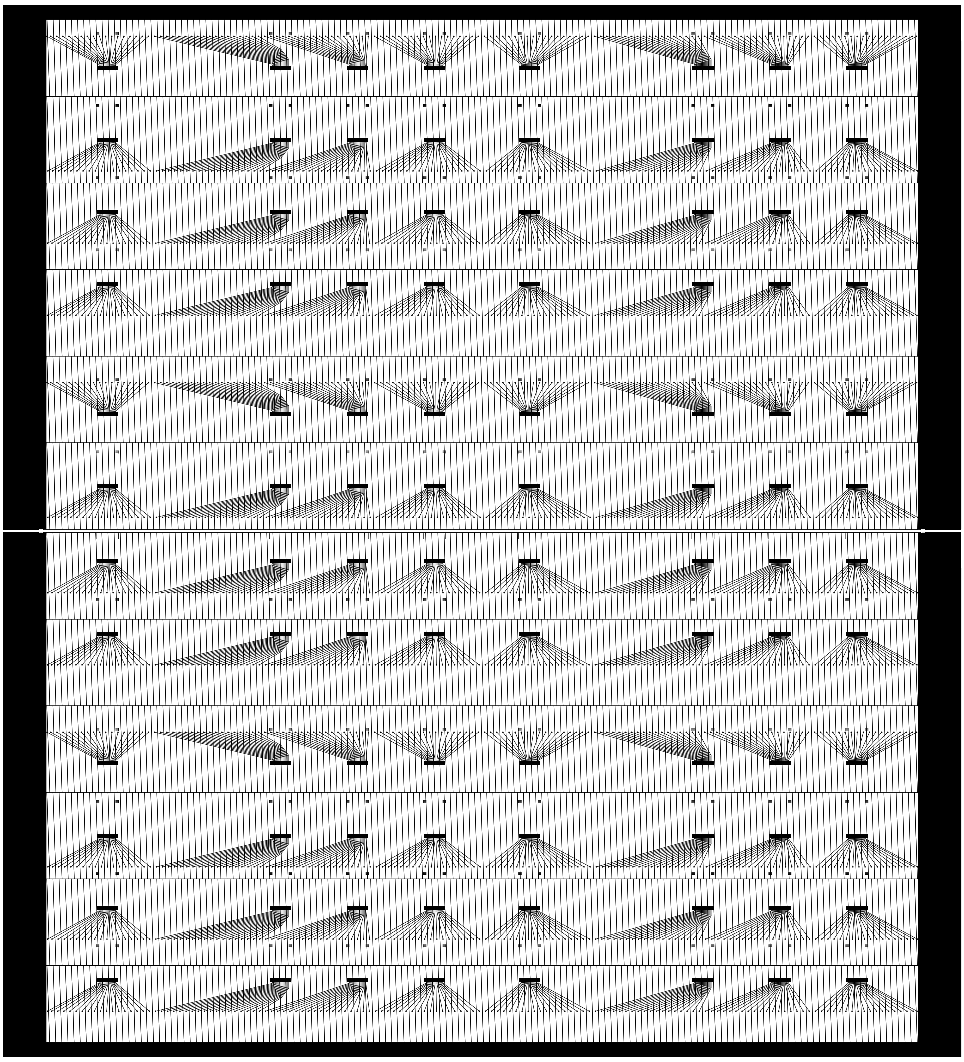

Figure B.1: L0C0 pad plane layout, 2 pieces : top - type 2, bottom - type 1. View from radially outside the chamber, looking through the pad plane, towards the beam pipe. Particles originating from the interaction point see pads tilted in the opposite direction.

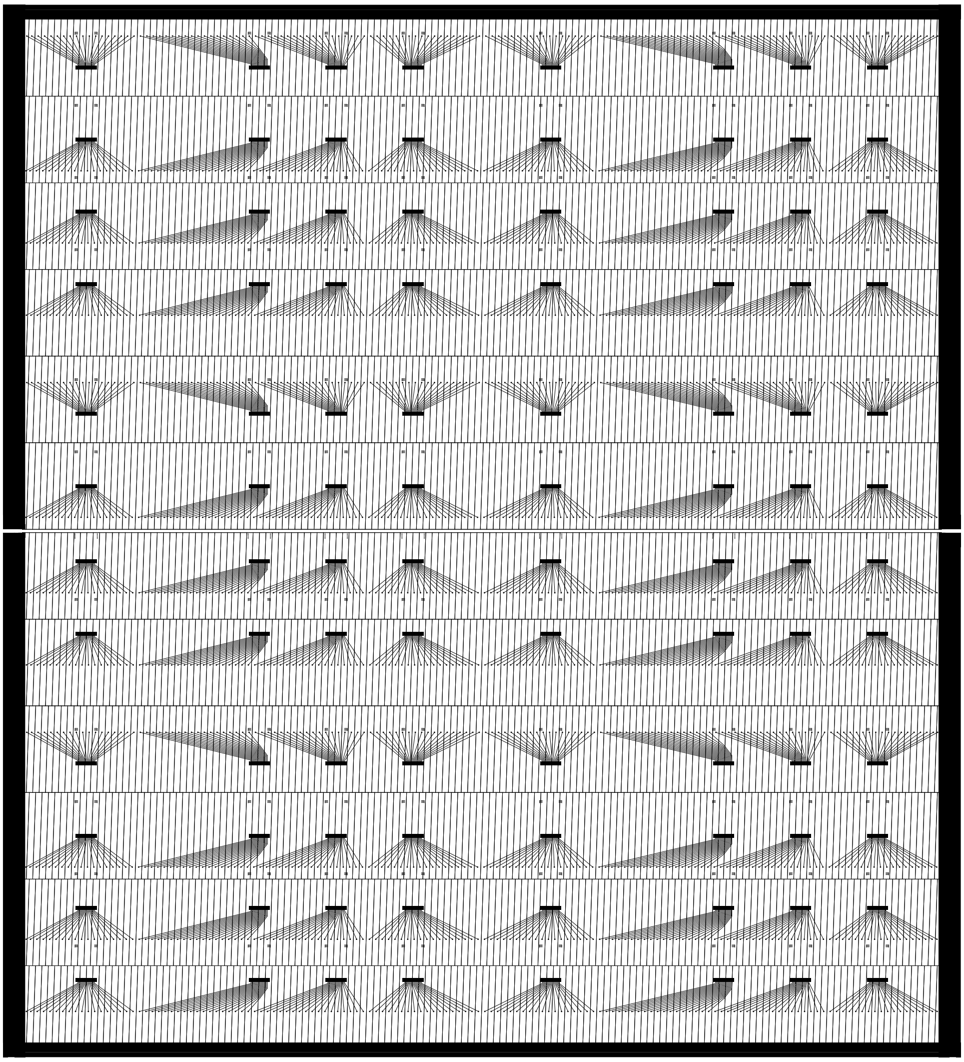

Figure B.2: L1C0 pad plane layout, 2 pieces : top - type 2, bottom - type 1. View from radially outside the chamber, looking through the pad plane, towards the beam pipe. Particles originating from the interaction point see pads tilted in the opposite direction.

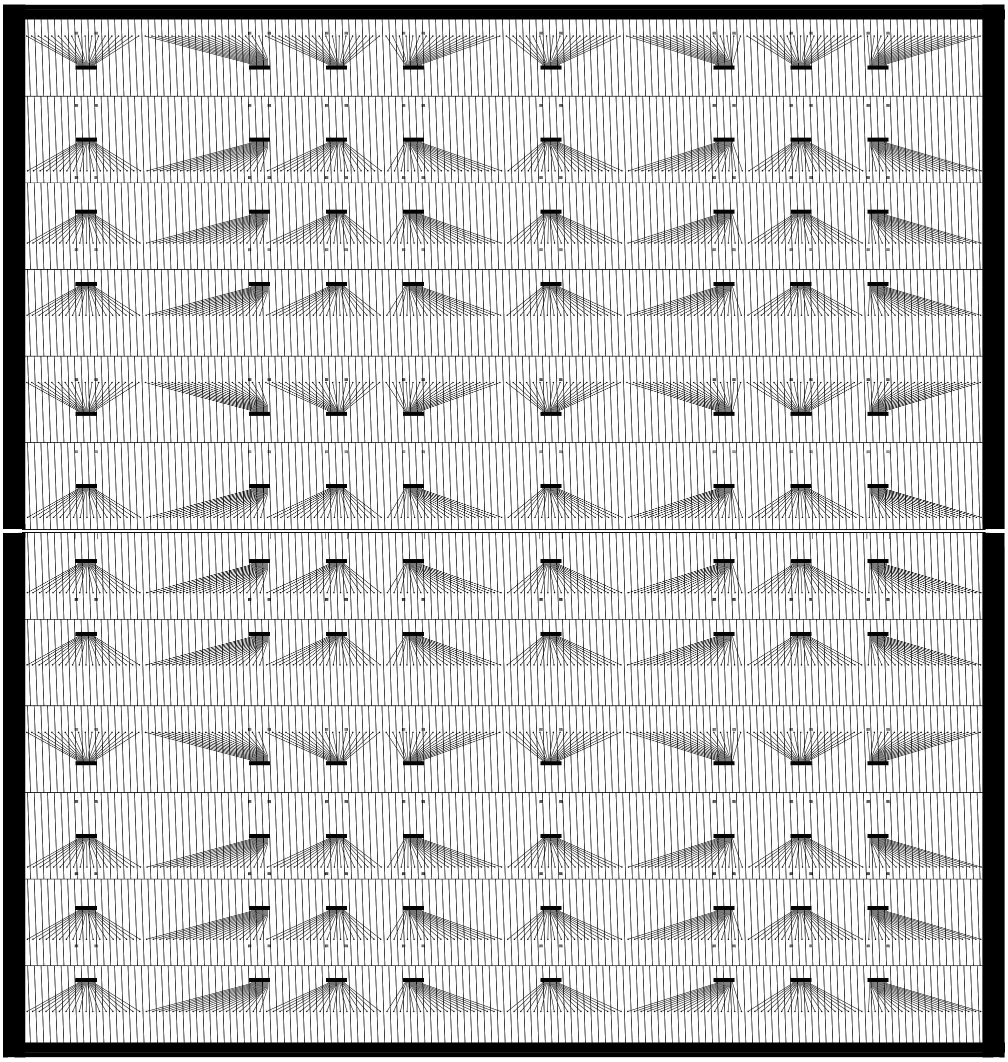

Figure B.3: L2C0 pad plane layout, 2 pieces : top - type 2, bottom - type 1. View from radially outside the chamber, looking through the pad plane, towards the beam pipe. Particles originating from the interaction point see pads tilted in the opposite direction.

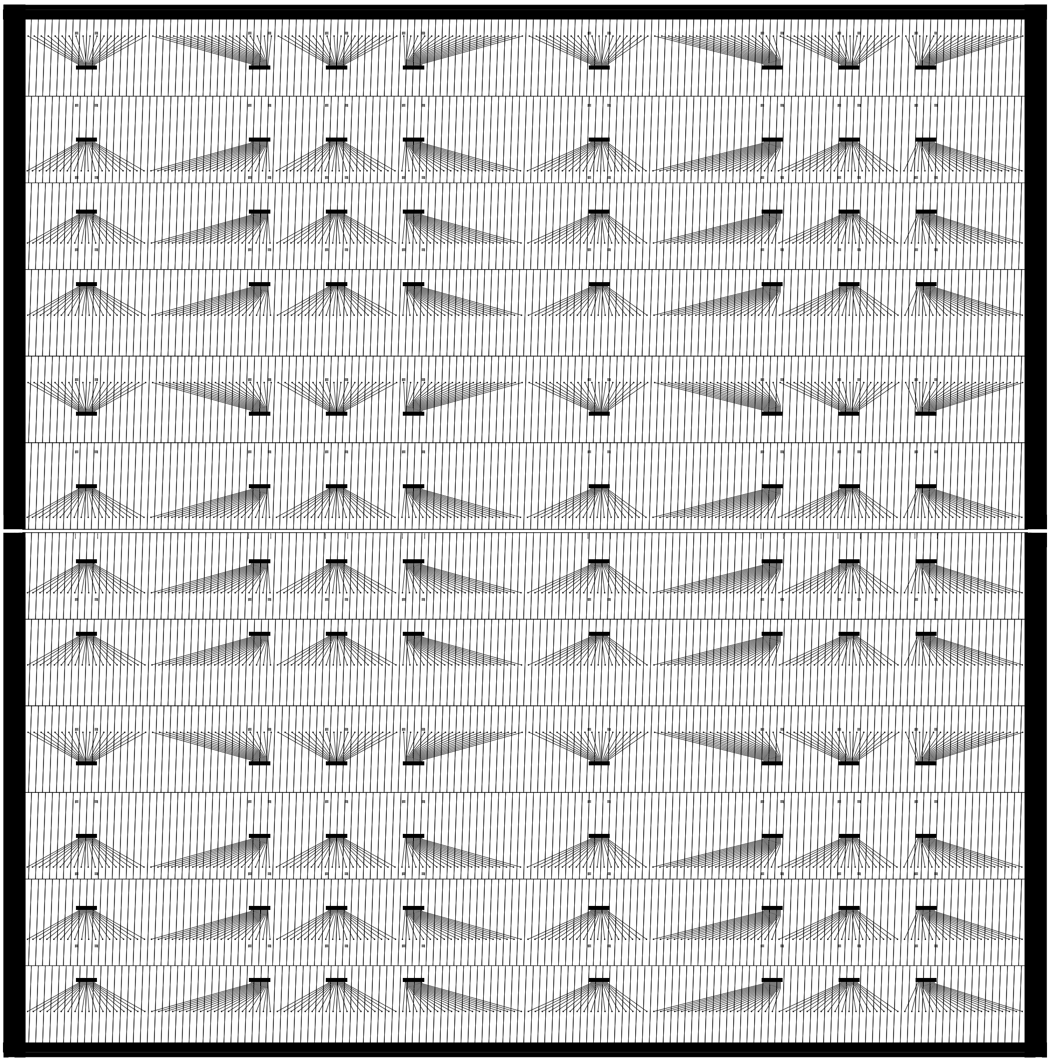

Figure B.4: L3C0 pad plane layout, 2 pieces : top - type 2, bottom - type 1. View from radially outside the chamber, looking through the pad plane, towards the beam pipe. Particles originating from the interaction point see pads tilted in the opposite direction.

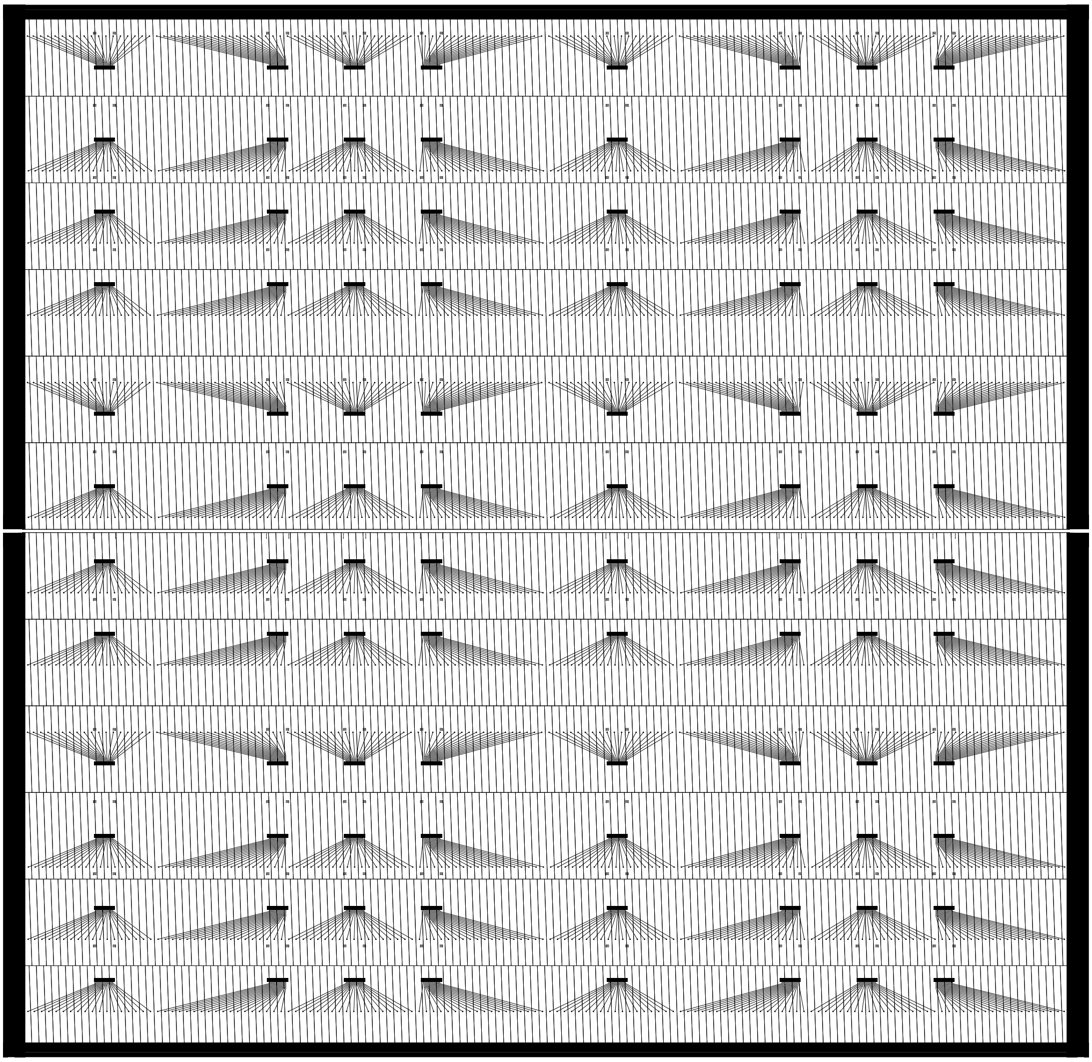

Figure B.5: L4C0 pad plane layout, 2 pieces : top - type 2, bottom - type 1. View from radially outside the chamber, looking through the pad plane, towards the beam pipe. Particles originating from the interaction point see pads tilted in the opposite direction.

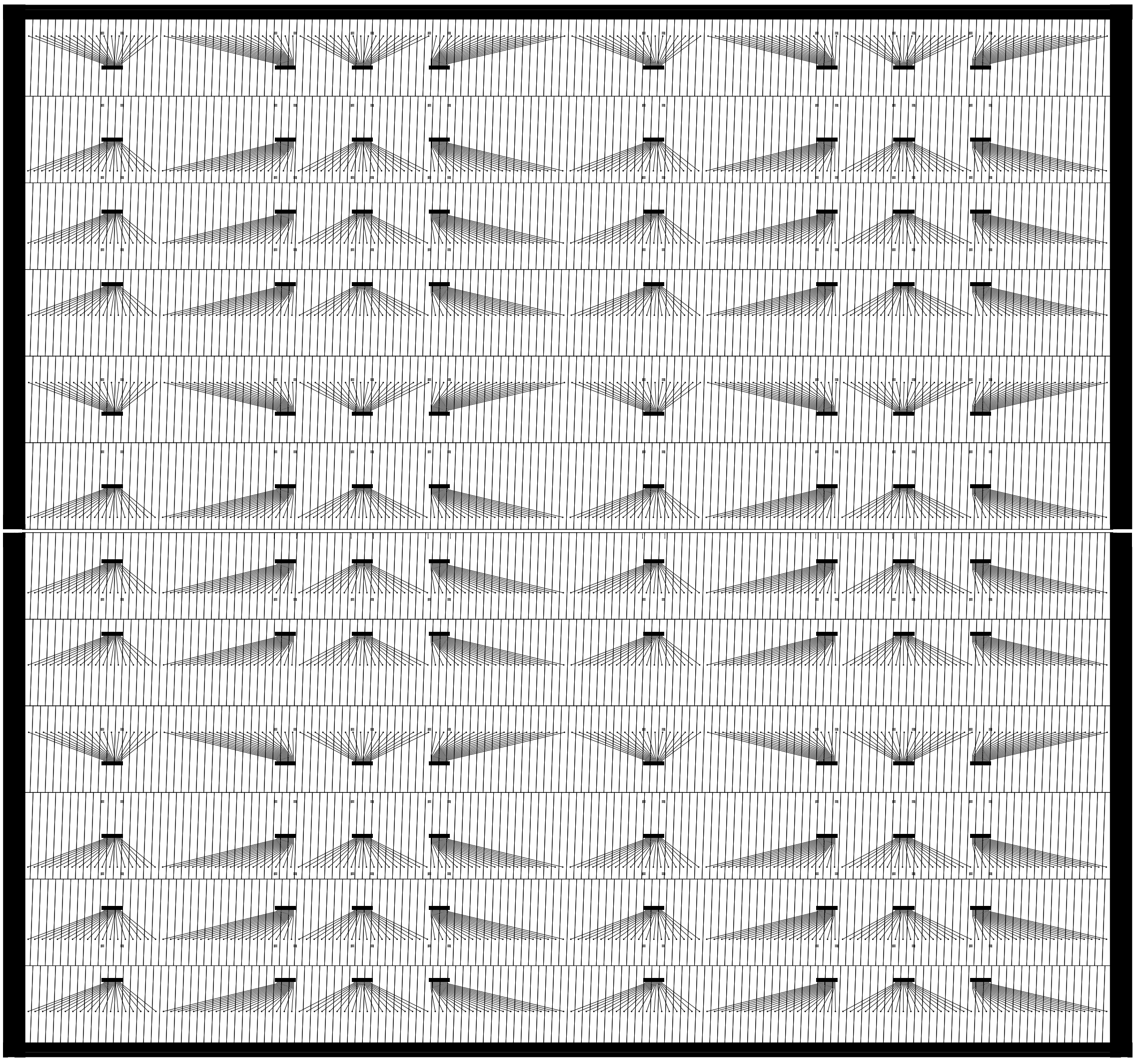

Figure B.6: L5C0 pad plane layout, 2 pieces : top - type 2, bottom - type 1. View from radially outside the chamber, looking through the pad plane, towards the beam pipe. Particles originating from the interaction point see pads tilted in the opposite direction.

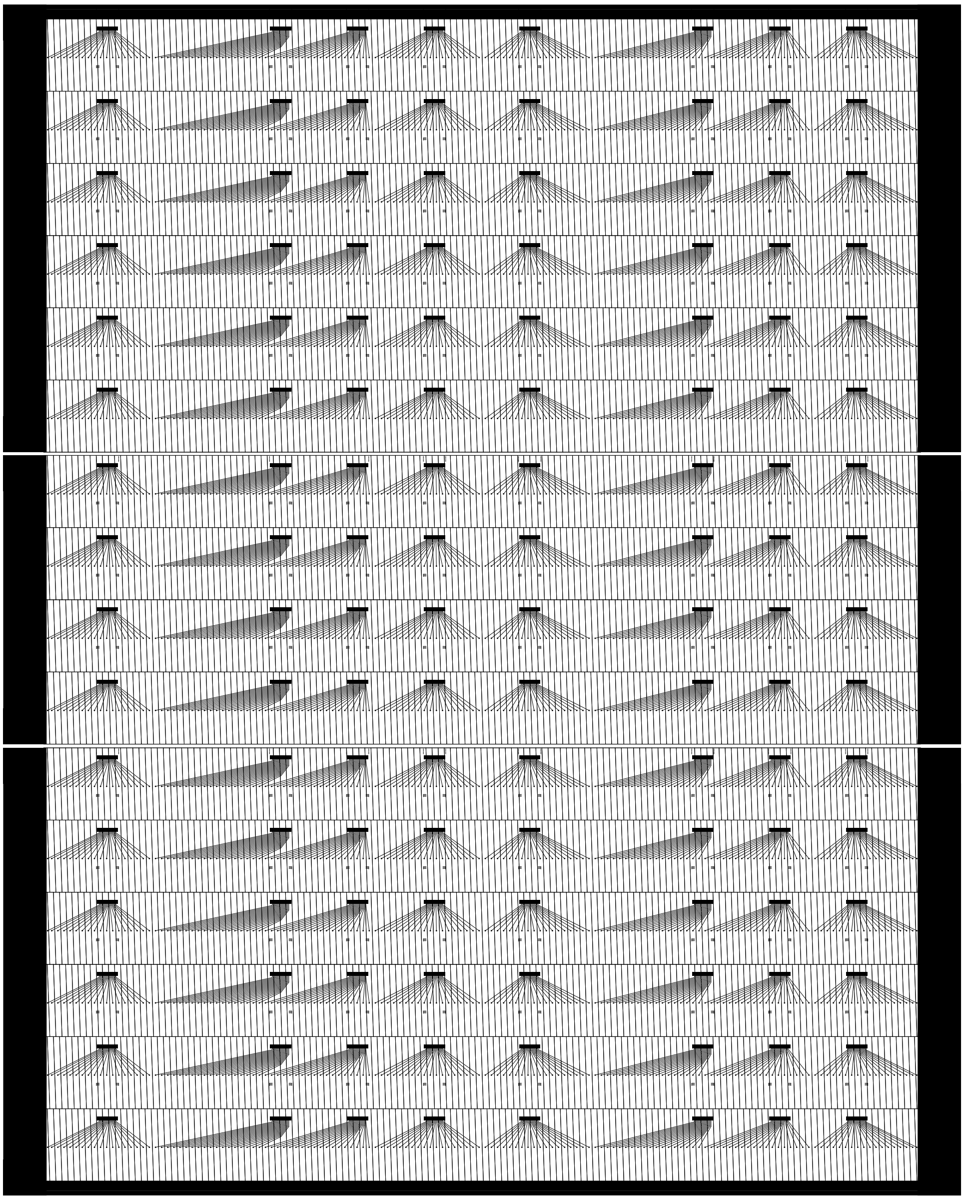

Figure B.7: L0C1 pad plane layout, 3 pieces : top - type 3, middle - type 2, bottom - type 1. View from radially outside the chamber, looking through the pad plane, towards the beam pipe. Particles originating from the interaction point see pads tilted in the opposite direction.

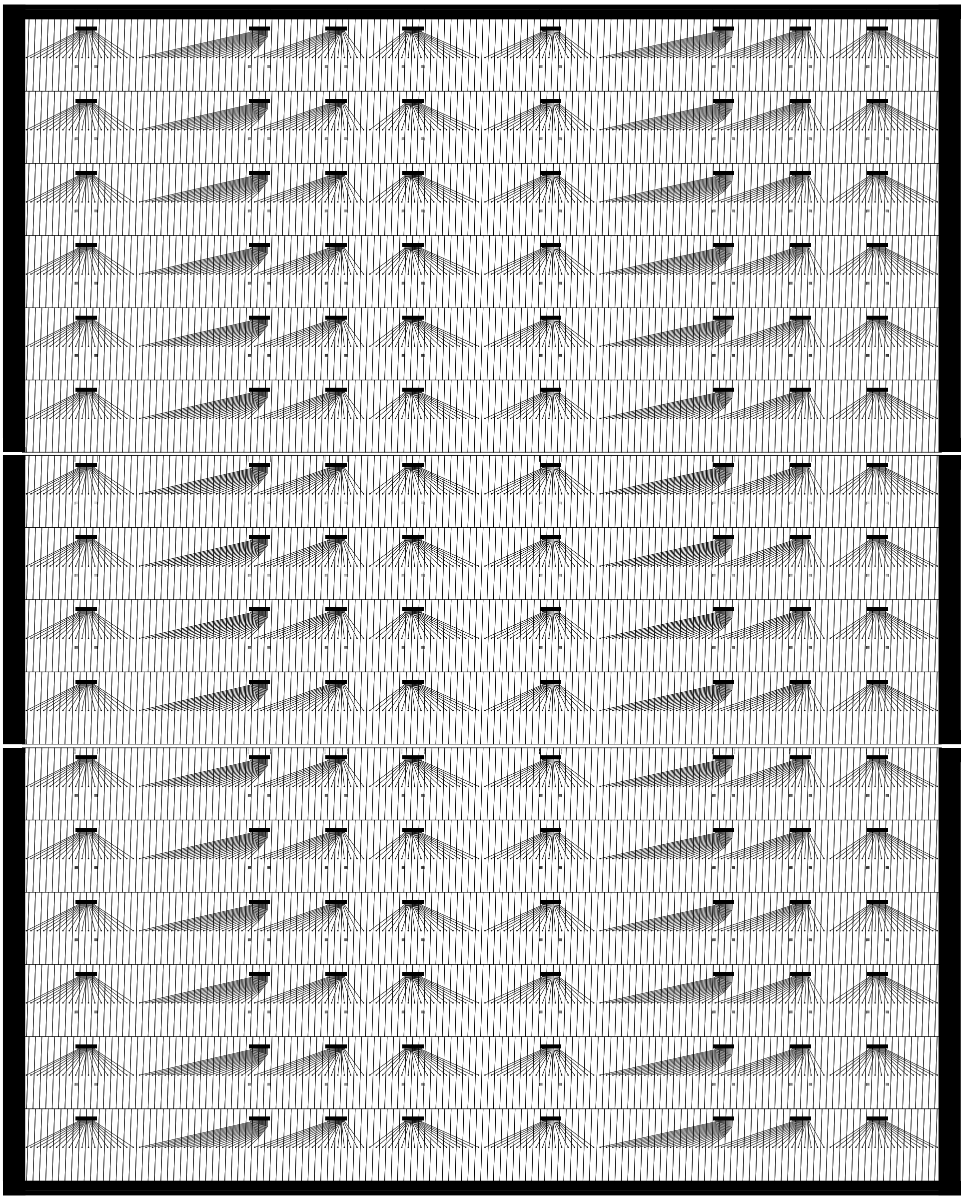

Figure B.8: L1C1 pad plane layout, 3 pieces : top - type 3, middle - type 2, bottom - type 1. View from radially outside the chamber, looking through the pad plane, towards the beam pipe. Particles originating from the interaction point see pads tilted in the opposite direction.

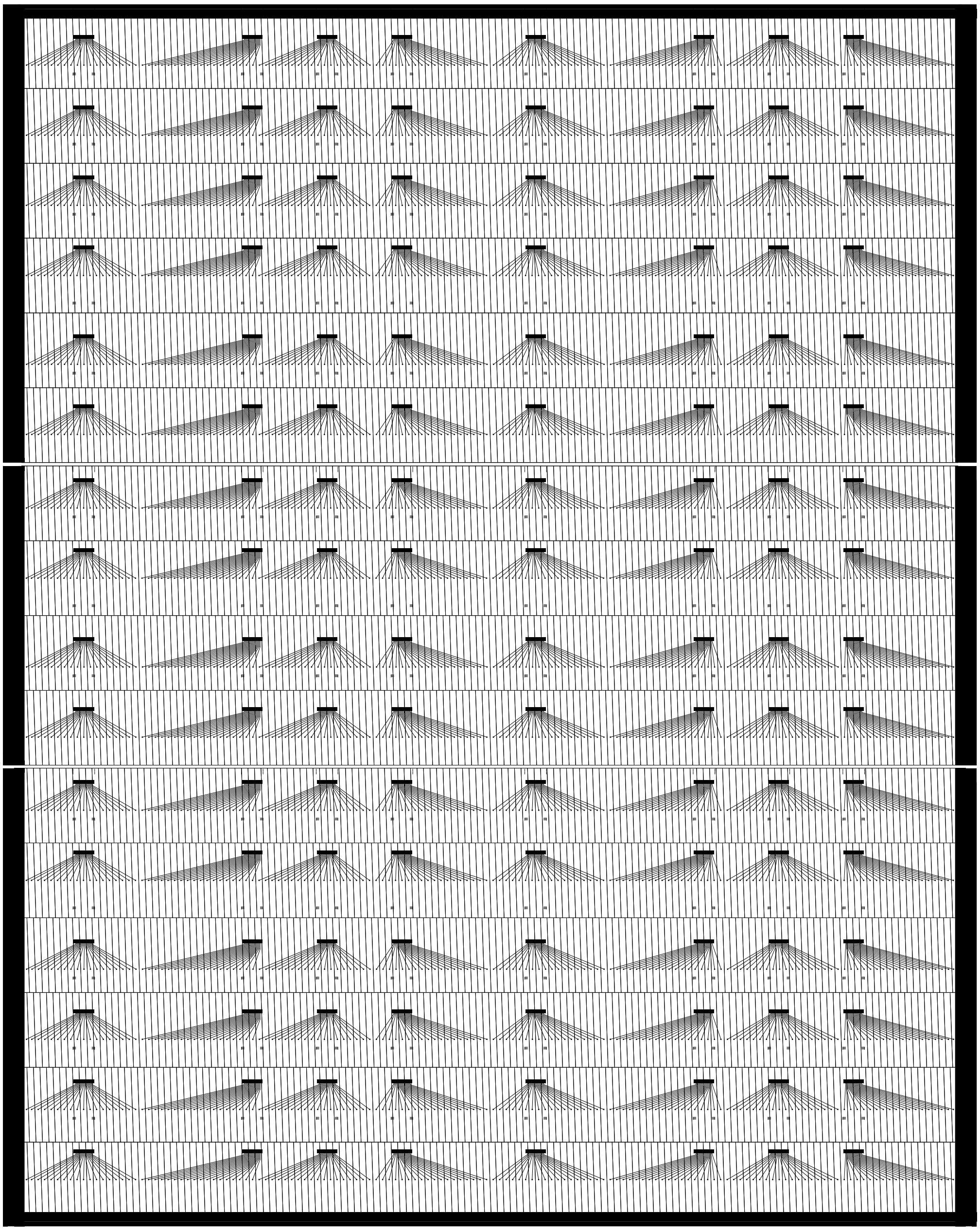

Figure B.9: L2C1 pad plane layout, 3 pieces : top - type 3, middle - type 2, bottom - type 1. View from radially outside the chamber, looking through the pad plane, towards the beam pipe. Particles originating from the interaction point see pads tilted in the opposite direction.

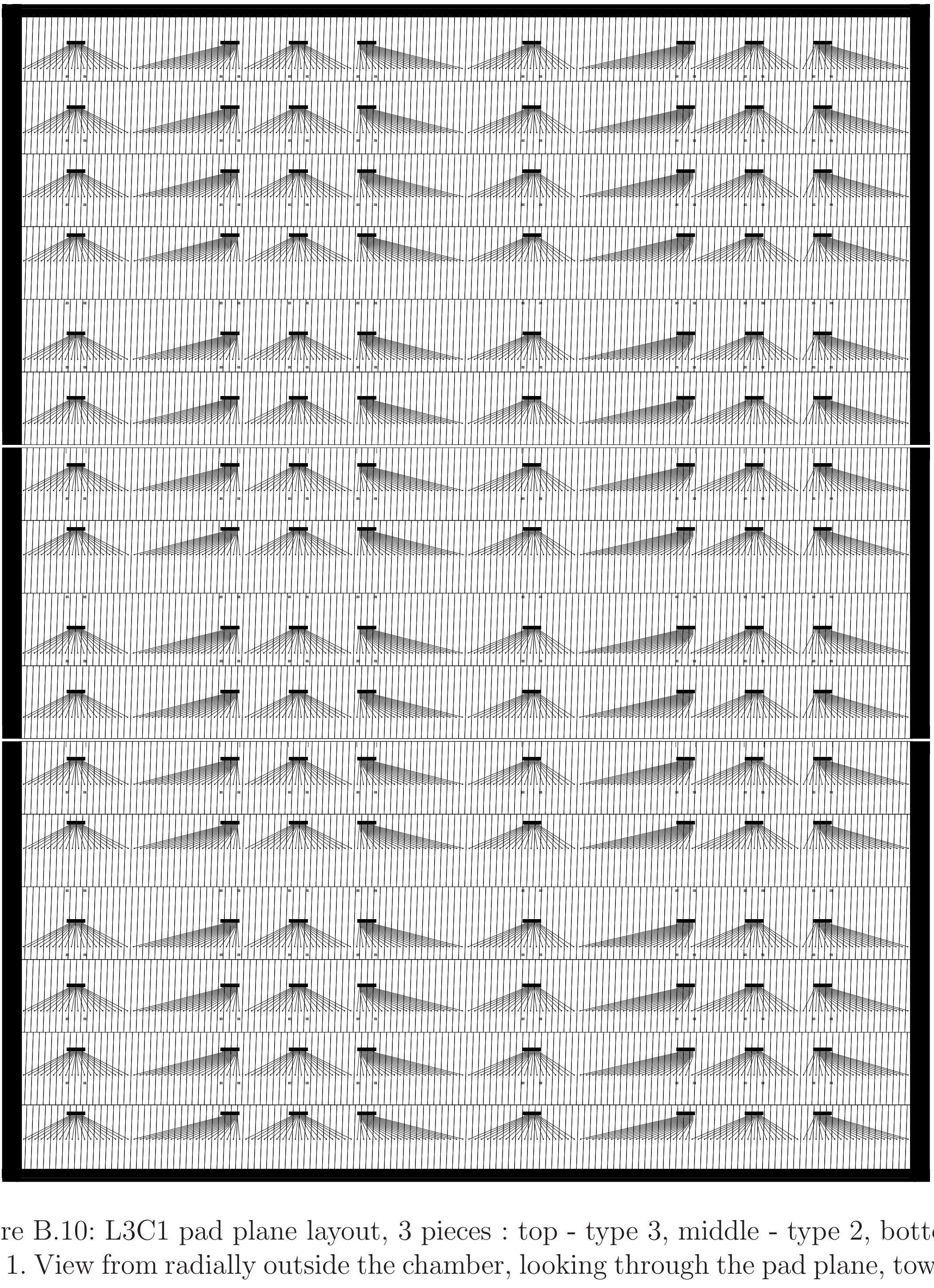

Figure B.10: L3C1 pad plane layout, 3 pieces : top - type 3, middle - type 2, bottom - type 1. View from radially outside the chamber, looking through the pad plane, towards the beam pipe. Particles originating from the interaction point see pads tilted in the opposite direction.

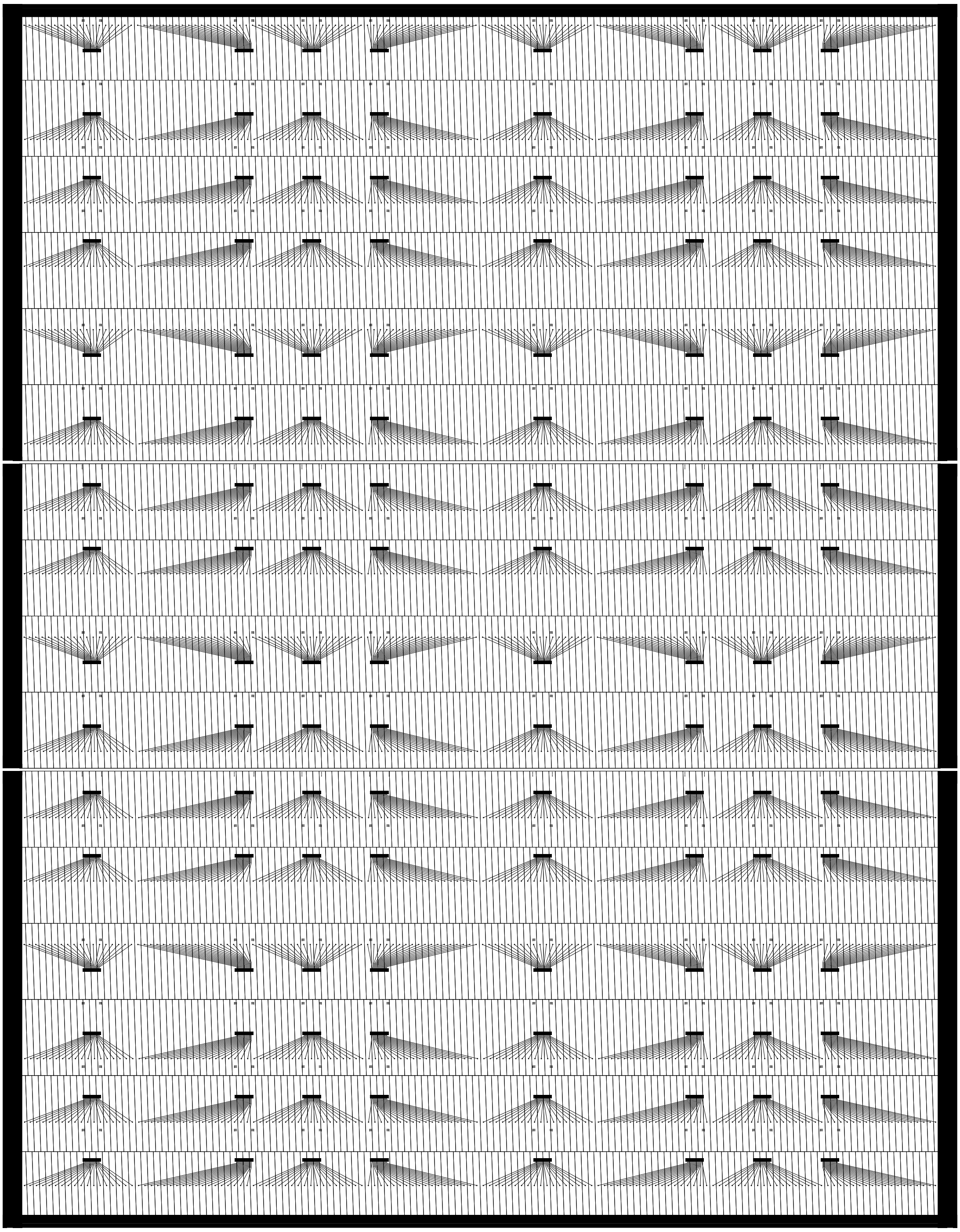

Figure B.11: L4C1 pad plane layout, 3 pieces : top - type 3, middle - type 2, bottom - type 1. View from radially outside the chamber, looking through the pad plane, towards the beam pipe. Particles originating from the interaction point see pads tilted in the opposite direction.

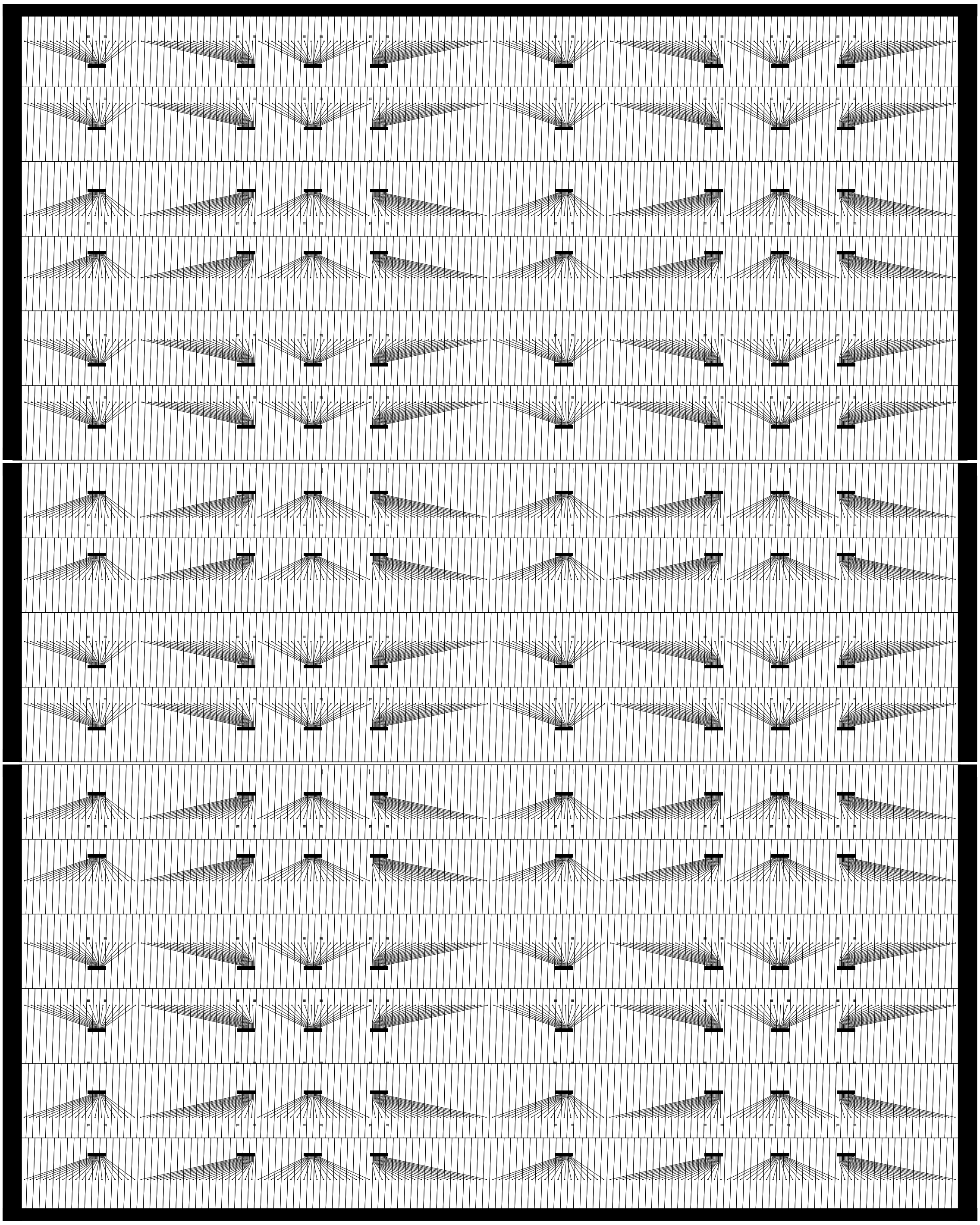

Figure B.12: L5C1 pad plane layout, 3 pieces : top - type 3, middle - type 2, bottom - type 1. View from radially outside the chamber, looking through the pad plane, towards the beam pipe. Particles originating from the interaction point see pads tilted in the opposite direction.

List of Figures

List of Tables

Bibliography

Chapter 1

[1] Frithjof Karsch
Lattice QCD at High Temperature and the QGP
http://arxiv.org/pdf/hep-lat/0601013

[2] F.Karsch, E.Laermann
Thermodynamics and in-medium hadron properties from lattice QCD
http://arxiv.org/pdf/hep-lat/0305025

[3] CBM collaboration
Technical Status Report for the Compressed Baryonic Matter Experiment
Darmstadt, February 2005
http://www.gsi.de/onTEAM/dokumente/public/DOC-2005-Feb-447.html

[4] Berndt Müller
Hadronic signals of deconfinement at RHIC
http://arxiv.org/pdf/nucl-th/0404015v2

[5] X. Zhu et al
DDbar correlations as a sensitive probe for thermalization in high energy nuclear collisions
doi:10.1016/j.physletb.2007.01.072

[6] R. Hagedorn
Nuovo Cim. Suppl. 3 (1965) 147.

[7] T. Matsui and H. Satz
J/ψ suppression by quark-gluon plasma formation
Phys. Lett. B 178, 416 (1986).

[8] A. Andronic, P. Braun-Munzinger, J. Stachel
Hadron production in central nucleus-nucleus collisions at chemical freeze-out
http://arxiv.org/pdf/nucl-th/0511071v3

[9] A. Andronic et al.
Evidence for charmonium generation at the phase boundary in ultra-relativistic nuclear collisions
http://arxiv.org/abs/nucl-th/0701079

[10] W. Sommer, et al
Quarkonia Measurements with the Central Detectors of ALICE
http://arxiv.org/abs/nucl-ex/0702045

[11] Lyndon Evans and Philip Bryant (editors)
LHC Machine
2008 JINST 3 S08001
doi: 10.1088/1748-0221/3/08/S08001

[12] O. Bruning, P. Collier, P. Lebrun, S. Myers, R. Ostojic, J. Poole and P. Proudlock
LHC Design Report Volume I:
The LHC main ring
CERN-2004-003-V-1

[13] O. Buning, P. Collier, P. Lebrun, S. Myers, R. Ostojic, J. Poole and P. Proudlock
LHC Design Report Volume II:
The LHC infrastructure and general services
CERN-2004-003-V-2

[14] M. Benedikt, P. Collier, V. Mertens, J. Poole and K. Schindl
LHC Design Report Volume III:
The LHC injector chain
CERN-2004-003-V-3

[15] Lyn Evans
SLHC Accelerator and Injector Upgrades
SLHC-PP kick-off meeting, 9 April 2008
https://edms.cern.ch/document/1979444045/1

[16] *CERN multimedia gallery*
http://multimedia-gallery.web.cern.ch/

[17] ALICE Collaboration 2004
ALICE: Physics Performance Report, Volume I
J. Phys. G: Nucl. Part. Phys. **30** 1517-1763
http://stacks.iop.org/JPhysG/30/1517
doi: 10.1088/0954-3899/30/11/001

[18] ALICE Collaboration 2006
ALICE: Physics Performance Report, Volume II
J. Phys. G: Nucl. Part. Phys. **32** 1295-2040
http://stacks.iop.org/JPhysG/32/1295
doi: 10.1088/0954-3899/32/10/001

[19] The ALICE Collaboration, K Aamodt et al
The ALICE experiment at the CERN LHC
2008 JINST 3 S08002
doi: 10.1088/1748-0221/3/08/S08002

[20] Particle Data Group 2008
Particle Physics Booklet
http://pdg.lbl.gov/

Chapter 2

[21] ALICE Collaboration 1999
A Transition Radiation Detector for Electron Identification within the ALICE central detector
Addendum to the ALICE Technical Proposal
CERN-LHCC-99-013
http://cdsweb.cern.ch/record/401988

[22] ALICE Collaboration 2001
Technical Design Report of the ALICE Transition Radiation Detector
CERN/LHCC 2001-021
https://edms.cern.ch/document/398057/1

[23] L. Betev,P. Chochula
Definition of the ALICE Coordinate System and Basic Rules for Sub-detector Components Numbering
ALICE-INT-2003-038
https://edms.cern.ch/file/406391/2/

[24] ALICE Collaboration 2004
ALICE Physics Performance Report, Volume I
J. Phys. G: Nucl. Part. Phys. 30 1517-1763
doi: 10.1088/0954-3899/30/11/001

[25] A. Andronic
The ALICE Transition Radiation Detector
http://www-linux.gsi.de/ andronic/physics/trd_alice.pdf

[26] T. Gunji
Study of Transition Radiation Detector for LHC ALICE experiment
Presentation at JPS 27.03.2003

[27] F. Rettig, private communication

[28] S. Zimmer, Diploma thesis 2008

Chapter 3

[29] C. Adler, private communication

[30] S. Wulff, private communication

[31] E. Mathieson et al.,
Nucl. Instr. Meth. A234 (1984) 505
Nucl. Instr. Meth. A279 (1988) 602
Nucl. Instr. Meth. A277 (1989) 277

[32] Gerber RS-274X Format
User's Guide
http://gerbv.sourceforge.net/docs/rs274xrevd_e.pdf

[33] I. Rusanov
Characterizing of the Charge Sensitive Preamplifier
(PASA version 3: Noise)
TRD Wiki – PASA_v3_Measurements_2.pdf

Chapters 4 and 5

[34] K. Oyama, private communication

[35] W-IE-NE-R, Plein & Baus GmbH
http://www.wiener-d.com

[36] ISEG Catalog
iseg Spezialelektronik GmbH
http://www.iseg-hv.com

Chapter 8

[37] ALICE Collaboration 2003
Technical Design Report of the ALICE Trigger, Data Acquisition, High Level Trigger and Control System
CERN-LHCC-2003-062
https://edms.cern.ch/document/456354/1

[38] ALICE Collaboration 2005
ALICE DAQ and ECS User's Guide
ALICE-INT-2005-015
https://edms.cern.ch/file/616039/1

[39] ALICE Collaboration 2005
Technical Design Report of the Computing
CERN-LHCC-2005-018
http://aliceinfo.cern.ch/Collaboration/Documents/TDR/Computing.html

[40] A. Andronic
TRD testbeam status meeting
TRD Status meeting, 05 November 2007
http://www-linux.gsi.de/ andronic/trd/tests/nov07/status.pdf

[41] C.J. Schmidt
The Leaking-TRD Issue, TRD Status meeting, 24 January 2008
http://www-alice.gsi.de/trd/meetings/status/080124/christian.ppt

[42] C.J. Schmidt
TRD Status meeting, 03 November 2008
https://indico.gsi.de/conferenceDisplay.py?confId=348

[43] C. Garabatos, private communication

[44] M. Ploskon, private communication

Chapter 9

[45] A. Wilk, private communication

[46] A. Andronic et al.
Energy loss of pions and electrons of 1 to 6 GeV/c in drift chambers operated with Xe,CO2(15%)
Nucl. Instrum. Meth. A519 (2004) 508-517
arXiv:physics/0310122

[47] A. Andronic et al.
Electron identification performance with ALICE TRD prototypes
Nucl. Instrum. Meth. A522 (2004) 40-44
arXiv:physics/0402131

[48] C. Adler et al.
Position Reconstruction in Drift Chambers operated with Xe, CO2 (15%)
Nucl. Instrum. Meth. A540 (2005) 140-157
arXiv:physics/0511233

[49] C. Adler et al.
Electron/pion identification with ALICE TRD prototypes using a neural network algorithm
Nucl. Instrum. Meth. A 552 (2005) 364
arXiv:physics/0506202

[50] A. Andronic et al.
Transition Radiation Spectra of Electrons from 1 to 10 GeV/c in Regular and Irregular Radiators
Nucl. Instrum. Meth. A558 (2006) 516-525
arXiv:physics/0511229

[51] R. Bailhache and C. Lippmann
New test beam results with prototypes of the ALICE TRD
Nucl. Instrum. Meth. A563 (2006) 310

Erklärung:

Ich versichere, daß ich diese Arbeit selbständig verfaßt und keine anderen als die angegebenen Quellen und Hilfsmittel benutzt habe.

Heidelberg, den ....
David Emschermann